Tesi doctoral presentada per En/Na

Adelina GEYER TRAVER

amb el títol

"Dynamics and structural evolution of collapse calderas: A comparison between field evidence, analogue and mathematical models"

per a l'obtenció del títol de Doctor/a en

GEOLOGIA

Barcelona, 28 de marc del 2007.

Facultat de Grologia
Departament de Geodinàmica i Geofísica

UNIVERSITAT DE BARCELONA

PART IV:

MATHEMATICAL MODELS

PART IV: MATHEMATICAL MODELS

IV. 1 INTRODUCTION

IV.1.1 The role of mathematical models in volcanology

The use of theoretical/mathematical models based on thermodynamics, rock and fluid mechanics principles has become more and more important during the last decades since their are a fast, cheap and accurate method to simulate and predict volcanic processes. In most cases, the complexity of the mathematical expressions makes unworkable the analytical solution of the problem and it is required the application of mathematical models run on computers.

A theoretical model is a simplified abstraction of a certain natural phenomena. The model is acceptable when it is possible to reproduce both experimental and analytical data, but its predictions may be confirmed by subsequent measurements. These models are characterized by a set of equations called govern equations, which describe the physical problem in a mathematical way. Usually, the application of simply algebra is not enough to solve analytically these govern equations, so that it is necessary to apply numerical methods such us differential and/or integral calculus. A numerical simulation is simply the solution of a certain theoretical model under certain set of assumed or given conditions. This includes both the boundary and the initial conditions for the governing equations, which are time-dependent differential equations that explain and predict the phenomenon.

Theoretical models applied to volcanology and especially on collapse calderas, are important to quantify variables, to predict semi-quantitative general conditions for fracture or fault formation and to provide a link with magma properties. Furthermore, this kind of models is flexible and parametric studies are straightforward.

In comparison with the analogue models described in thee previous sections, mathematical models allow to determine when caldera collapse process will occur, but they cannot tell us how such a complex process will develop. Therefore, combination of mathematical and analogue models together with field studies, is by now the best way to

understand the whole sequence of processes involved in the formation of collapse calderas.

IV.1.2 Classification

Theoretical models applied to volcanology are divisible in two principal groups pre-eruptive and eruptive models.

IV.1.2.1 Pre-eruptive models

Modelling pre-eruptive phenomena is crucial to understand those processes that lead to volcanic eruptions. Likewise, this kind of models is crucial to interpret correctly precursory geophysical and geochemical signals of volcanic activity.

Several theoretical models have been developed during the last decades in order to study pre-eruptive processes occurring inside magma chamber, as for example cooling, differentiation, mixing and degasification processes, overpressurization and magma chamber rupture. These models can be divided in two main groups depending on if they consider the magma chamber as an open or a closed system. The first group considers that the pressure increase inside the magmatic reservoir is induced by volatile oversaturation due to the cooling and crystallization process (e.g. Tait et al., 1989; Martí and Folch, 2005). The second group of models assume that the overpression has its origin in the income of fresh magma into the reservoir, which may produce important physical and chemical changes inside the chamber (e.g. Tait et al., 1989; Folch and Martí, 1998). Further pre-eruptive models are also focused on the study of field stresses around the chamber, the magma chamber rupture and the subsequent process of dike injection (e.g. Gudmundsson, 1998; Burov and Guillou-Frottier, 1999).

IV.1.2.2 Eruptive models

Eruptive models are useful to understand the physical aspecst of the eruptive processes throughout thermodynamics, rock mechanics and fluid dynamics. In an ideal case, these models should consider simultaneously the physical processes occurring inside the magma chamber, in the conduit, during the magma output and in the

atmosphere. In fact, processes occurring in each of these domains may affect the others. However, to couple all processes is, by now, a nearly impossible task. The main problem is that each region of the system, chamber, conduit, and atmosphere is physically distinct from the others and the governing equations in each of them require different mathematical techniques. Likewise, several of the implied processes are still obscure.

In order to simplify the solution of the problem the different regions are treat separately. Consequently, we distinguish:

- **Magma chamber models:** These models describe the dynamics of the process of magma withdrawal during an eruption. More recently, this kind of models have been focused on understanding the variations of pressure inside the chamber as a consequence of the magma lost and the subsequent changes in the stress field.

- **Conduit models:** These models are mainly focused on studying those processes taking place during the ascent of magma along the conduit. This includes degasification processes and magma fragmentation. Furthermore, these models provide information of the physical conditions at the magma outflow in the crater.

- **Atmospheric models:** These models aim to characterise the dynamic and deposition of the volcanic material considering certain physical parameters such as volatile content, eruptive rate, conduit diameter, etc.

IV.2 PRESSURE EVOLUTION DURING CALDERA-FORMING ERUPTIONS

As we have already mentioned in different parts throughout this work (see sections I.1.2, II.3.5, III.3.4.3), that caldera-forming systems pass through different stages before eruption and caldera collapse onset and during caldera collapse. These changes are mainly controlled by the internal pressure of the magmatic system or by external factors that also affect the pressure equilibrium of the system. In this section, we present a summary of the theoretical pressure evolution during caldera collapse episodes (Fig. 4.1).

During a whole caldera-forming event cycle the equilibrium of the pressure inside the chamber $\mathbf{P_M}$ (i.e. magmatic pressure) and the lithostatic pressure $\mathbf{P_L}$ controls the evolution and steps of the process (Druitt and Sparks, 1981; Martí et al., 2000).

At the beginning, prior to the eruption, there exists equilibrium in the system. The pressure inside the chamber ($\mathbf{P_M}$) and the external lithostatic pressure ($\mathbf{P_L}$) are equal ($\mathbf{P_M} = \mathbf{P_L}$). However, both external and internal triggers may alter the system (see section I.1.2). The most common external triggers are the injection of fresh magma inside the chamber (Sparks et al., 1977; Blake, 1981; Tait et al., 1989; Folch and Martí, 1998; Troll et al., 2000) and volatile exsolution and the formation of gas bubbles due to the cooling process (Smith and Bailey, 1968; Blake, 1984; Tait et al., 1989; Martí and Folch, 2005). Both processes produce and increase in the magma chamber internal pressure ($\mathbf{P_M} \uparrow$). The chamber is overpressurized, i.e. $\mathbf{P_M} - \mathbf{P_L} > 0$ ($+\Delta\mathbf{P}$). This overpressure can be supported by the host rock if $\mathbf{P_M} < \mathbf{P_L} + \Delta P_{START}$, where ΔP_{START} is the overpressure necessary to break the host rock by tension, i.e. the tensile strength of the rock. However, this overpressure may induce microfracturing and local doming. In some cases, at advanced stages of local doming an apical collapse may develop at surface, at the apical part of the dome, where surface tensions are larger (Komuro et al., 1984). The collapse takes place due to a mechanical collapse of the rock and has no volcanic implications, i.e. no magma is extruded. By contrast, if the overpressure inside the chamber is large enough to break the host rock ($\mathbf{P_M} > \mathbf{P_L} + \Delta P_{START}$) the system may evolve in three different ways. Under the presence of a large regional doming, due to tectonic compression or underplating, eruption through ring-faults may take place, i.e. a caldera collapse is induced (see section II.5.7.7, type-A calderas). Once the system is open and the caldera collapse is going on, the pressure inside the chamber decreases and subsidence occurs until the system is re-equilibrated. However, under normal circumstances (absence of regional doming), the excess of $\mathbf{P_M}$ may lead to a dike intrusion or if this reaches the surface, to a volcanic eruption (Gudmundsson et al., 1997; Gudmundsson, 1998). During the eruption, the pressure inside the chamber decreases progressively ($\mathbf{P_M} \downarrow$) and the system may response in two different ways. For the first one we consider that the host rock behaves perfectly elastic (end-member situation 1). Consequently, the host rock accommodates instantaneously the pressure decrease inside the chamber re-equilibrating the system, $\mathbf{P_M} = \mathbf{P_L}$. Additionally, due to the elastic assumption the capacity of the host rock for accommodating deformation is unlimited. In

this case the eruption will continue until the closure of the conduit (Quareni and Mulargia, 1993; Papale, 1998). On the contrary, if the host rock behaves rigidly ($\mathbf{P_L}$ (t)=constant) or $\mathbf{P_L}$ decreases slower than $\mathbf{P_M}$, it cannot deal with the ingoing pressure changes. Consequently, the difference between $\mathbf{P_L}$ and $\mathbf{P_M}$ increases with time ($\mathbf{P_M - P_L}$ (t)). It is said that the magma chamber is underpressurized when $\mathbf{P_M - P_L} < 0$ ($-\Delta P$). When $\mathbf{P_M} \leq \mathbf{P_L} - \Delta P_{COLL}$, where ΔP_{COLL} is the underpressure necessary to induce caldera collapse, caldera collapse starts.

From a theoretical point of view and according to the pressure evolution inside the chamber during the caldera-forming cycle, we can say that there are two collapse caldera end-members:

- **Underpressure calderas:** The caldera-forming eruption begins under overpressure inside the chamber that triggers, once overcome the tensile strength of the host rock, magma injection into the host rock and finally, an eruption. The magma withdrawal during these eruptive phases leads to a pressure decrease in the magma chamber. The caldera collapse begins once the resistance of the host rock to break and subside, is exceeded

- **Overpressure calderas:** These calderas form due to the overpressurization of a magma chamber in the presence of a regional extensive stress field and a large scale doming or underplating (). When the tensile strength of the host rock is exceeded, ring fractures nucleate at surface. The caldera-forming eruption starts due to the decompression of the magma chamber throughout the ring faults.

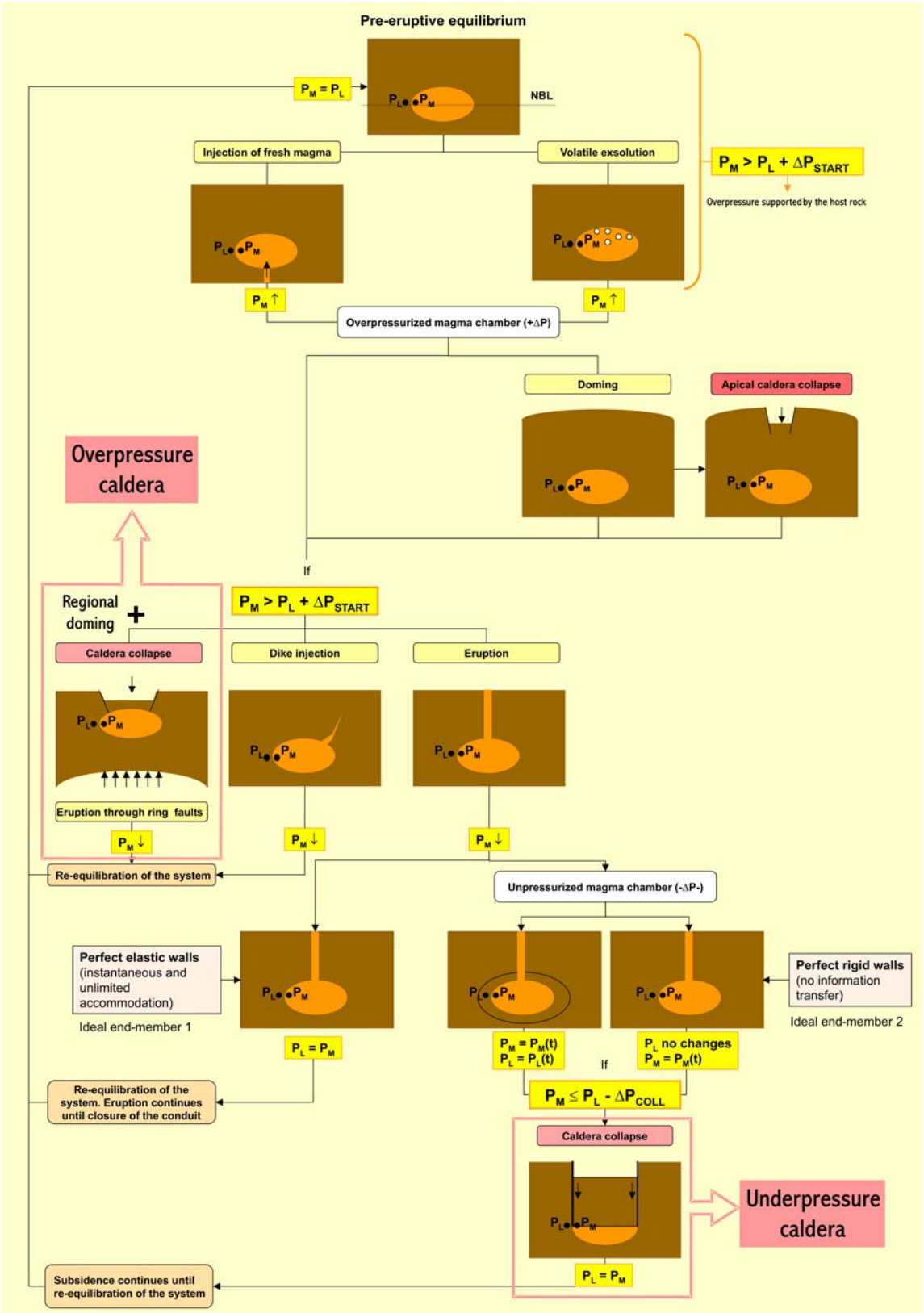

Fig. 4.1: Sketch of the pressure evolution during a caldera-forming event cycle. P_L Lithostatic pressure; P_M Magmatic pressure; **+ΔP** Overpressure; **-ΔP** Underpressure; ΔP_{COLL} Underpressure necessary to induce caldera collapse; ΔP_{START} Overpressure necessary to break the host rock by tension.

IV.3 CONDITIONS FOR RING FAULT INITIATION

In order to encourage the initiation of subvertical, normal ring faults, the stress field must verify three conditions simultaneously (Gudmundsson, 1998; Folch and Martí, 2004):

1. **The minimum value of σ_3, the tensile stress, (maximum tension) must be at surface**

2. **The maximum value of σ_1-σ_3, the shear stress, must occur at the outer margins of the magma chamber**

3. **The maximum tension at surface must peak at a radial distance approximately equal to the projection at surface of the magma chamber extension.**

The latter condition is motivated by the field evidence that ring-faults are nearly vertical and by the agreement between analogue models in showing that the area of experimental calderas coincides approximately with the projection at surface of the chamber extension. The third condition is also verified if the angle $\boldsymbol{\varpi}$ (Fig. 4.2), localized between the vertical and the line that draw from the edges of the cavity and mark the peak of σ_3 at surface is lower than a critical value $\boldsymbol{\varpi_{crit}}$ in the range or lower than 10-15º, i.e. when the absolute minimum value of σ_3 is not only at the Earth's surface but also peaks at a radial distance comprised between $D/2-h_{max}$ and $D/2+h_{max}$, where:

$$h_{max} = P \cdot \tan(\varpi_{crit}) \qquad [4.1]$$

Considering that rocks behave as brittle materials at rapid loads, low confining pressures and low temperatures, i.e. near the surface, whereas they tend to be ductile at high confining pressures and temperatures, i.e. near the chamber (Rutter, 1974), tensional fractures are produced when:

$$\sigma_3 \leq -T_0 \qquad [4.2]$$

whereas shear fractures occur if:

$$\sigma_1 - \sigma_3 \geq S_0 \qquad [4.3]$$

where T_0 and S_0 represent the tensile and the shear strength of the embedding crust, respectively. Equation 4.2 is the Griffith failure criteria for brittle materials under tensional regime ($\sigma_1 + 3\sigma_3 < 0$), whereas Equation 4.3 reflects a limit of the Mohr-Coulomb shear failure criteria near the brittle-ductile transition. Hence, the above expressions can be considered as end-members of the combined Griffith/Mohr-Coulomb failure criteria for brittle materials. Using these criteria, tensional fractures are produced in a plane perpendicular to σ_3 whereas a conjugate pair of shear fractures occurs in the plane σ_1 - σ_3 forming angles of ± 45º with respect the σ_1 direction.

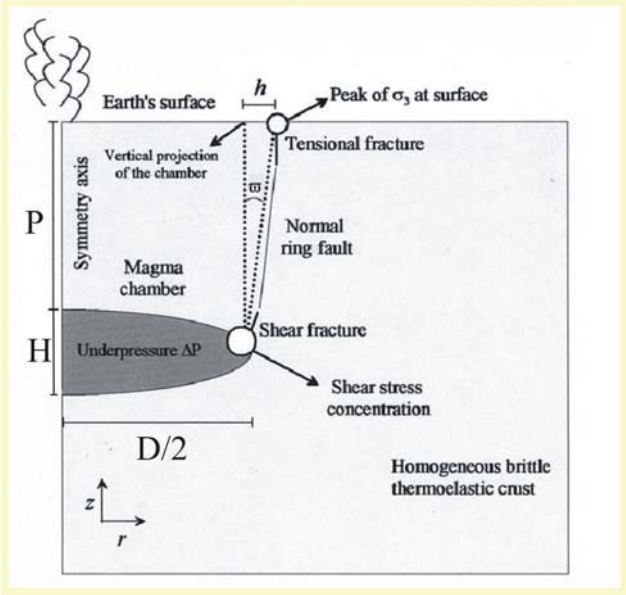

Fig. 4.2: Example of the model geometry applied by Folch and Martí, 2004. **α** Fault dip angle; **-ΔP** Underpressure. **D** Magma chamber diameter; **H** Magma chamber vertical extent; **P** Magma chamber depth. (Modified from Folch and Martí, 2004).

IV.4 STATE OF THE ART

IV.4.1 Mathematical models of collapse caldera: A general classification

The aim of this section is to briefly describe the existing mathematical models related to caldera collapse processes. A summary of the most important results is included, principally those relevant for this study. Furthermore, Table 4.1 lists the existing studies and provides a short description of their most important characteristics.

Mathematical models on collapse calderas performed during the last years can be classified depending on the topic they are focused on. There exit principally three groups:

- **Models focused on the pressure evolution inside the magma chamber:** Druitt and Sparks, 1984; Bower and Woods, 1997; 1998; Martí et al. 2000; Roche and Druitt, 2001.
- **Models to determine stress conditions for normal-fault caldera initiation:** Komuro, 1984; Chery et al., 1991; Gudmundsson et al., 1997; Gudmundsson, 1998; Roche and Druitt, 2001: Folch and Martí, 2004.
- **Models that predict fault location using non-elastic rheology:** Burov and Guillou-Frottier, 1999; Guillou-Frottier et al., 2000; Gray and Monaghan, 2004.

AUTHORS	TYPE OF MODELS	AR	Values for the principal parameters	
			chamber/magma	host rock
Models focused on the pressure evolution inside the chamber and the erupted magma fraction				
Druitt and Sparks, 1981	Analysis of magma chamber pressure during an eruption. Estimate of erupted magma chamber volume fraction	----	**Chamber:** P= 2.5-10 km **Magma:** zoned chamber *silicic magma:* T: 900 ºC, B: 30 GPa, +ΔP: 25 MPa, wc: 4.5-7.5 % *mafic magma:* B: 10-100 GPa	CT: 35-40 km TR: extensional HF: 60 mWm^{-2} fc: 0.6 ρ: 2700 kg m^{-3} E: 100GPa ν: 0.25
Bower and Woods, 1997	Model to expose some of the fundamental controls on the mass, which may erupt from a chamber during the caldera-forming eruption until the critical underpressure at which the walls fail under compression.	---	**Chamber:** P: 2-7 km, H: 3km, vol: 10 km^3, +ΔP: 1-45 MPa, -ΔP: 0-30 MPa **Magma:** ρ: 2700 kg m^{-3}, T: 922 ºC, B: 10-100 GPa, vc: 3-7%, mcc: 0-0.4	----------
Martí et al., 2000	Pressure evolution model during explosive caldera-forming eruptions. Description of the pressure variation throughout the whole central vent eruption-caldera collapse cycle	EL	**Chamber:** P: 3-6 km, D: 1-5 km, H: 1-5 km, +ΔP:10-30 MPa, ΔP_{COLL}:30-60 MPa **Magma:** T: 850 ºC, ρ: 2500 kg m^{-3}, wc: 3.5-6 %	Ss : 40 MPa
Roche and Druitt, 2001	**A)** Scaling analysis: failure criterion for piston collapse along reverse ring fault. Comparison with experimental results. **B)** Calculation of volume fraction required to trigger caldera collapse	MC	**Chamber:** P: 2.5-10 km, H: 0.5-3 km, +ΔP: 0.1-1 MPa, ec: 1-2.5 **Magma:** silicic T: 895 ºC, B: 30 GPa, ρ: 2200 kg m^{-3}, wc: 3-7 wt%	fc : 0.5-0.7 θ : 70-90º c: 0.1-5 MPa ρ: 2700 kg m^{-3} sc: 0.6

Table 4.1: List of the existing studies of mathematical models related to caldera collapse. A short description of the models as well as the applied rheology (AR) and the values for the principal parameters are indicated. ρ Density; ν Poisson's ratio; **+ΔP** Magma chamber overpressure; **-ΔP** Magma chamber underpressure; ΔP_{COLL} Collapse trigger underpressure; θ Ring fault dip angle; **B** Bulk modulus; **c** Cohesion; C_0 Compression strength; **CT**: Crust Thickness; **D** Magma chamber horizontal extent, i.e. diameter **E** Young modulus; **ec** Ellipticity coefficient; **EL**: Elasticity; **ELP** Elastoplastic; **ELPD** Elastic-plastic-ductile; **ELPV** Elastic-visco-plastic; **fa** Friction angle; **fc** Friction coefficient; **GCTS** Griffith criterion under tensile strength; **H** Magma chamber vertical extent, i.e. height; **HF** Heat Flow; **mcc** Magma crystal content; **NV** Non-linear viscous; **P** Magma chamber depth; **PL** Plasticity; S_0 Shear strength; **T** Temperature; **TEL** Thermoelasticity; **TR** Tectonic regime; T_0 Tensile strength; **v** Viscosity; **vc** Volatile content; **VM** Von Mises failure criterion; **vol** Magma chamber volume; **wc** water content.

AUTHORS	TYPE OF MODELS	AR	Values for the principal parameters	
			chamber/magma	host rock
Models to determine stress conditions for normal-fault caldera initiation (incl. caldera morphology)				
Komuro et al., 1984	Apical caldera collapse as a consequence of a domal deformation	ELP-VM	----------	ν: 0.25
Chery, et al., 1991	1) Quasi-static evolution of thermally stratified continental crust near an: -inflating magma chamber -relaxating magma chamber 2) Caldera collapse 3) Resurgence of a central dome	ELPV	**Chamber:** D: >10 km P: 5 km vol: 2000 km^3 +ΔP: 30-60 MPa **Magma:** rhyolitic T:1150ºC	CT: 35-40 km TR: extensional HF: 60 mWm^{-2} fc: 0.6 ρ: 2800 kg m^{-3} E: 100GPa ν: 0.25
Gudmundsson et al., 1997 **Gudmundsson, 1998a,b**	Magma chamber under: -lithostatic equilibrium -overpressure -underpressure -horizontal tensile stresses -vertical compressive stresses	EL-GCTS	**Chamber:** D: 2a-4a +ΔP: 1-5 MPa -ΔP: 10 MPa	E: 40 GPa *v*: 0.25 T_0 : 5 MPa
Folch and Martí 2004	Coupled thermomechanical model to find out the conditons for caldera collapse due to magma chamber underpressure.	TEL-GCTS MC	**Chamber:** P: 3.5 km **Magma:** T: 950ºC	**Crust:** E: 60 GPa v: 0.25 T_0 : 15 MPa S_0 : 50 GPa
Kusumoto and Takemura, 2005	Quantitative discussion of the relationship between the caldera geometry and the magma chamber depth	ELP-MC	**Chamber:** 2P/D : 1-8 km	**Basaltic crust:** E: 40 GPa fa: 30º v: 0.25 C_0 : 15 MPa S_0 : 50 GPa θ: 0-40º
Models that predict fault location using non-elastic rheology				
Burov and Guillou-Frottier, 1999	Thermomechanical numerical model 1) stationary temperature field (rapidly caldera collapses) -no regional compression/extension -regional extension 2) full time-dependent conduction and advection (caldera collapse and long-term post-collapse activity) Influence of: heat diffusion from the hot magma body and thermal blanketing by the ignimbrite cover	ELPD-MC-NV	**Chamber:** H: 5-10 km D: P-25P P: 2-5 km **Magma:** T: 800ºC B: 30 GPa ρ: 2200 kg m^{-3} v: 10^{16} Pa s	**Upper crust:** ρ: 2650 kg m^{-3} **Lower crust:** ρ: 2900 kg m^{-3} **Both crusts:** CT: 10 km fa: 30º E:0.8 GPa ν:0.25 v: 10^{19}-10^{21} Pa s
Guillou-Frottier et al., 2000	Caldera collapse with a pre-defined rectangular existing magma chamber. Steady-state geotherm and no heat transport during the collapse.	ELPD-MC-NV	**Chamber:** P: 2.5 km D: 10-15 km H: 2d -ΔP: 10 MPa	TC: 10 km fa: 30º ρ: 2900 kg m^{-3} E: 0.8 GPa *v*: 0.25 c: 0-20 MPa v: 10^{19}-10^{21} Pa s
Gray and Monaghan, 2004	Numerical simulations of the formation of cracks under tensional stresses or increasing magma chamber pressure. It includes a fracture model that allows to follow the growth of fractures under stress	. EL P-VM DM GCTS	**Chamber:** P: 3.5 km D: 3.5 km H: 1.6 km	----------

Caldera collapse through magma chamber overpressure

Caldera collapse through magma chamber underpressure

Caldera collapse through magma chamber over- and underpressure

Table 4.1 (continuation): List of the existing studies of mathematical models related to caldera collapse. A short description of the models as well as the applied rheology (AR) and the values for the principal parameters are indicated. **ρ** Density; **ν** Poisson's ratio; **+ΔP** Magma chamber overpressure; **-ΔP** Magma chamber underpressure; ΔP_{COLL} Collapse trigger underpressure; **θ** Ring fault dip angle; **B** Bulk modulus; **c** Cohesion; C_0 Compression strength; **CT**: Crust Thickness; **D** Magma chamber horizontal extent, i.e. diameter **E** Young modulus; **ec** Ellipticity coefficient; **EL**: Elasticity; **ELP** Elastoplastic; **ELPD** Elastic-plastic-ductile; **ELPV** Elastic-visco-plastic; **fa** Friction angle; **fc** Friction coefficient; **GCTS** Griffith criterion under tensile strength; **H** Magma chamber vertical extent, i.e. height; **HF** Heat Flow; **mcc** Magma crystal content; **NV** Non-linear viscous; **P** Magma chamber depth; **PL** Plasticity; S_0 Shear strength; **T** Temperature; **TEL** Thermoelasticity; **TR** Tectonic regime; T_0 Tensile strength; **v** Viscosity; **vc** Volatile content; **VM** Von Mises failure criterion; **vol** Magma chamber volume; **wc** water content.

❖ MODELS FOCUSED ON THE PRESSURE EVOLUTION INSIDE THE MAGMA CHAMBER

These models are based on state laws for magmas and on simple fracture criteria. They allow parametric studies varying magma composition and water content, some host rock properties and magma chamber geometry, dimensions and depth.

All models included in this section consider that caldera collapse takes place due to decompression of the magmatic reservoir (e.g. Druitt and Sparks, 1984; Martí et al., 2000). Consequently, these models distinguish two stages in caldera-forming events (Fig.4.3):

- **Stage 1**: Before the eruption, magmatic overpressure becomes large enough ($P_M > P_L + \Delta P_{START}$) to propagate tensile fractures generating pathways for the magma to the surface triggering an eruption. During this phase the conduit or conduits become sufficiently enlarged by sidewall erosion so that they are not totally closed by elastic deformation when the pressure at the top of the chamber falls below lithostatic. Once the eruption begins, removal of magma from the chamber results in a decrease in pressure with time provided that the walls of the chamber remain rigid at the time scale during which the eruption occurs.

- **Stage 2**: The second stage of the eruption is marked by the onset of the caldera collapse. This takes place when the chamber pressure has decreases well below the lithostatic value and the resistance threshold of the host rock has been reached ($P_M = P_L - \Delta P_{COLL}$) .

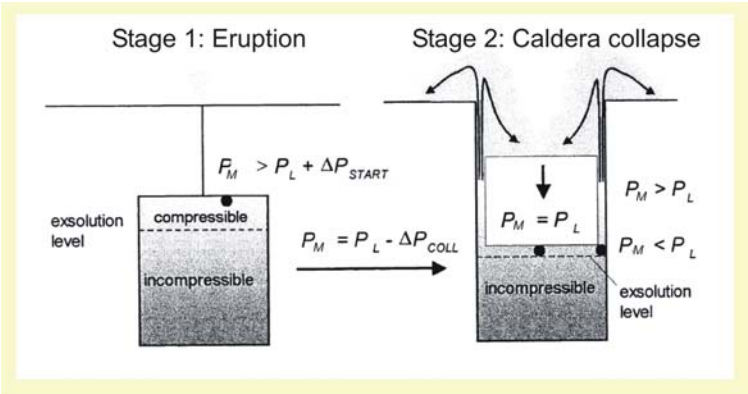

Fig. 4.3: Schematic representation of an explosive caldera collapse process (see text for more details). Solid dots indicate points inside the magma chamber for which Pm is indicated. $\mathbf{P_M}$ Magmatic pressure; $\mathbf{P_L}$ Lithostatic pressure; $\mathbf{\Delta P_{START}}$ Overpressure required to fracture the country rock and to form a conduit to the surface; $\mathbf{\Delta P_{COLL}}$ Shear strength of the rock, i.e. the underpressure necessary to initiate caldera collapse. (Modified from Martí et al., 2000).

Some of these works (e.g. Martí et al., 2000, Roche and Druitt, 2001) are mainly focused on calculating the magma chamber underpressure and the magma volume fraction that needs to be erupted to trigger a caldera collapse as a function of parameters such as the vertical extent, water content, and shape of the magma chamber. Furthermore, these studies offer also a description of the pressure variations throughout the whole central vent eruption-caldera collapse cycle.

The most significant results from this type of models are (Fig. 4.4):

- For a given roof aspect ratio (**R**) the erupted magma chamber volume fraction ***f*** necessary to trigger caldera collapse depends on the water/volatile content (**wc**), the cohesion (**c**), the coefficient of internal friction (**fc**), the ring fault dip angle (θ), the magma chamber height (**H**) and the magma chamber depth (**P**). In fact, in deep chambers the magma remains undersaturated throughout the eruption and the elasticity of the liquid magma and chamber walls controls the mass erupted. Consequently, only a small fraction of the total mass in the chamber erupts. By contrast, in shallow chambers the magma is saturated and consequently, much more compressible. Therefore, the erupted volume of magma from the chamber is larger. Furthermore, for a magma chamber with negative gradient of volatile content, the ***f*** before the collapse decreases significantly compared to that for a corresponding homogeneous chamber. Moreover, the influence of the magma chamber height is also relevant, so that with increasing **H** pressure decrease occurs more rapidly and the collapse conditions are reached at lower ***f*** values. Therefore, dike-like chambers with a great vertical extent need lower ***f*** to reach collapse than sill-like magma chamber, which have a lower fraction of compressible magma and the proportion of magma located above the nucleation level is lower. Magma chambers with the same aspect ratio but with different geometries (cylindrical or ellipsoidal) present similar results.

- Once the eruption has begun, if the eruptive conduit has a suitable geometry or is sufficiently irregular in shape to remain open, the magma can continue to be discharged from the chamber after the internal pressure decreases below lithostatic. The main driving force for magma ascent is caused by the imbalance between the hydrostatic pressure of the vesiculating magma column within the conduit and the magma chamber. If the magma chamber contains a large volume of dense, volatile poor magma it restricts the

effectiveness of the process. The magma must be partially vesiculated in order to facilitate caldera collapse so that there is a minimum value of water content required to ensure the formation of calderas. A low density of the vesiculating magma may result in the hydrostatic pressure being substantially less than the chamber pressure even when the chamber pressure has fallen below the lithostatic value. Consequently, the underpressure might be expected to become sufficient for the walls and the roof of the chamber to collapse.

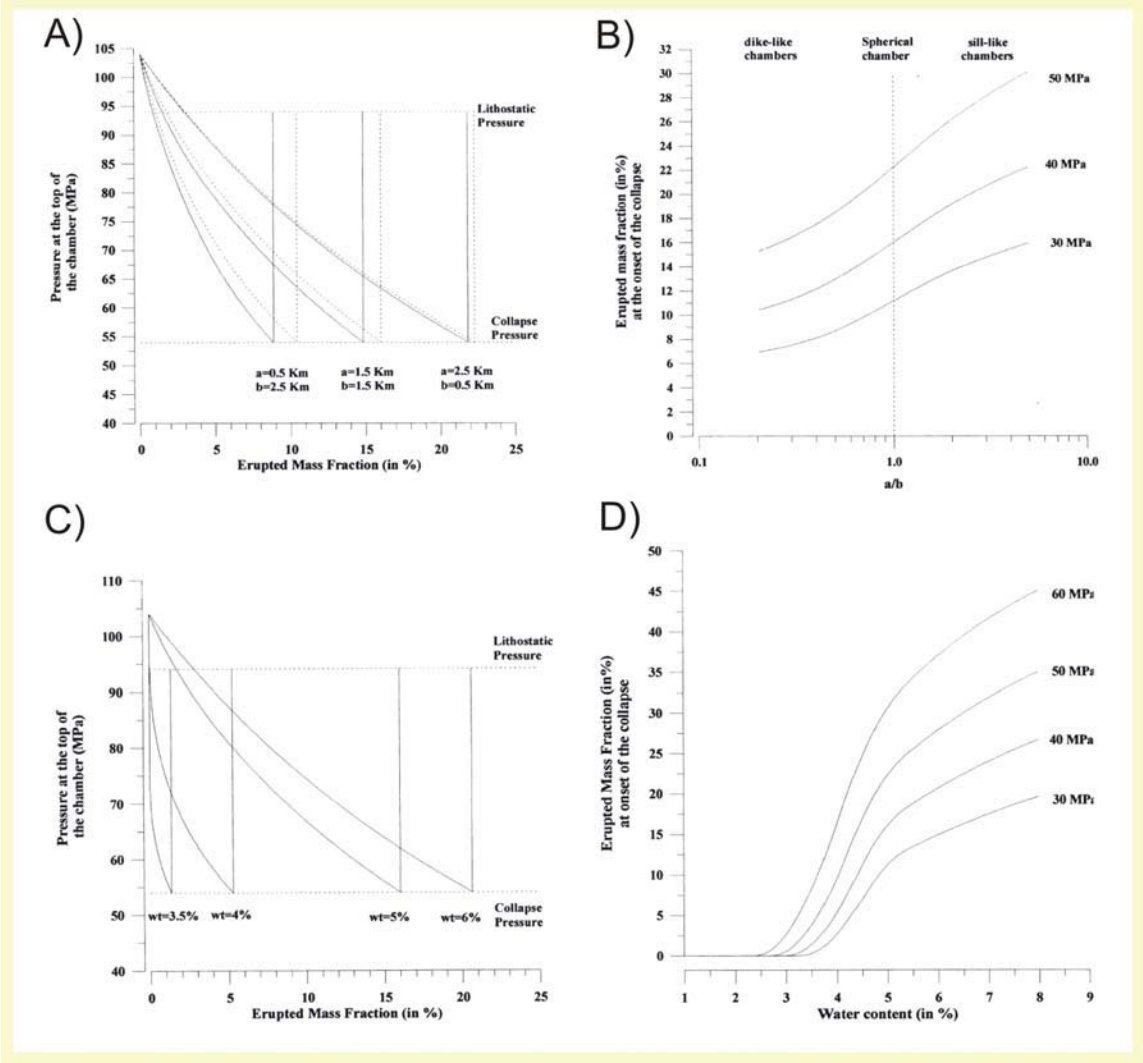

Fig. 4.4: Example of some of the results presented by Martí et al., 2000. **(A)** Magma pressure at the chamber roof as a function of the erupted mass fraction for different chamber geometries. Water content is constant and equal to 5 wt%. Dashed lines: results using cylindrical geometries (piston-like model). Continuous lines: results using ellipsoidal geometries with semi-axes **a** and **b**. **(B)** Erupted mass fraction at the onset of collapse as a function of the aspect ratio (**a/b**) of the chamber, considering volume constant. Results for different underpressure (ΔP_{COLL}) values. Water content is constant and equal to 5 wt%. **(C)** Magma pressure at the chamber roof as a function of the erupted mass fraction for different water contents. **(D)** Erupted mass fraction at the onset of collapse ($P_{TOP} = P_L - \Delta P_{COLL}$) as a function of the water content for different underpressure (ΔP_{COLL}) values. (Modified from Martí et al., 2000).

❖ MODELS TO DETERMINE STRESS CONDITIONS FOR NORMAL-FAULTS CALERA INITIATION

The main goal of these models is to provide information about the stress conditions leading to the initiation of faults controlling caldera collapses.

The models considered in this section study specifically the location of the minimum value of σ_3 and the maximum value of σ_1-σ_3 as well as the location at surface of the peak of maximum tension. These studies permit to investigate which geometrical configurations (chamber size, shape and depth) may induce a stress field suitable to initiate normal ring faults. Although these models do not consider the influence of any pre-collapse fracturing, some of them take into account the presence of regional tectonic stresses such as horizontal tensile or vertical compressional stresses, i.e. regional doming (e.g. Gudmundsson, 1998).

As shown on Table 4.1, these models may assume both possibilities, caldera collapse through magma chamber overpressure (e.g. Komuro et al., 1991; Gudmundsson et al. 1997; Gudmundsson, 1998) or underpressure (e.g. Folch and Martí, 2004). Logically, conditions for ring fault initiation (i.e. caldera collapse initiation) are the same regardless if wether the magma chamber is over- or underpressurized. We proceed to describe the most important results obtained with both type of models.

Results obtained considering overpressure inside the chamber

- **A ring fault may initiate at any depth between the margins of the chamber and the surface. If failure initiates at the margin of the chamber, the resulting dykes would relax the stress difference and possibly hinder the development of a ring fault. (Gudmundsson et al., 1997; Gudmundsson, 1998)**

- **Faults controlling caldera collapse commonly develop from tension fractures at the surface of the associated volcano and propagate to greater depths, toward the boundary of the associated magma chamber. At a certain depth these tensional ring fracture change into a normal- fault ring fractures. (Gudmundsson, 1998)**

- The formation of ring fractures is favoured depending on the magma chamber geometry, the assigned overpressure and the relationship of the latter with the regional stress (Fig. 4.4). A sill-like magma chamber with overpressure and regional doming generates the stress field adequate for ring fault formation. The area of the volcanic field subject to doming must be much larger than the cross-sectional area of the chamber; if not, the surface stresses peak above the centre of the chamber and do not favour the initiation of a ring fault. Other configurations such as spherical magma chambers only with overpressure or spherical magma chambers with overpressure lower than the horizontal tensile stress are not suitable for ring fault formation. In the first case, the maximum tensile and shear stresses at the free surface occur at the centre of the chamber, rather than its margins. In the second case, although the tensile and shear stresses at surface peak at a certain distance above the centre of the chamber, the maximum tensile stress occurs at the boundary of the chamber at the point nearest to the surface. (Gudmundsson et al., 1997; Gudmundsson, 1998)

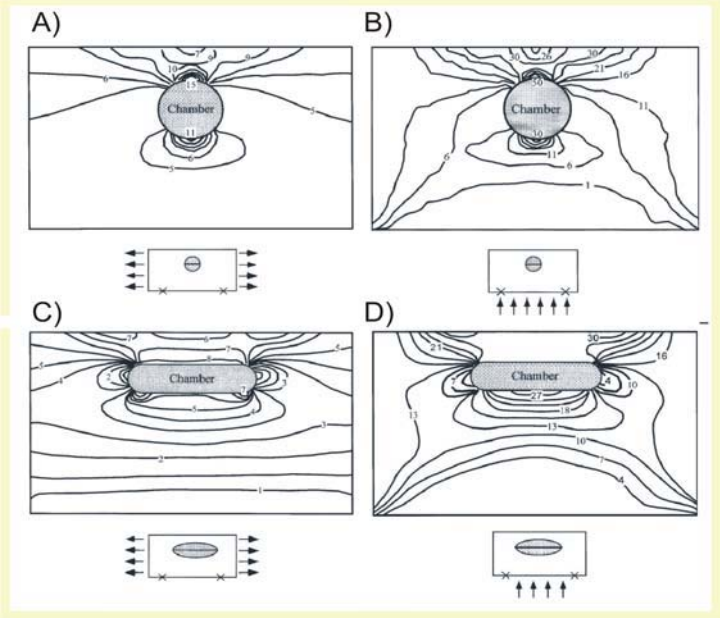

Fig. 4.5: Boundary-element results showing the contours of the maximum principal tensile stress in MPa. Models simulating a magma chamber subject to remote horizontal tensile stress. Two chamber reservoir shapes have been considered: spherical shape **(A)** and sill-like **(C)**. The other two sketches represent the results of models emulating a magma chamber under the effects of a magmatic overpressure in a reservoir located at the base of the volcanic field containing the magma chamber. Two different chamber reservoir shapes have been considered: spherical shape **(B)** and sill-like **(D)**. (Modified from Gudmundsson, 1998).

Results obtained considering underpressure inside the chamber

- Some authors (e.g. Gudmundsson et al., 1997; Gudmundsson, 1998) affirm that for spherical magma chambers subjected to underpressure the tensile stress at surface is much

smaller than the underpressure in the chamber. The maximum tensile stress would be too small to initiate fractures. The maximum shear stress occurs at the centre of the chamber but not on a suitable location for the initiation of normal fault calderas. However, varying the magma chamber eccentricity and for certain roof aspect ratio values, tensional stresses at surface increase, and a low magma chamber underpressure may produce a tensile peak at surface sufficient to induce rupture and favour ring fault formation. Furthermore, the results related to the variation of the value of underpressure show that the position of the peak of maximum tensile stress at surface remains invariant when changing the chamber underpressure and that its value varies linearly with pressure variations. Moreover, considering different magma chamber shapes it can be observed that for the same underpressure, the maximum value of tensile stress at surface decreases when increasing the chamber eccentricity e (D/H).

- **The formation of ring fault calderas may be governed by two different mechanisms strongly controlled by the geometry (eccentricity) and the roof aspect ratio of the associated magma chamber (Folch and Martí, 2004).**

  Mechanism A (Fig. 4.6 Region A):

  - Ring faults form as a consequence of the flexural bending of the chamber roof.
  - This would be the mechanism related to the formation of large plate-subsidence calderas, without necessary previous cycles of inflation-deflation.
  - Low chamber underpressures would be able to set up a collapse, since shear stresses at the outermost chamber walls and tensile stresses at surface are greater than the underpressure itself.
  - Only a very small volume fraction of the chamber needs to be extruded before the critical set up condition for collapse is reached.
  - Geometries of chambers in region A seem unlikely to support important loads without bending.

Mechanism B (Fig. 4.6 Region B):

- Mechanism related to small to moderate size collapse calderas, commonly associated with the evolution of large stratovolcanoes.

- The formation of the faulting system is more complex and history dependent.

- The collapse mechanism is similar to that found in the analogue models and may require previous fracturing and higher chamber decompression because chamber geometry does not favour an adequate stress field.

- For caldera collapse to occur it is necessary the extrusion of a great volume fraction of the chamber.

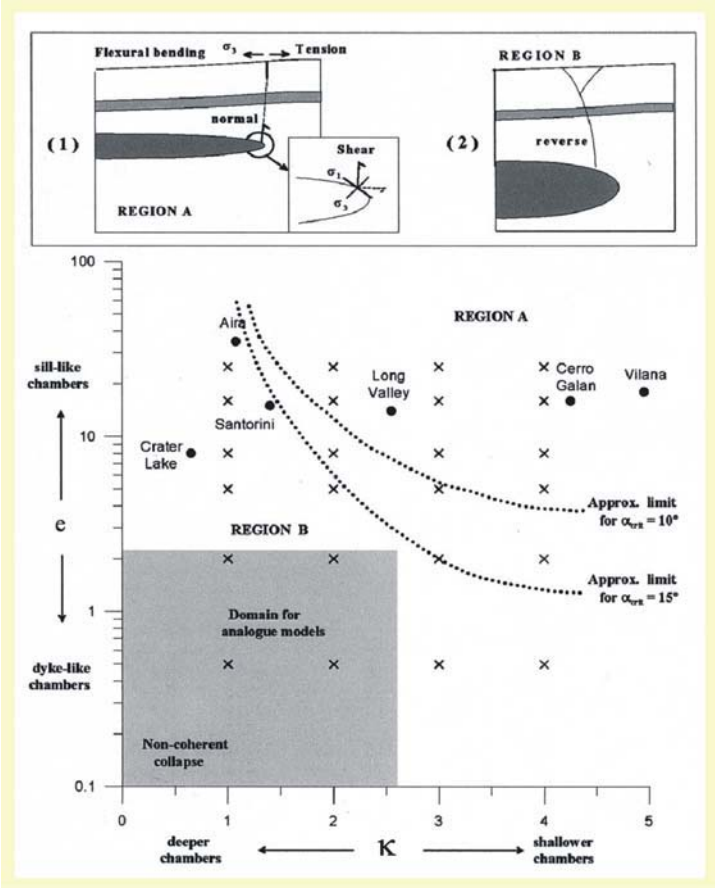

Fig. 4.6: Summary of simulation performed by Folch and Martí, 2004. Chamber configurations are plotted using a small cross in terms of the dimensionless parameters κ (**D**/**2P**) and e (**D**/**H**) (the latter in logarithmic scale). Cases that verify the conditions for ring fault formation lay in region A, whereas the rest lay in region B. The approximate critical limit that separates these two regions is marked using a dotted line for two different values of fault dip angle α_{CRIT}. The domain for which results of analogue models exist is indicated in grey. The position in the diagram of some documented collapse calderas is also shown using black dots. Topinset : schematic representation, not at scale, of the ring fault structure suggested by: (1) numerical experiments for region A, and (2) experimental models for region B. (Modified from Folch and Martí, 2004)

❖ MODELS THAT PREDICT FAULT LOCATION USING NON-ELASTIC RHEOLOGY

The principal objective of these works is to investigate the formation and deep geometry of the caldera faults, and the relationships between the magmatic system and the surface features of ash flow calderas. One of these models (Gray and Monaghan, 2004) includes a fracture model that allows following the growth of fractures under stress. Furthermore, the other models (Burov and Guillou-Frottier, 1999; Guillou-Frottier et al., 2000) are able to study the thermal regime at depth, which may alter crustal rheology and physical rock properties, and consequently, influence fracture formation and development.

In short, the calculations provide stress and thermal regimes versus time around the magma chamber and its vicinity, prediction of fault location and geometry, and directions of the potential brittle failure zones around the magma reservoir. The main controlling factors considered in these models are the regional stress field, the reservoir geometry and the roof aspect ratio R. The principal results obtained by Burov and Guillou-Frottier (1999) and Guillou-Frottier et al. (2001) may be summarized as follows:

Caldera collapse in the absence of the regional stress field and with a steady temperature field

Static conditions for caldera snapping following an analytical assessment

- The bending of the magma chamber roof should mostly results in localized faulting at the places of highest flexure. Furthermore, the maximum values of flexural stress inside the caldera roof are reached at the borders of its upper surface. In any case, the roof breaks when the flexural stress is greater than the local brittle rock strength, which is much lower at surface than at the brittle-ductile interface with the magma chamber. Moreover, the larger the caldera, the smaller the force or load needed to break it at the borders (Burov and Guillou-Frottier, 1999).

Coupled thermomechanical numerical models

- During the uplift stage, overpressure results in flexural uplift of the caldera roof causing bending. Roof bending results in the failure at the borders, the initiation of normal inclined border faults or reactivation of the first formed faults during the previous uplift. The subsidence of the roof is limited by the inward geometry of the cover. A later snapping of the roof in a vertical direction, allows the piston like subsidence. Consequently, the model predicts two groups of faults: inclined primary (initiated during the flexural stage) and subvertical secondary (initiated during overloading and subsidence) faults .

- Inclined normal faults may be initialised at the surface during the subsidence phase or at depth during the possible uplift phase (in this case they first appear as inverse faults) and propagate upward to the surface .

- Magma chamber geometry controls the mechanism of collapse. In fact, the number and location of faults depend on the magma chamber eccentricity e $(\mathbf{D}/\mathbf{H})$. For e values lower than 2.4 no border faults appear because the external load is balanced by the strength of the underlying crust. Moreover, during the initial stages of large calderas (e >3), an upward caldera roof bending precedes the collapse due to the overpressure inside the chamber. Consequently, the flexural stress concentrates at the upper corners of the magma chamber, resulting in the formation of inverse inclined border faults propagating from the top to the bottom of the magma roof, which inclination is controlled by the friction angle. Furthermore, with a larger magma chamber aspect ratio, internal embedded faults are created.

Caldera collapse in the presence of the regional stress field and with a steady temperature field

- The presence of far-field stresses can significantly modify the distribution and geometry of faulting. Regional extensional stresses shift the locations of the zones of minimal and maximal bending stresses, leading to the formation of multiple faults near the centre of the caldera floor. Consequently, regional extension favours the occurrence of deep faulting centred over the magma chamber roof. As long as the extension continues, the faults

propagate from the centre to the borders and create a wider dispersed fault zone. With extension fractures develop at a more vertical angle.

Caldera collapse in the absence of the regional stress field and with a non-steady temperature field

- The main thermal effects that influence the collapse process are heat diffusion from the hot magma reservoir and thermal blanketing due to the presence of the insulating ignimbritic cover. The magma chamber creates a ductile "aureole" around itself, delineated by a brittle-ductile transition (BDT) that can be considered as the "thermomechanical" geometry of the magma chamber, in contrast to a more common chemical/lithological boundary or definition. The transition between "hot" (ductile) to "cold" (brittle) may limit the propagation of the brittle faults and cracks. In fact, brittle deformation follows this boundary without penetrating inside, except for some major faults. The BDT is clearly marked in the models by a subhorizontal fracture zone in the middle of the cover, thus delineating a "mechanical magma chamber". Although the location of the border faults does not change significantly, their geometry is affected. In fact, lateral border faults are inward-dipping at the surface but outward-dipping at depth. Furthermore, the insulating ingnimbritic cover tends to overheat the lower part of the magma chamber roof, which becomes even more ductile. This considerably reduces the effective mechanical thickness of the roof, as well as the depth and inclination of the border faults.

IV.4.2 Summary of previous results

In order to facilitate the comprehension and understanding of the rest of this chapter, we consider necessary to present a schematic summary of the most important aspects commented in this section. Figure 4.7 offers a sketch summing up the different aspects and topics commented in this section concerning the state of the art of collapse calderas mathematical models.

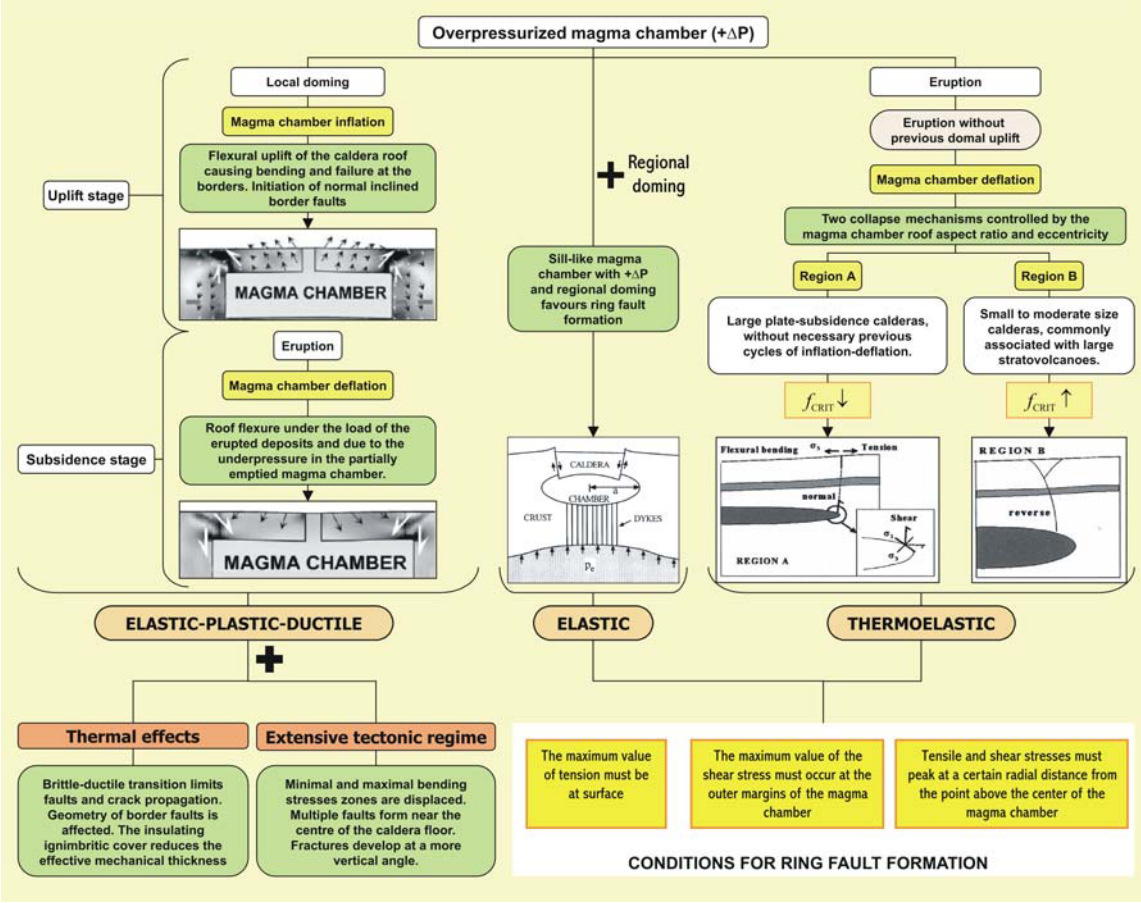

Fig. 4.7: Sketch summing up the different aspects and topics commented in this section concerning the state of the art of collapse caldera mathematical models. f Erupted magma chamber volume fraction necessary to trigger caldera collapse.

IV.4.3 Description of the restrictions

Before discussing the results obtained by theoretical/mathematical models and their geological implications, it is necessary to determine their main restrictions, and if possible, to try to minimize their effect in future models.

In this section we describe the different restrictions and limitations found in the mathematical models applied to the study of collapse calderas. These vary from model to model, and are principally dependent on the design of the physical model and the considered rheological behaviour for the host rock. The main restrictions are:

- **Homogeneous host rock**
- **Fluid dynamics and rock mechanics are uncoupled**
- **Impossibility of dike injection**
- **Absence of volcanic edifice**
- **Failure considered only under extensional stresses**
- **No regional faults or previous formed structures**
- **Host rock rheology**

❖ HOMOGENEOUS HOST ROCK

Similar to analogue models, most of the existing mathematical models have been carried out with homogenous host rock. As mentioned before, this is not a correct approximation to the natural system, since country rocks around magma chamber are normally heterogeneous in composition. Lithological heterogeneities and structural discontinuities can influence the stress field and consequently, fracture propagation and structure development (e.g. Gudmundsson and Brenner, 2005). Therefore, it is important to introduce stratigraphic heterogeneities in order to approach mathematical models, as much as possible, to reality. This is a relevant point when studying and applying mathematical models, as they are very sensitive to changes on rock properties.

❖ FLUID DYNAMICS AND ROCK MECHANICS UNCOUPLING

The main problem of the existing models about caldera collapse processes is that fluid dynamics and rock mechanics are in all cases uncoupled. In an ideal case, all physical processes should be simulated simultaneously, as processes occurring inside the chamber may affect or are depending on those taking place in the country rock and vice versa. However, since each region of the system is physically distinct from the other, coupling all processes is a very difficult or almost impossible task. Nevertheless, this should be one of the principal objectives of future complex mathematical modelling.

❖ NO DIKE INJECTION SIMULATION

None of the analysed mathematical models can simulate dike injection during the collapse or tumescence process. However, the possibility of dike injection is important during magmatic processes because it can regulate the equilibrium inside the magma chamber (see section III.2.3) (Gudmundsson, 1998). For example, in situations of overpressure, dike intrusion can decrease the magma chamber pressure and may avoid the initiation of an eruptive event. Furthermore, the impossibility of simulating dike injection has other consequences. On the one hand, dike intrusions may significantly modify the physical properties of the country rock as, for example, its tensile or shear strength values. Evidently, this will affect fault nucleation and propagation. Moreover, another important problem is that some interpretation of results obtained may be misinterpreted. Whereas some authors maintain that ring fault or other collapse controlling structures develop from the top of the magma chamber to the surface (e.g. Gray and Monaghan, 2004), others hold that ring fault nucleation at depth is not possible as any magma chamber rupture would lead to a dike intrusion (e.g. Gudmundsson, 1998). Of course, this kind of controversies will last until the application of a model, which considers also dike injection.

❖ ABSENCE OF VOLCANIC EDIFICE

The stress field around a magma chamber is one of the most important controlling factors of caldera collapse processes. In natural systems the stress field near a magmatic reservoir has contributions from three main sources: the stress perturbation associated with the magma chamber itself (over- or underpressure), the regional or far-field stress and finally, the topography loading stresses (Muller et al., 2001). In fact, at some volcanic complexes the topographic load may be the principal upper-crustal stress field and is able to modify the regional fault patterns, increase the fault throw and induce extension (Lavalleé et al., 2004, and references therein). Despite this fact, previous commented mathematical models use a flat horizontal topography, although calderas usually form in volcanic fields with significant topographic relief. Nowadays, mathematical models related to caldera collapse processes, which consider in their systems the presence of a volcanic edifice are inexistent. There only exist some works studying the effect of volcanic edifice on magma chamber emplacement and dike propagation (e.g. Pinel and Jaupart, 2000, 2003, 2004)

❖ FAILURE ONLY UNDER EXTENSIONAL STRESSES

Obviously, this restriction is limited to those models that are able to reproduce failure (e.g. Gray and Monaghan, 2004). Due to the complexity of fracture analysis, nowadays, programs computing brittle fracture propagation are restricted to failure under extensional stresses. In fact, shear components in this kind of models may destabilize the process and the system fails. Of course, the main problem is that although faults controlling caldera collapses are tensional at surface these became shear fractures at depth. Consequently, mathematical models are not able to follow them. However, faults generated at the magma chamber wall may develop to fluid-filled cracks which have a extensional component due to the fluid pressure, consequently these can be modelled as tensional fractures. However, the impossibility of simulating shear fractures slants the information of caldera collapse controlling structures, such as vertical ring faults.

❖ NO REGIONAL FAULTS OR PREVIOUS FORMED STRUCTURES

Another important restriction of previous commented models is that these are unable to introduce regional faults or previous formed structures. These mathematical models are not capable to simulate multicycling processes of inflation and deflation, although in some of them (e.g. Burov ang Guillou-Frottier, 1999) it is possible to observe the reactivation of structures formed during the uplift stages. However, the simulation of fault in these models is not possible. They follow fault propagation by looking at the stress distribution and the accumulated plastic strain, but they cannot register fractures in a strict sense. By contrast, those models able to follow and recreate brittle structures (e.g. Gray and Monaghan, 2004) do not introduce pre-existing regional structures. Clearly, the existence of regional faults or previous formed structures strongly affects the morphology (e.g. Silali – *Kenya*, Bosworth et al., 2003; Valles – *U.S.A*., Self et al., 1986) (see section II.2.2) and, in some cases, the mechanism of caldera collapse. Therefore, if mathematical models are not able to reproduce them these will be far away from simulating with accuracy natural systems. In these sense, model considering elastic rheology are too simplistic.

❖ HOST ROCK RHEOLOGY

The models presented in this section deal with different govern equations involving diverse rock rheologies. The main problem is that results obtained are highly conditioned by the selected host rock rheological behaviour. The most extended option is to assume that the crust behaves as a linear homogeneous elastic material, although the use of elastic behaviours to predict brittle rock strain is not very robust. However, those models using this rheology study, in general trends, the main factors controlling (e.g. magma chamber geometry, depth and volume) caldera collapse or the stress field conditions for the formation of ring-faults or in some cases also dikes, rather than to study fault or brittle failure structures in detail. Furthermore, the use of linear rheologies permits to work with the superposition principle of stress fields. However, the main problem appears when comparing results obtained for the different rheologies, which in some cases are completely opposite (Burov and Guillou-Frottier, 1999).

IV. 5 NEW MATHEMATICAL MODELS

IV.5.1 Objectives

The new mathematical models exposed in this work have several objectives. On the one hand, we want to reproduce some of the analogue experiments set out in this work and described in chapter III. This offers us the possibility to compare the results obtained using mathematical or analogue models and consequently, to detect additional restrictions of both methodologies.

The second aim of this section is to reproduce some of the mathematical models exposed in Folch and Martí (2004). On the one hand, we are going to study the influence of the selected geometrical setting (e.g. axial symmetric or three-dimensional) in the obtained results and the subsequent interpretation of the required stress field suitable to initiate normal ring faults. These models do not consider the influence of any pre-collapse fracturing or differential tectonic stress.

Apart from the mathematical models intimately related to caldera collapse processes, there is also the possibility of applying other types of mathematical models. These are not strictly related to collapse caldera processes but the results obtained are applicable to the study of collapse mechanisms and their controlling factors, as we will see in this section. In addition to the presentation of some new results of the models, we also want to point out that future mathematical works on collapse calderas have to consider the possibility of combining the results of other disciplines to go further in the investigations.

IV.5.2. Rheological model

IV.5.2.1 General aspects

Some authors tend to assume that during the course of a caldera-forming eruption, i.e. during the process of magma chamber decompression and subsequent initiation of ring-faults, the surrounding crust behaves as a linear homogeneous elastic

material (e.g. Folch and Martí, 2004). In our mathematical models we want to reproduce conditions as much closer as possible to natural rocks. Natural materials deform in a brittle fashion and have a Mohr-Coulomb behaviour. However, some problems appear when trying to simulate numerically brittle deformation and fracture. Although, there exist several commercial programmes able to reproduce fracture (e.g. ANSYS® , BEASY®, etc.), they present some problems depending on the considered fracture mode. In short, there are three different fracture modes I, II or II (Fig. 4.8) (Ramsay and Huber, 1983). The first one corresponds to a pure opening or tensile mode, the second to a sliding or in plane-shear mode and the third to a tearing or antiplane shear mode. Normally, the above commented programmes are able to reproduce mode I fractures but they present some problems when trying to reproduce mode II and III cracks. This is an important restriction when performing our models. As described in prior section, some fractures that appear in nature and in the models may be tensile but other have an important shear component (see section II.5.4). Consequently, it is very difficult to reproduce them numerically. As a result, we decide to simplify the calculus using also linear elasticity. We assume that the results obtained are approximated but as we will see these are considerably satisfactory. Nevertheless, at the end of the section, we will comment the restriction of the method.

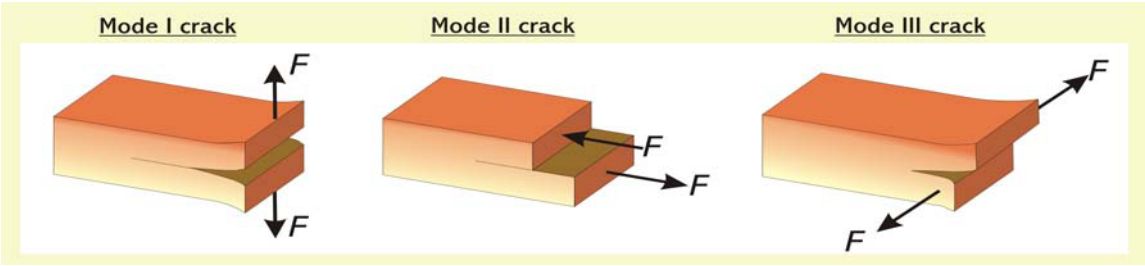

Fig. 4.8: Sketch of the three main fracture modes: Mode I is opening or tensile mode. The forces are perpendicular to the crack pulling the crack open. Mode II is sliding or in plane-shear mode. The forces are parallel to the crack. The crack surfaces slide over one another perpendicular to the leading edge of the crack. Mode III is tearing or antiplane shear mode. The crack surfaces move relative to one another and parallel to the leading edge of the crack (Modified from Ramsay and Huber, 1983).

IV.5.2.2 Linear elasticity

In this section we review the most important and relevant aspects concerning elasticity in order to facilitate the understanding of the results obtained and the subsequent discussion.

In short, elastic materials deform when a force is applied and return to their original shape when the force is removed. A linear, isotropic, elastic solid is one in which stresses are linearly proportional to strains and mechanical properties have no preferred orientations. The principal axes of stress and strain coincide in such a medium, and the connection between stress and strain can be conveniently written in this coordinate system as (Turcotte and Schubert, 2002).

$$\sigma_1 = (\lambda + 2G)\,\varepsilon_1 + \lambda\,\varepsilon_2 + \lambda\,\varepsilon_3 \quad [4.4]$$

$$\sigma_2 = \lambda\varepsilon_1 + (\lambda + 2G)\,\varepsilon_2 + \lambda\,\varepsilon_3 \quad [4.5]$$

$$\sigma_3 = \lambda\varepsilon_1 + \lambda\,\varepsilon_2 + (\lambda + 2G)\,\varepsilon_3 \quad [4.6]$$

where the material properties λ and the modulus of rigidity $\boldsymbol{G}$ are known as the Lamé parameters. Furthermore, σ_1 , σ_2 and σ_3 are the principal stresses. The state of stress at a point in a solid is completely specified by giving σ_{xx}, σ_{yy}, σ_{zz}, σ_{xy}, σ_{xz} and σ_{yz} or the orientation of the principal axes and the value of the principal stress (Fig. 4.9). In fact, it is possible to find three orthogonal axes such that all shear stress components are zero. The normal stresses on planes perpendicular to the principal axes are the principal stresses commonly denoted as σ_1 , σ_2 and σ_3 . By convention these are chosen such that $\sigma_1 \geq \sigma_2 \geq \sigma_3$. Thus, σ_1 is the maximum principal stress, σ_2 is the intermediate principal stress and σ_3 is the minimum principal stress (Turcotte and Schubert, 2002).

Additionally, Equations 4.4 – 4.6 can be also written:

$$\varepsilon_1 = \frac{1}{E}\sigma_1 - \frac{\nu}{E}\sigma_2 - \frac{\nu}{E}\,\sigma_3 \quad [4.7]$$

$$\varepsilon_2 = -\frac{\nu}{E}\,\sigma_1 + \frac{1}{E}\,\sigma_2 - \frac{\nu}{E}\,\sigma_3 \quad [4.8]$$

$$\varepsilon_3 = -\frac{\nu}{E}\,\sigma_1 - \frac{\nu}{E}\sigma_2 + \frac{1}{E}\sigma_3 \quad [4.9]$$

where $\boldsymbol{E}$ and ν are material properties known as the Young's modulus and the Poisson's ratio, respectively. Consequently, the elastic behaviour of a material can be characterized by specifying either λ and $\boldsymbol{G}$ or $\boldsymbol{E}$ and ν. Throughout this work, material properties will be specified using the Young's modulus $\boldsymbol{E}$ and the Poisson's ratio ν.

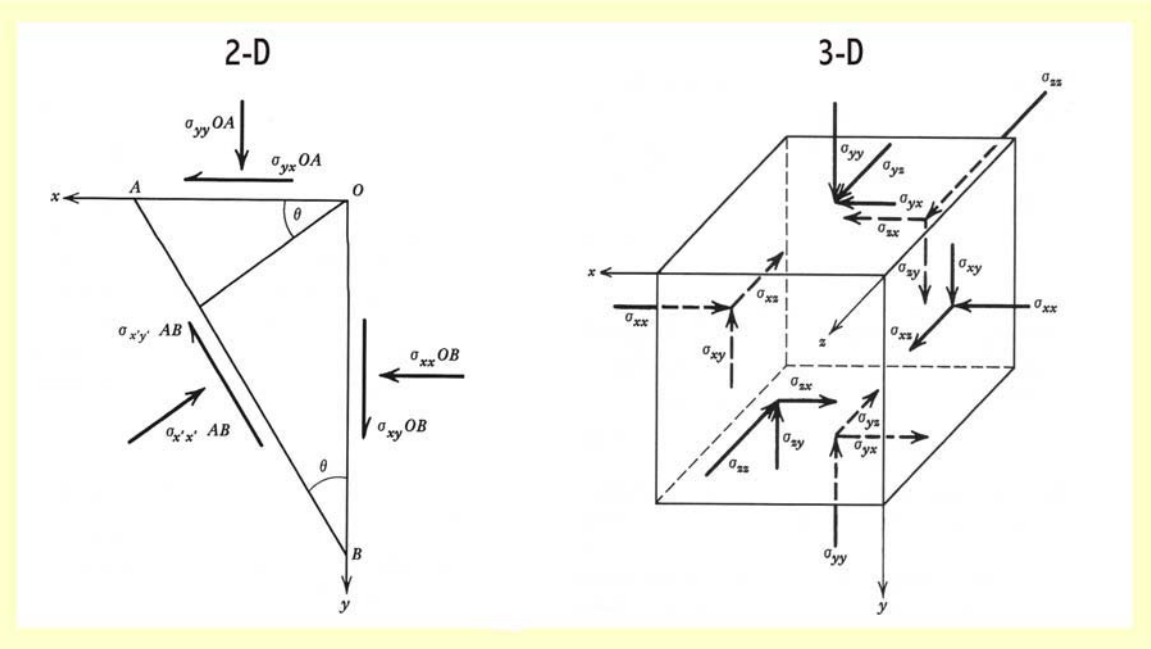

Fig. 4.9: Stress components in 2-D and 3-D (Modified from Turcotte and Schubert, 2002).

IV.5.3 Mathematical reproduction of analogue models

IV.5.3.1 General aspects and objectives

The number of studies combining mathematical and analogue models is very low (e.g. Komuro et al., 1984; Roche and Druitt, 2001). However, we will see that this seems to be the appropriate way to a better understanding of collapse caldera processes. In this section we reproduce numerically some of the analogue experiments of chapter 3. Thus, we can compare the results obtained with both kinds of models and to infer from their differences, the restrictions and limitations of both methodologies. Results obtained are divided in two different parts depending on the kind of reproduced analogue models: balloon or silicone.

IV.3.3.2 Reproduced experiments

Since the reproduction of all the experiments would be too time-consuming and excessive, it is preferable to concentrate on the most representative and significant ones.

In tables 4.2 and 4.3 are listed the selected experiments considering balloon or silicone reservoir as magma chamber analogue, respectively.

For balloon analogue models we choose three D-type experiments (experiments without topography performed with the experimental set-up I b) (Fig. 3.12). In order to facilitate the comprehension of the results and observations presented in the next sections, Table 4.2 also summarizes the main input parameters and, measured and calculated values of these four balloon experiments. With the reproduction of these experiments we can study the influence of the roof aspect ratio **R**.

For silicone analogue models we choose eight experiments (Table 4.3): five with flat and four with curved silicone reservoir (see section III.3.5). Table 4.3 also includes the main input parameters and, measured and calculated values of these silicone experiments. With their mathematical reproduction we can study the influence **R** and the effect of the reservoir eccentricity ***e***.

A)

Experiments	INPUT PARAMETERS									
	P (cm)	R	H (cm)	D_{max} (cm)	D_{min} (cm)	t (s)	% V	He_1 (cm) / He_2 (cm)	α / β	Ra_1 (cm) / Ra_2 (cm)
								7.4	37º	10
D-1	6	0.34	14	20	16	160	50	/	/	/
D-4	12.5	0.52	15.5	25	23	290	64	/	/	/
D-5	17.5	0.84	15	22	20	310	86	/	/	/

B)

Experiments	MEASURED AND CALCULATED VALUES									
	R	S_p (cm)	S_s (cm)	P-D_p (cm)	P-D_{smax} (cm)	P-D_{smin} (cm)	OL-D_{max} (cm)	OL-D_{min} (cm)	N-D_{max} (cm)	N-D_{min} (cm)
D-1	0.34	n.c	n.c.	n.c.	13	11	33	26	13	11
D-4	0.52	n.c	n.c.	n.c.	18	15	59.44	57.50	18	15
D-5	0.84	n.c	n.c.	n.c.	17.5	13.5	55	47	17.5	13.5

Table 4.2: Sections of tables 3.3 and 3.6. List of the analogue experiments reproduced numerically. **(A)** Input parameters of the analogue models. **(B)** Relevant measured or calculated parameters in balloon analogue models. α Slope of the volcanic cone 1; β Slope of the volcanic cone 2; **D_{max}** Balloon maximum diameter; **D_{min}:** Balloon minimum diameter; **H** Balloon height; **He_1** Volcanic cone height; **He_2** Height of the volcanic cone 2; **n.c.** No calculable or measurable value due to experimental reasons or visual problems; **N-D_{max}** Maximum diameter of the non-deformed area; **N-D_{min}** Minimum diameter of the of the outer limit of the collapse; **OL-D_{max}** Maximum diameter of the outer limit of the collapse; **OL-D_{min}** Minimum diameter piston diameter at surface; **P** Balloon depth; **P-D_{smax}** Maximum piston diameter at surface; **P-D_{smin}** Minimum piston diameter at surface; **P-D_p** Piston diameter at depth; **R** Roof aspect ratio defined as R= $[(P+He1)(D_{max}+D_{min})]/2D_{max}D_{min}$ (Roche and Druitt, 2001); **Ra_1** Radius of the volcanic cone 1; **Ra_2**: Radius of the volcanic cone 2; **S_p** Subsidence at depth; **S_s** Subsidence at surface; **t** Duration of the experiment; **V** Total extruded volume of water from the balloon.

A)

Experiment	INPUT PARAMETERS				
	P (cm)	D (cm)	t (min)	Shape	R
SIL-1	2	10	150	FLAT	0.2
SIL-2	3	10	140	FLAT	0.3
SIL-3	4	10	180	FLAT	0.4
SIL-7	7	10	136	FLAT	0.7
SIL-8	8	10	180	FLAT	0.8
SIL-9	3.3	10	100	A= 1.7 cm e = 2. 94	0.33
SIL-10	2.2	10	60	A= 2.8 cm e = 1.79	0.22
SIL-11	2.5	10	n.c.	A= 3.5 cm e = 1.43	0.25
SIL-12	3.4	10	75	A= 4.6 cm e = 1.08	0.34

B)

Experiments	MEASURED AND CALCULATED VALUES					
	R	S_p (cm)	S_s (cm)	N-D (cm)	OL-D (cm)	EXT-W (cm)
SIL-1	0.2	0.83	0.83	7.4	9.8	1.20
SIL-2	0.3	0.76	0.76	6	10.5	2.25
SIL-3	0.4	1.4	1.4	5	9.8	2.40
SIL-7	0.7	1	0.8	2.75	5.7	1.48
SIL-9	0.33	1.46	0.85	5.54	10.7	2.58
SIL-10	0.22	n.c.	0.92	5.7	10.17	2.23
SIL-11	0.25	0.8	0.8	6.12	11.51	2.70
SIL-12	0.34	2.6	2.6	2.11	4.07	0.98

Table 4.3: Sections of tables 3.10 and 3.13. List of the analogue models reproduced numerically. **(A)** List of the input parameters of the considered analogue silicone models **(B)** Relevant measured or calculated parameters. **A** Silicone reservoir height**; D** Silicone reservoir diameter; e Silicone reservoir eccentricity defined as 0.5×D/A (e =1 implies an hemispheric silicone reservoir); **EXT-W** Width of the external area of flexure and extension; **n.c.** No calculable or measurable value due to experimental reasons or visual problems; **N-D** Diameter of the non-deformed area; **OL-D** Diameter of the outer limit of the collapse; **R** Roof aspect ratio= P/D; S_p Subsidence at depth; S_s Subsidence at surface; **T** Roof thickness; **t** Duration of the experiment.

IV.5.3.3 Geometrical setting

IV.5.3.3.1 General aspects

Prior to the elaboration of any mathematical models it is necessary to define the required geometrical setting. The first step is to establish the dimensions of the geometry. As we will see, depending on the selected dimensions the results obtained are

slightly different. In order to illustrate the importance of the geometrical setting and its influence on the results obtained, we find appropriate to analyse a simple example. We consider a cube of size 1 × 1 × 1 length units (LU) defined in accordance with a cartesian *x*, *y*, *z* coordinate system. We fixed its basis, i.e. the displacement $\boldsymbol{u}$ in all directions is equal to zero ($\boldsymbol{u_x = u_y = u_z = 0}$) and assign an excess pressure of 10^3 pressure units (PU) on its top (Fig. 4.10 A). The lateral surfaces are traction free. Numerically, we have the possibility of a two- dimensional (2-D), a three-dimensional (3-D) or an axial symmetrical model (AS) (Fig. 4.10 B, C and D, respectively).

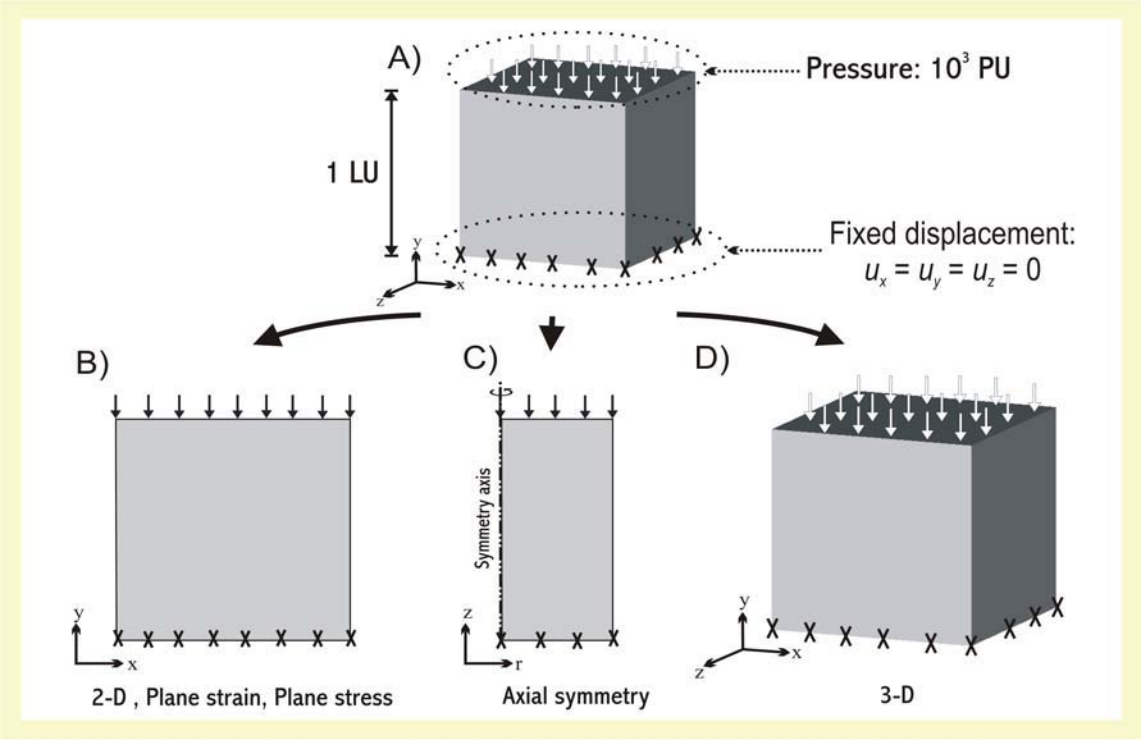

Fig. 4.10: Sketches of the different possibilities of modelling a cube of size 1 × 1 × 1 length units (LU) with fixed basis, i.e. the displacement *u* in all directions is equal to zero ($u_x = u_y = u_z = 0$) and subjected to an excess pressure of 10^3 pressure units (PU) on its top. **(A)** Sketch of the example's geometry and boundary conditions. **(B)** Sketch of the example's geometry in 2-D with the assigned boundary conditions. **(C)** Sketch of the example considering axial symmetry. **(D)** Sketch of the 3-D solution of the example with the prescribed boundary conditions.

In order to simplify the geometry and to avoid time-consuming calculus we can select a 2-D model (Fig. 4.10 B). Consequently, the geometrical setting is a 1 × 1 LUs square with an excess pressure of 10^3 PU at its top and fixed displacement at its basis ($\boldsymbol{u_x = u_y = 0}$). When dealing with 2-D we can choose between "pure" 2-D, "plane strain" or "plane stress" model.

In a "pure" 2-D model the state of stress is two-dimensional. In this case, surface forces and strain in the *z* direction is zero, and none of the others surface forces varies in the *z* direction. Consequently, the three independent components of stress are the normal stress σ_{xx}, σ_{yy} and the shear stress σ_{xy} .

In a "plane stress" state of stress one component of principal stress is zero, i.e. $\sigma_3 = 0$, $\sigma_1 \neq 0$, $\sigma_2 \neq 0$. The situation is sketched in Figure 4.11. The geometrical setting is considered then as a very thin and infinitely wide plate. The strain according to Equations 4.7- 4.9 are:

$$\varepsilon_1 = \frac{1}{E}(\sigma_1 - \nu\,\sigma_2) \qquad [4.10]$$

$$\varepsilon_2 = \frac{1}{E}(\sigma_2 - \nu\,\sigma_1) \qquad [4.11]$$

$$\varepsilon_3 = -\frac{\nu}{E}(\sigma_1 + \sigma_2) \qquad [4.12]$$

In the case of "plain strain", $\varepsilon_3 = 0$, and ε_1 and ε_2 are not zero. Figure 4.11 illustrates a "plain strain" situation. The geometry of Figure 4.11 B would correspond to a section of infinite long prismatic bar. Here Equations 4.4 – 4.6 are reduced to:

$$\sigma_1 = (\lambda + 2G)\,\varepsilon_1 + \lambda\,\varepsilon_2 \qquad [4.13]$$

$$\sigma_2 = \lambda\varepsilon_1 + (\lambda + G)\,\varepsilon_2 \qquad [4.14]$$

$$\sigma_3 = \lambda(\varepsilon_1 + \varepsilon_2) \qquad [4.15]$$

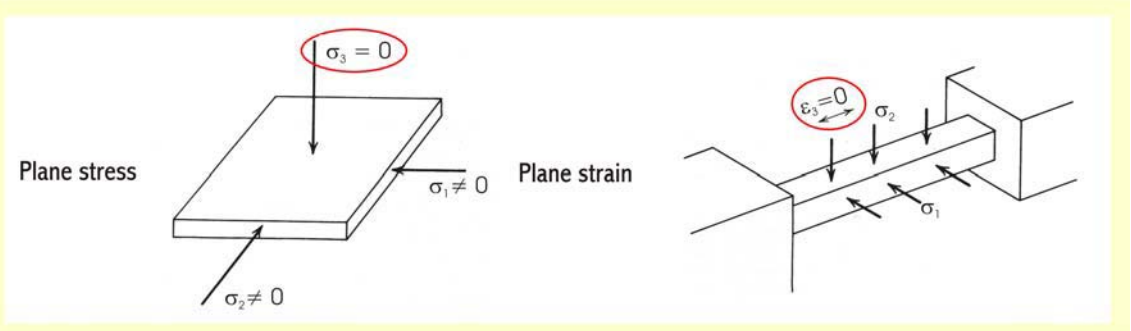

Fig. 4.11: Sketches representing the main characteristics of a "plane stress" and "plane strain" situations. In a "plane stress" state of stress one component of principal stress is zero, i.e. $\sigma_3 = 0$, $\sigma_1 \neq 0$, $\sigma_2 \neq 0$. In the case of "plain strain", $\varepsilon_3 = 0$, and ε_1 and ε_2 are not zero (Modified from Turcotte and Schubert, 2002).

On the other hand, if we assume axial symmetry the geometry becomes a 0.5 × 1 LUs rectangle with an excess pressure of 1 PU at its top and fixed displacement at its basis ($\boldsymbol{u_x = u_y = 0}$). The required condition along the symmetry axis is $\boldsymbol{u_x = 0}$. Evidently, this geometrical setting does not provide exactly the solution for a cube. If we rotate the rectangle on the symmetry axis we obtain a cylinder of radius 0.5 LU and height 1 LU. In this case the six independent components of stress are $\sigma_{rr}, \sigma_{zz}, \sigma_{\theta\theta}, \sigma_{rz}, \sigma_{r\theta}$, and $\sigma_{z\theta}$.

More mathematically complicated but also more accurate is to reproduce the cube three-dimensionally. Consequently, the six independent components of stress are the normal stress $\sigma_{xx}, \sigma_{yy}, \sigma_{zz}$ and the shear stresses σ_{xy} , σ_{xz} and σ_{yz} .

In order to find out the consequences and implications of choosing one of the different numerical possibilities proposed in Figure 4.10 we proceed to compare the results obtained when solving the exposed example (Fig. 4.10 A) with the different approaches. For that we use arbitrary values of Young's modulus $\boldsymbol{E}$ = 1 PU and Poisson's coefficient ν = 0.25. It has been checked that the values of these two physical properties do not affect the results.

In order to investigate the effect of the different mathematical approaches we study the values of displacements and principal stresses σ_1 and σ_3 along a vertical axis passing through the centre of the cube or square (depending of the dimensions of the problem) or along the symmetry axis if the model has axial symmetry. Results obtained are exposed in Figure 4.12. We can observe that the displacement values are practically independent on the selected model. By contrast, the distribution of the values of σ_1 and σ_3 change considerably. Especially interesting is the comparison between 3-D and axial symmetry. Whereas the results of the displacements in of both models are equivalent (differences are due to the mesh quality), the profiles of the principal stresses σ_1 and σ_3 are different. Therefore, we have to be cautious when interpreting the results obtained with both types of models.

Remember that collapse caldera a process modelling is specially focused on the distribution of σ_3 at surface therefore, the selection of the approach (2-D, plane stress, plain stress, axial symmetry or 3-D) is of high relevance. We release also in this section that this phenomenon is highly dependent on the geometrical setting of the model.

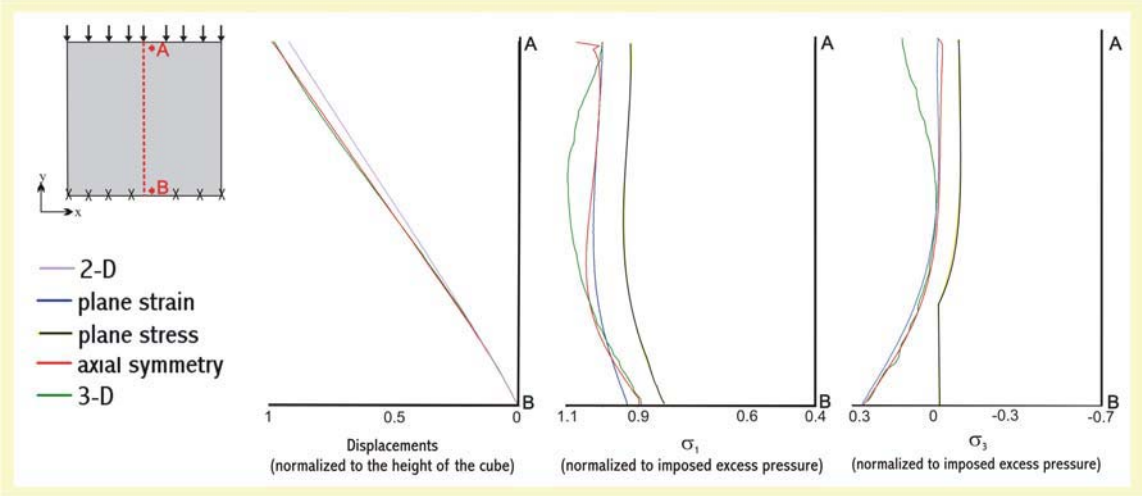

Fig. 4.12: Results obtained when solving the proposed model of Figure 4.10 A with the different mathematical approaches. We include in the Figure the distribution of the displacement values, σ_1 and σ_3. Values of displacement are normalized to the height of the cube 1 LDU and values of stress to the imposed excesses pressure of 10^3 PU.

IV.5.3.3.2 Geometrical setting for reproducing mathematically balloon models

Figure 4.13 sketches the experimental devices of balloon analogue modes and the corresponding geometrical setting of the performed mathematical models. Evidently, the mathematical models have to reproduce the most important components of the experimental set-up: the host rock analogue (dry-quartz sand), the magma chamber analogue (latex balloon) and the rigid walls of the tank where the analogue models are performed, which may probably introduce some edge effects that have to be analysed.

We used two geometrical setting depending if we consider two- or three dimensions. We want to reproduce the experiments with both approaches and in order to detect differences in the results due to the selection of the geometrical setting.

The 2-D geometrical setting (Fig. 4.13) corresponds to a rectangle (coloured in grey) of 60 or 100 cm width depending on the reproduced model. The height of this rectangle is equivalent to the thickness of the sand-pack **T** in each experiment. This geometry implies that the computational domain corresponds to the sand in the analogue experiments. The rigid walls of the tank (wood or glass) are reproduced fixing the laterals and the base of this rectangle. Small black crosses indicate the boundary condition of fixed zero displacement in any direction ($\boldsymbol{u}_x = \boldsymbol{u}_y = \mathbf{0}$). The magma chamber analogue is reproduced by an elliptical hole (white) in the rectangle. The upper part is free.

The 3-D geometrical setting consists of a prism with fixed laterals and base. The magma chamber analogue corresponds to an ellipsoidal hole and the upper surface is free (Fig. 4.13).

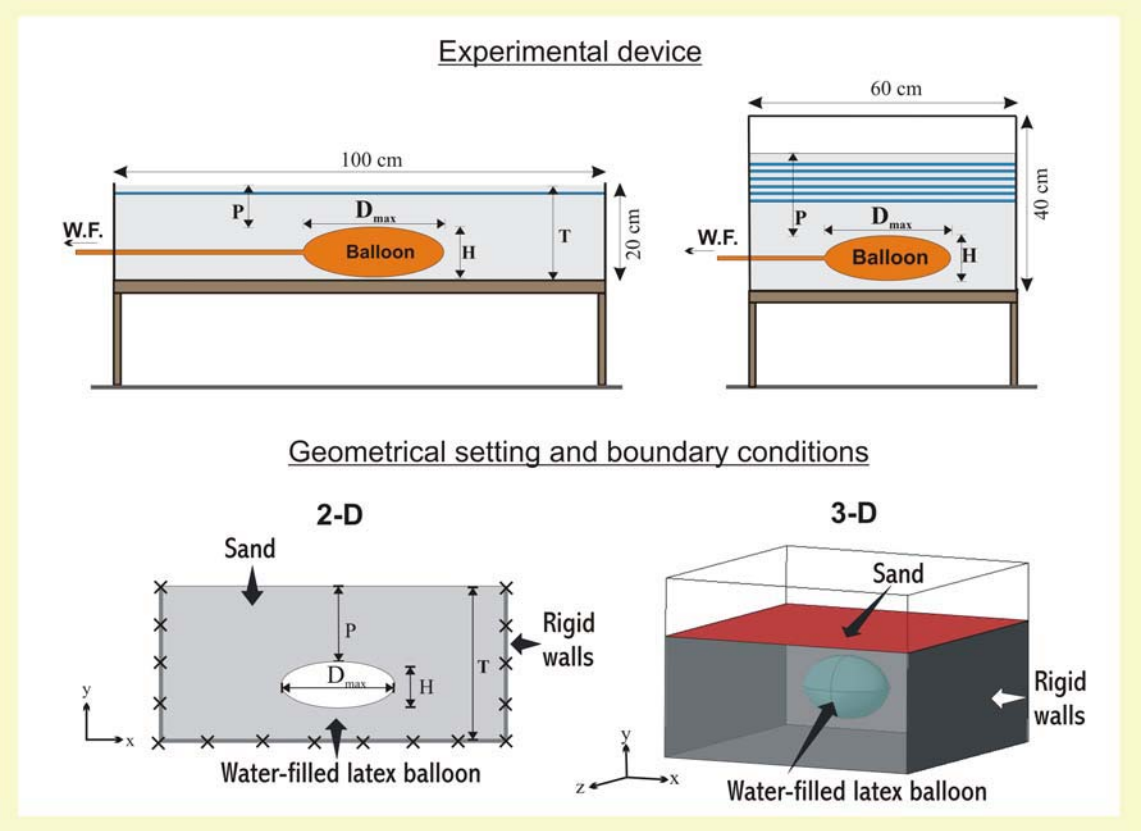

Fig. 4.13: (Top) Sketch of the experimental devices reproduced numerically **(Bottom)** Geometrical setting and boundary conditions of the performed mathematical models. The 2-D geometrical setting corresponds to a rectangle with fixed laterals and base ($u_x = u_y = u_z = 0$). The magma chamber analogue is reproduced by an elliptical hole (white) in the rectangle. The upper part is free. The 3-D geometrical setting consists of a prism with fixed laterals and base (grey). The magma chamber analogue corresponds to an ellipsoidal hole (coloured in blue) and the upper surface is free (red). **D_{max}** Balloon maximum diameter; **H** Balloon height; **P** Balloon depth; **T** Sand-pack thickness; **W.F.** Water flow direction.

IV.5.3.3.3 Geometrical setting for reproducing numerically silicone models

Figure 4.14 sketches the experimental device of those analogue modes carried out with a silicone reservoir as magma chamber analogue. We also represent the corresponding geometrical setting of the performed mathematical models. Similar to the reproduction of the balloon models, the most important components of the experiments are the host rock analogue (dry-quartz sand), the magma chamber analogue (silicone

reservoir, curved or flat) and the rigid walls of the wood tank. Again we used two geometrical settings (axial symmetry and 3-D) in order to detect differences in the results due to the election of the geometrical setting.

The geometrical setting with axial symmetry (Fig. 4.14) corresponds to a rectangle of 50 cm width which height is equivalent to the thickness of the sand-pack **T** in each experiment. One of the laterals corresponds to the symmetry axis and consequently, displacements in the horizontal direction *x* are fixed to zero ($\boldsymbol{u}_x = 0$). Also here the geometry implies that the computational domain corresponds to the sand of the analogue experiments. The rigid walls of the tank are reproduced fixing the other lateral and the base of the rectangle. Again small black crosses indicate the boundary condition of fixed zero displacement in any direction ($\boldsymbol{u}_x = \boldsymbol{u}_y = 0$). In order to reproduce the flat silicone reservoirs, we select a small part of the rectangle base close to the symmetry axis and free it from the condition of fixed zero displacement, i.e. this small section is able to deform. Curved silicone reservoirs are simulated cutting with a curvy shape the edge of the rectangle base located closer to the symmetry axis. This curved part is also free from the condition of fixed zero displacement, i.e. is able to deform. The upper part of the rectangle is always considered to be traction free.

The 3-D geometrical setting (Fig. 4.14) consists of a prism with fixed laterals and base. The silicone reservoir corresponds to a small free surface cut in the centre of the fixed base (flat silicone reservoir) or to a hemisphere. The upper surface is free.

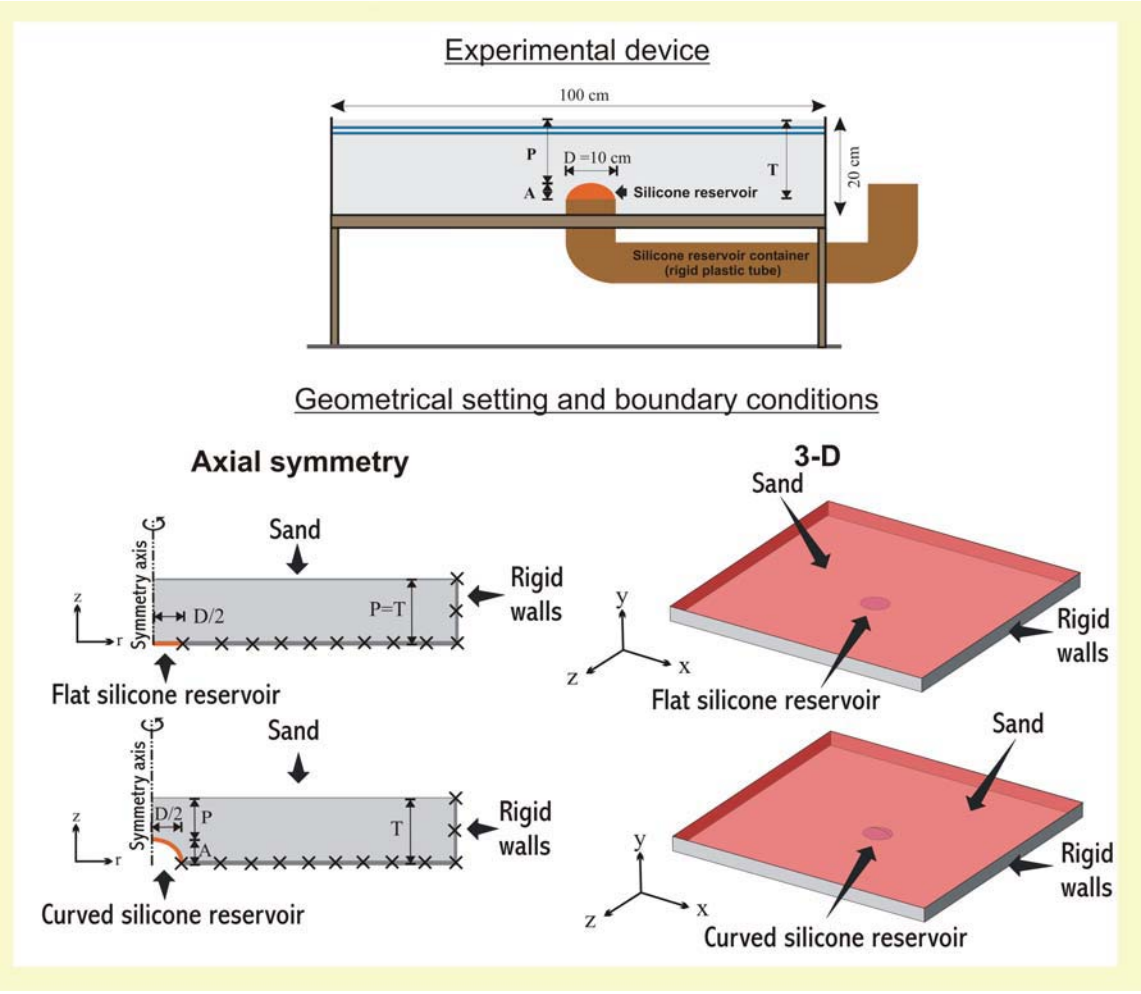

Fig. 4.14: (Top) Sketch of the experimental device reproduced numerically **(Bottom)** Geometrical setting and boundary conditions of the performed mathematical models. The geometrical setting with axial symmetry corresponds to a rectangle (coloured in grey) whit one of the laterals corresponding to the symmetry axis and consequently, with displacements in the horizontal direction *x* fixed to zero ($u_x = 0$). The other lateral and the base of this rectangle are fixed to zero displacement in any direction ($u_x = u_y = 0$). In orange colour are indicated those parts of the base free of the prior boundary condition and representing the silicone reservoir. The upper part of the rectangle is free. The 3-D geometrical setting consists of a prism with fixed laterals and base (grey). The silicone reservoir corresponds to a small free surface cut in the centre of the fixed base (flat silicone reservoir) or to a hemisphere (curved silicone reservoir). The upper surface (red) is free. **A** Height of the silicone reservoir; **D** Silicone reservoir diameter; **P** Silicone reservoir depth; **T** Sand-pack thickness.

IV.5.3.4 Boundary conditions and numerical method

Solutions are obtained using FEMFES, a code that solves elasticity using a Finite Element Method with nodal implementation. The programme, developed in the context of computational fluid dynamics (Codina and Folch, 2004), has been now particularised to elasticity and tested against standard benchmark problems (Folch and Martí, 2004).

The solutions for the several configurations have been calculated using the following values of Young's modulus E = 1400 kPa , Poisson's ratio $\nu = 0.25$ and density ρ_s = 1270 kg/m^3 for the dry-quartz sand. The density value has been obtained in the laboratory and the other two are approximate obtained come from specialized weppages (e.g. http://geology.bgsu.edu). However, we have checked that variations in E (even changes of one order of magnitude) and ν affect only the quantitative analysis of the results but not the qualitative one. Although the values of the principal stresses may vary, the location of the peaks of σ_3 remains constant. Additionally, since we do not know the values of $\mathbf{T_0}$ and $\mathbf{S_0}$ for the dry-quartz sand, it is unnecessary to calculate exactly the values of the principal stresses. Anyway, we are unable to decide which are the points of rupture for dry-quartz sand.

A difficult task when trying to reproduce numerically analogue models is the definition or assignment of the boundary conditions (BC). Some of the BCs assigned to these mathematical models are partially illustrated in Figures 4.13 and 4.14. Since the tank walls are rigid and fixed, displacements have to be prescribed to zero at the computational margins placed at vertical and horizontal distances corresponding to the dimensions of the tank where the experiments where carried out. Normally, in order to minimize edge effects, the computational margins in mathematical models are placed at distances greater than the dimensions of the chamber. However, we want to reproduce exactly the dimensions of the glass or wood tank. We assume that these may introduce border effect in the analogue models and this is a way to check them.

More difficult is to define the BCs that reproduce the balloon deflation or the silicone reservoir withdrawal (i.e. analogue magma chamber withdrawal responsible for the roof collapse). In previous mathematical models focused on natural caldera collapse processes, magma chamber withdrawal is usually simulated imposing an underpressure -ΔP at the chamber walls (e.g. Folch and Martí, 2004). This condition is also feasible to reproduce the balloon deflation when water is evacuated. As mentioned before (see section III.2.3) filled to its maximum capacity the balloon deflates elastically (see Fig. 3.11 A) and at lower water capacities, the roof subsided vertically as the water was evacuated (see Fig. 3.11 B). Consequently, we can choose between simulating the deflation throughout a radial contraction imposing an underpressure **-ΔP** at the walls of the analogue magma chamber (Fig. 4.15 A) or throughout a vertical deformation imposing a vertical traction **VT** at the chamber roof (Fig. 4.15 B). In order to maintain a

certain similarity between balloon analogue models and models simulating natural caldera collapse processes, we simulate the balloon withdrawal imposing underpressure.

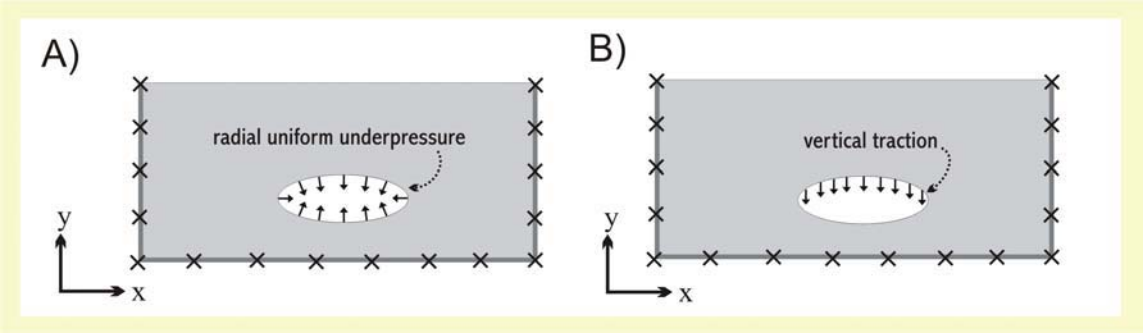

Fig. 4.15: Sketches of the two possible boundary conditions we can assign to our models in order to simulate the experiments with a water-filled balloon as magma chamber analogue. **(A)** The limits of the computational domain are fixed ($u_x = u_y = 0$) and we impose underpressure $-\Delta P$ at the magma chamber walls. **(B)** The limits of the computational domain are fixed ($u_x = u_y = 0$) and we impose a traction the *y* – direction.

However, in order to exemplify which effects may have these two boundary conditions on the results we have run model considering both possibilities (Fig. 4.16). The geometrical setting is identical in both models and corresponds to the geometry of the experiment D-1 in 2-D. The value of the imposed underpressure is equal to the vertical traction $-\Delta P = VT = 10^3$ Pa. Results obtained for the distribution of σ_3 at surface are illustrated on Figure 4.16. We can observe that results obtained are practically identical. The most relevant information for collapse caldera mechanism, the distance at which the peaks of σ_3 appear **h** (Folch and Martí, 2004) is approximately the same at both models. Only the values of σ_3 vary being more tensile with the condition of vertical traction. The election between both boundary conditions introduces small variations in the σ_3 values, which are not so relevant when simulating analogue models because as we mentioned before the values of the mechanical properties (E and ν), which principally control the values of the displacements and stresses, are approximated. In these models it has sense only the quantitative analysis of the results but not the qualitative one.

In this case of the experiments with the silicone reservoir, the collapse takes place due to the flow of the silicone through the reservoir's tube. There does not exist a radial contraction. By contrast, the silicone moves apparently vertically with higher velocity at the centre. Velocity decreases close to the tube walls, due to the existence of frictional forces (Fig. 4.19 A).

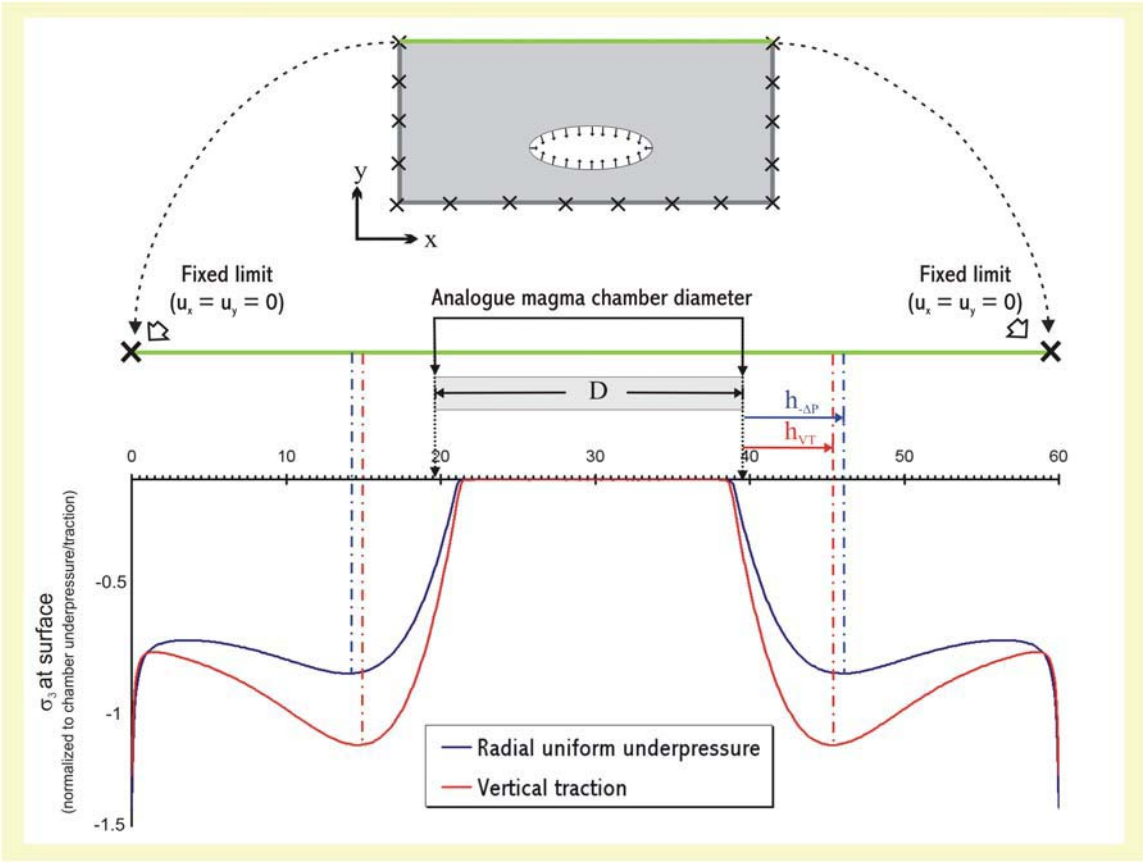

Fig. 4.16: Results obtained when running two models in 2-D with identical geometrical setting but one with assigned radial underpressure **-ΔP** and the other with vertical traction **VT** both focused to simulate analogue magma chamber deflation. The geometrical setting corresponds to the geometry of the experiment D-1 in 2-D. At the bottom the distribution of σ_3 at surface plotted versus distance (in cm) along the tank. **D** Magma chamber diameter; **h** Distance from the vertical projection of the chamber to the peak of σ_3 at surface.

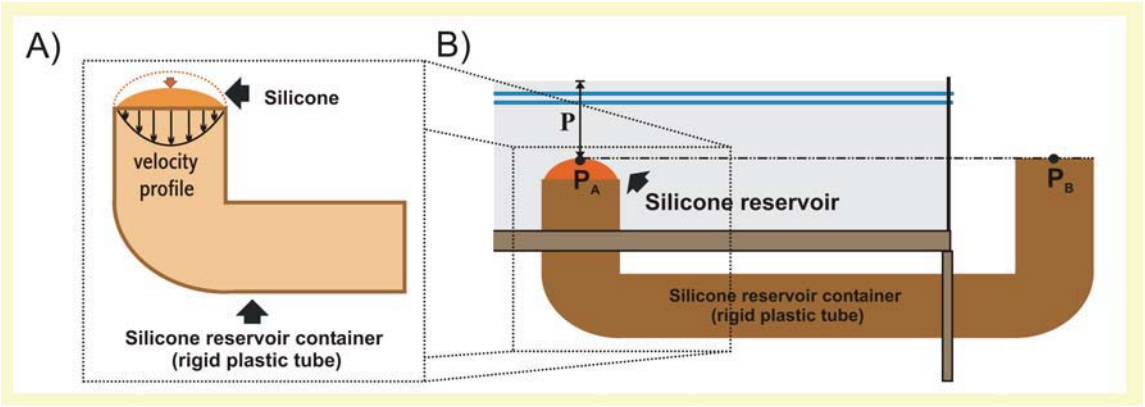

Fig. 4.17: (A) Sketch of the flow of the silicone through the reservoir's tube. The silicone moves vertically with higher velocity at the centre and lower close to the tube walls due to the existence of friction forces. **(B)** Sketch of a section of the silicone reservoir analogue experiments. The excess of weight of the overlying sand-pack produces the silicone outflow. At the beginning of the experiment, prior to the burial of the silicone reservoir by the sand, the pressure at the points $\mathbf{P_A}$ and $\mathbf{P_B}$ are equal to atmospheric pressure. Once the sand has been introduced in the tank the pressure at the point $\mathbf{P_A}$ increases due to the weight of the overlaying sand-pack.

Consequently, a radial underpressure is not representative of this behaviour. Since in the analogue models, the excess of weight of the overlying sand-pack produces the silicone outflow, we have decided that the best approximation is to leave the sand-pack deform by gravity (Fig. 4.17 B). At the beginning of the experiment, prior to the burial of the silicone reservoir by the sand, the pressure at the points $\mathbf{P_A}$ and $\mathbf{P_B}$ are equal to atmospheric pressure. Once the sand has been introduced in the tank the pressure at the point $\mathbf{P_A}$ increases due to the weight of the overlaying sand-pack. The total increase of pressure $+\Delta\mathbf{P}$ is calculated by:

$$+\Delta P = P \cdot g \cdot \rho_s \qquad [4.16]$$

where **P** is the depth of the silicone reservoir (i.e. the thickness of the sand-pack above the point P_A), ***g*** is the gravitational acceleration and $\boldsymbol{\rho_s}$ the density of sand. Consequently, the silicone is obliged to deform under the Earth's gravitational force.

IV.5.3.5 Results

IV.5.3.5.1 Balloon models

In this section we describe and compare the results obtained when reproducing experiments D-1, D-4 and D-5 in a 2-D and a 3-D geometrical setting. According to the conditions of ring fault formation (see section IV.3 for more details), to study numerically analogue caldera collapses we have to localize the maximum value of σ_1-σ_3, the minimum value of σ_3 and the location of the peak of maximum tension (minimum σ_3) at surface.

Results for the experiments D-1, D-4 and D-5 in a 3-D geometrical setting:

- **Regardless the roof aspect ratio of the models, the maximum value of σ_1-σ_3 occurs at the outer margins of the magma chamber (Fig. 4.18 indication I).**

- **The minimum value of σ_3, the tensile stress, (maximum tension) occurs in all three cases at the outer margins of the magma chamber (Fig. 4.18 indication II).**

- All three reproduced experiments have local minimums of σ_3 at surface (Fig. 4.19), i.e. points of maximum of tension, located symmetrically to the magma chamber. The location of these peaks of σ_3 corresponds approximately to the observed limits of non-deformed area in the analogue experiments. Consequently, the distance between the peaks of maximum tensile stress **MTSdis** is similar to the diameter of the non-deformed area **N-D_{max}** (MTSdis $\approx$ N-D_{max}).

- In all three experiments the distance between the peaks of maximum tensile stress **MTSdis** is smaller than the vertical projection of the magma chamber at surface, i.e. is smaller than the maximum diameter of the magma chamber **D_{max}** (MTSdis < D_{max}).

- With decreasing roof aspect ratio **R** of the experiment, the peaks of σ_3 at surface become more tensile (i.e. σ_3 decreases).

Comparison of the results for the experiments D-1, D-4 and D-5 in a 2-D and a 3-D geometrical setting:

- Regardless the used geometrical setting, the maximum value of σ_1-σ_3 occurs at the outer margins of the magma chamber, but above the analogue magma chamber the distribution of σ_1-σ_3 varies considerably (Fig. 4.18 indication III).

- Regardless the used geometrical setting, the minimum value of σ_3 occurs at the margins of the magma chamber. However, the 2-D solution localizes it at the centre of the chamber and the 3-D at the outer margins. Additionally, above the analogue magma chamber the distribution of σ_3 varies considerably (Fig. 4.18 indication IV).

- Independent on the experiment, the values of σ_3 at surface calculated with the 2-D geometrical setting are considerably lower (more tensile) than those obtained with the 3-D approach (Fig. 4.20).

For each experiment the distance between the peaks of minimum σ_3 (i.e. maximum tensile stress) calculated with the 2-D geometrical setting **$MTSdis_{2\text{-}D}$** is considerably larger than that obtained with the 3-D approach **$MTSdis_{3\text{-}D}$** ($MTSdis_{2\text{-}D} > MTSdis_{3\text{-}D}$) (Fig. 4.20).

- With the 3-D geometrical setting, the distribution of the σ_3 values at surface has independent on the experiment a local maximum just in the centre of the analogue magma chamber horizontal extension (Fig. 4.20 indication I). However, with the 2-D approach this local maximum becomes a wide flat region (Fig. 4.20 indication II).

- At the computational margins the results obtained with the 3-D geometrical setting do not present extreme values due to possible edge effects (Fig. 4.20 indication III). By contrast, the distributions calculated with the 2-D approach present extremely low σ_3 values (Fig. 4.20 indication IV).

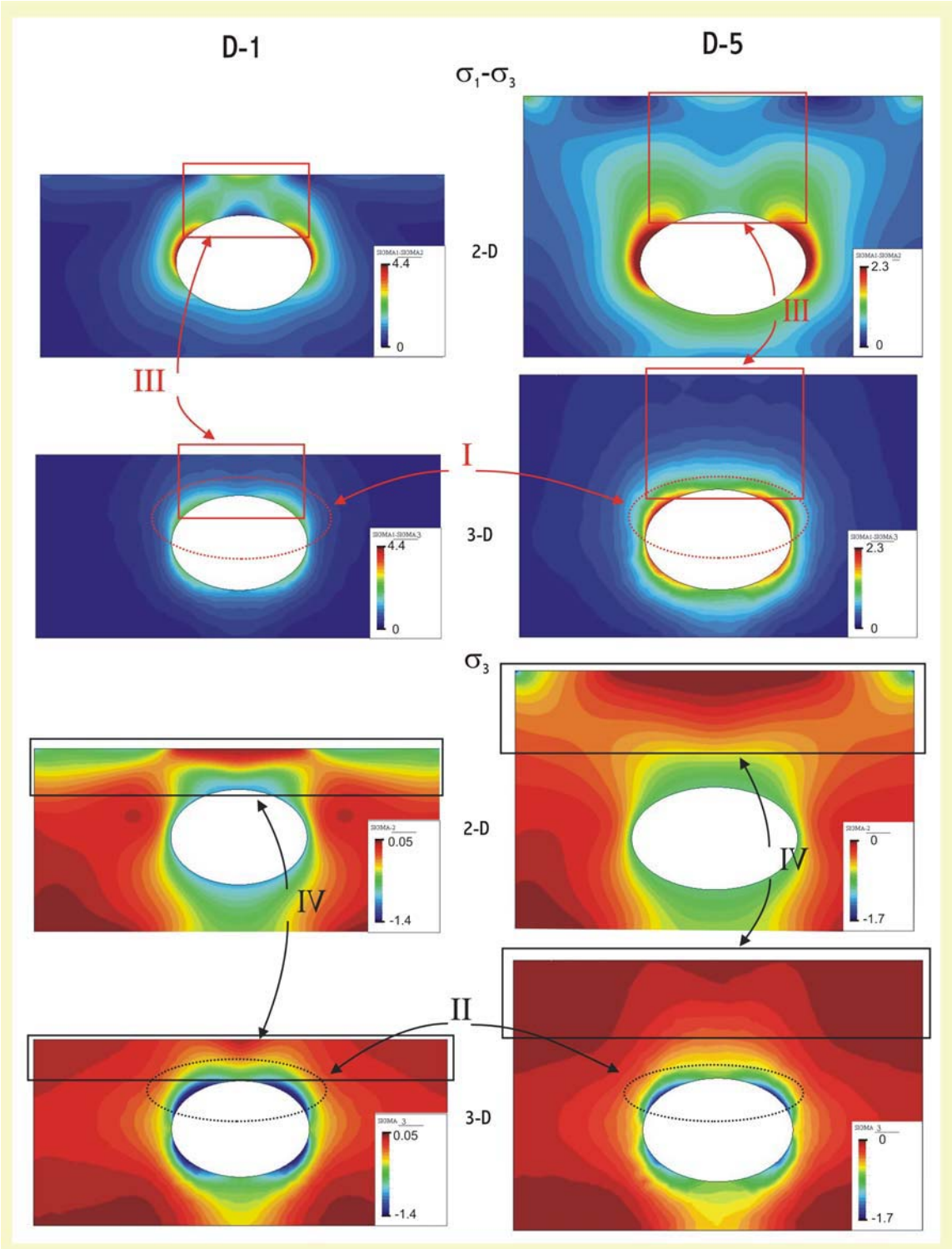

Fig. 4.18: Results obtained when reproducing numerically the analogue experiments D-1 and D-5 in a 2-D and a 3-D geometrical setting. Contour fills of the σ_1 -σ_3 and σ_3. Stress values are normalized to magma chamber underpressure. Negative values for σ_3 imply extension.

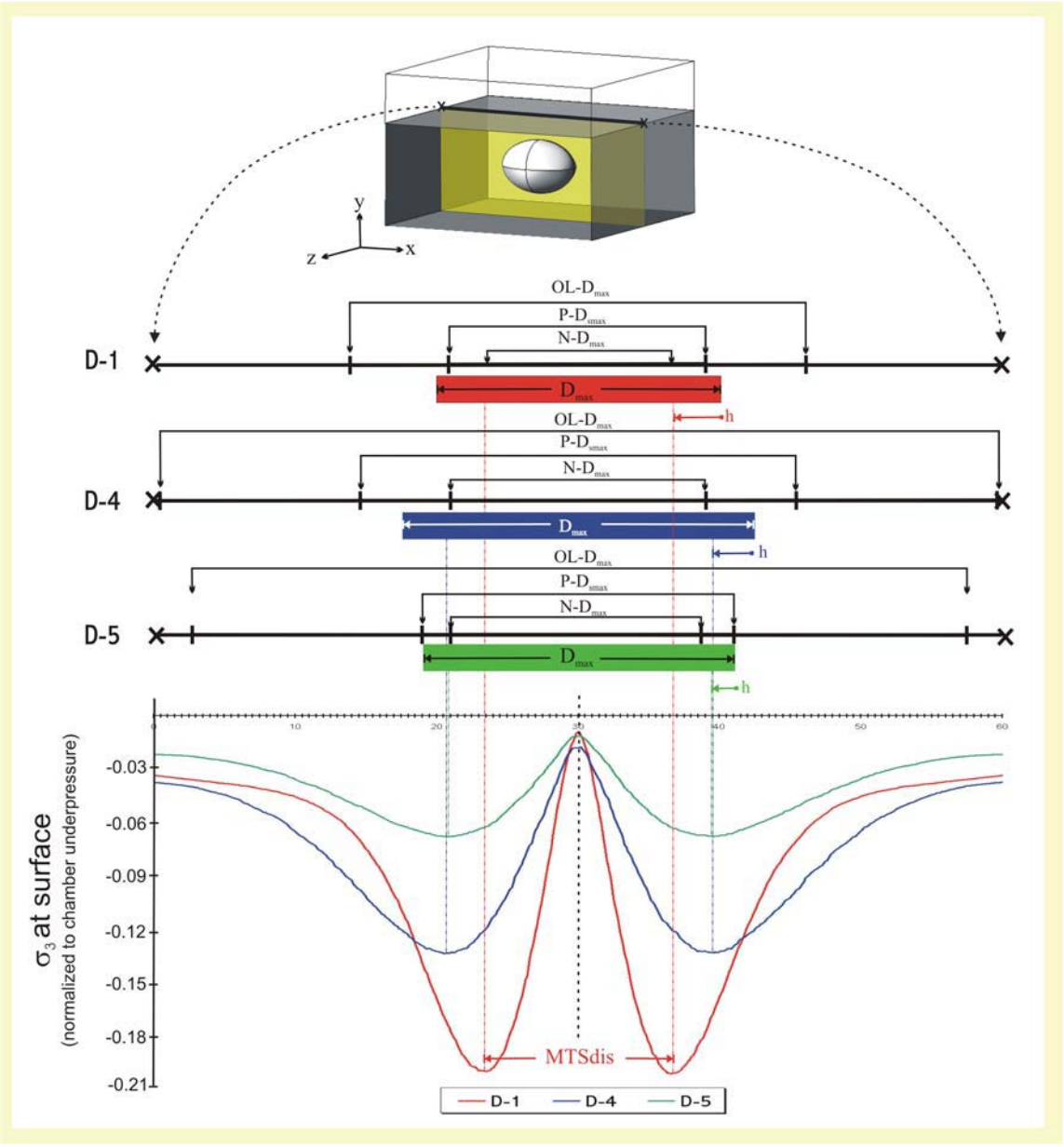

Fig. 4.19: Results obtained when reproducing numerically the analogue experiments D-1, D-4 and D-5 with a 3-D geometrical setting. On the top of the Figure horizontal coloured rectangles indicate the magma chamber analogue horizontal extension in each of the reproduced experiments. Small black crosses indicate the limit of the computational domain with assigned fixed zero displacement ($\boldsymbol{u_x} = \boldsymbol{u_y} = \boldsymbol{u_z} = 0$). At the bottom, distribution of σ_3 at surface plotted versus distance (in cm) along the tank. **D** Magma chamber diameter; **h** Distance from the vertical projection of the chamber to the peak of σ_3 at surface; **MTSdis** Distance between both symmetrical peaks of σ_3 at surface; **OL-D$_{max}$** Maximum diameter of the outer limit of the collapse**; P-D$_{max}$** Maximum piston diameter at surface

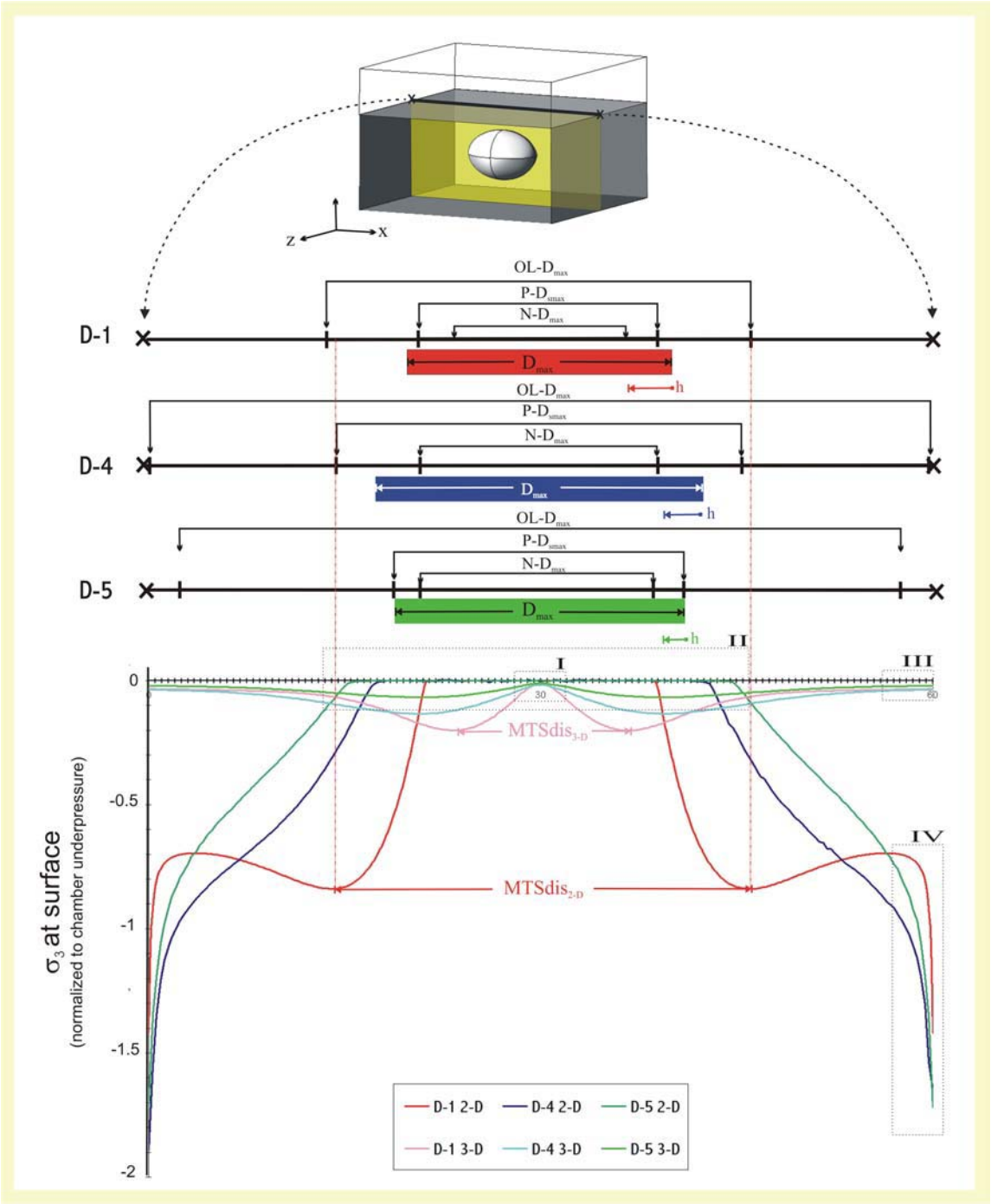

Fig. 4.20: Results obtained when reproducing numerically the analogue experiments D-1, D-4 and D-5 in a 2-D and a 3-D geometrical setting. On the top of the Figure horizontal coloured rectangles indicate the magma chamber analogue horizontal extension in each of the reproduced experiments. Small black crosses indicate the limit of the computational domain with assigned fixed zero displacement ($\boldsymbol{u_x} = \boldsymbol{u_y} = \boldsymbol{u_z} = 0$). At the bottom, distribution of σ_3 at surface plotted versus distance (in cm) along the tank. **D** Magma chamber diameter; **h** Distance from the vertical projection of the chamber to the peak of σ_3 at surface; **MTSdis** Distance between both symmetrical peaks of σ_3 at surface; **OL-D$_{max}$** Maximum diameter of the outer limit of the collapse**; P-D$_{max}$** Maximum piston diameter at surface

IV.5.3.5.2 Silicone models

In this section awe describe the results obtained for the numerical reproduction of the silicone experiments SIL-1, SIL-2, SIL-3 and SIL-7 using an axial symmetric (AS) and a 3-D geometrical setting. Furthermore, we want to study the influence of the silicone reservoir eccentricity ***e*** analysing the results of the silicone models SIL-9, SIL-10, SIL-11 and SIL-12.

Due to the design of the geometrical setting the limit of the magma chamber analogue tends to arrest the highest values of σ_1-σ_3 and σ_3 (Fig. 4.21). Consequently, it is very difficult to discriminate between "real" values and edge effects. Moreover, due to this effect the condition that the maximum value of σ_1-σ_3 should be localized at the outer limit of the analogue magma chamber is in all cases accomplished (Fig. 4.21). In the case of the distribution of σ_3, Figure 4.21 illustrates how important is to redefine the limits of the contour fills to a better visualization of the extensive (negative) values of σ_3. In all experiments, the most tensile stress values are located at the margin of the chamber analogue. Taking into account these observations and the results obtained for the balloon models, we analyse for the silicone models only the distribution of σ_3 at surface.

Results for the experiments SIL-1, SIL-2, SIL-3 and SIL-7 in a 3-D geometrical setting:

- **Independent on the roof aspect ratio value, reproduced experiments have two local minimums of σ_3 at surface (Fig. 4.22). The location of these peaks of σ_3 depends on the roof aspect ratio, the distance between them MTSdis increases with R.**

- **For low roof aspect ratio values (R=0.2-0.3), MTSdis is equivalent to the piston diameter at surface P-D, i.e. in the case of silicone models also to the analogue magma chamber horizontal extension D (see section….. for more details).**

- **For higher R values MTSdis is larger than the vertical projection of the magma chamber at surface D (MTSdis = D + h).**

➢ With increasing roof aspect ratio **R** of the experiment, the peaks of σ_3 at surface become less tensile (i.e. σ_3 increases).

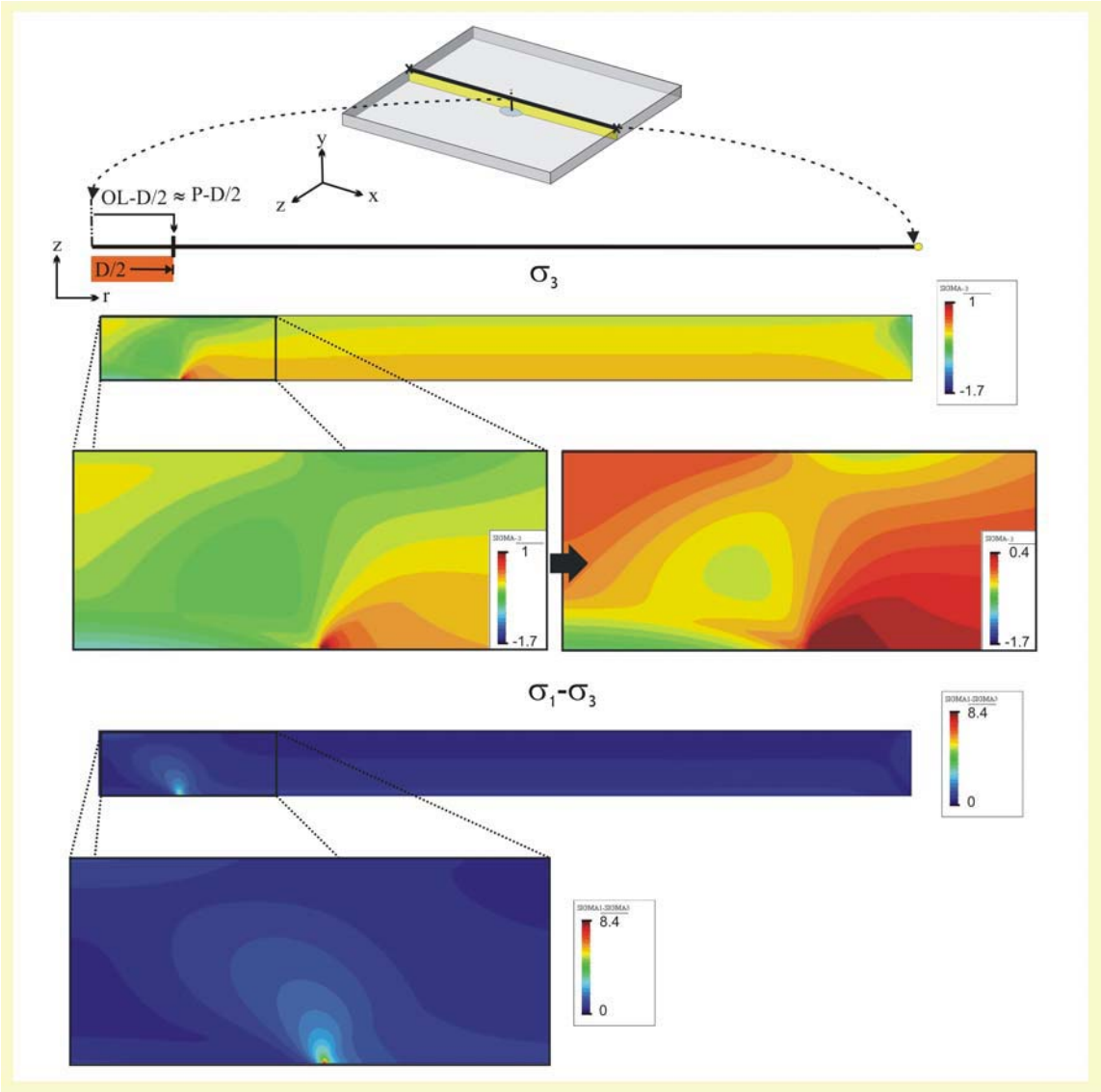

Fig. 4.21: Results obtained when reproducing numerically the analogue experiment SIL-3 in the axial symmetric geometrical setting. On the top of the Figure a sketch illustrates the geometrical setting of the reproduced models. Small black crosses at the laterals indicate the limit of the computational domain, i.e. the walls of the experimental tank. These limits have assigned zero displacement in any spatial directions ($u_x = u_y = u_z = 0$). Moreover, the horizontal the coloured rectangle indicates the magma chamber analogue horizontal extension for all reproduced experiments. The Figure includes the contour fills of σ_1 -σ_3 and σ_3 Stress values are normalized to the pressure increase due to the sand-pack weight. Negative values for σ_3 imply extension. **D** Magma chamber diameter; **h** Distance from the vertical projection of the chamber to the peak of σ_3 at surface; **OL-D** Diameter of the outer limit of the collapse; **P-D** Piston diameter at surface.

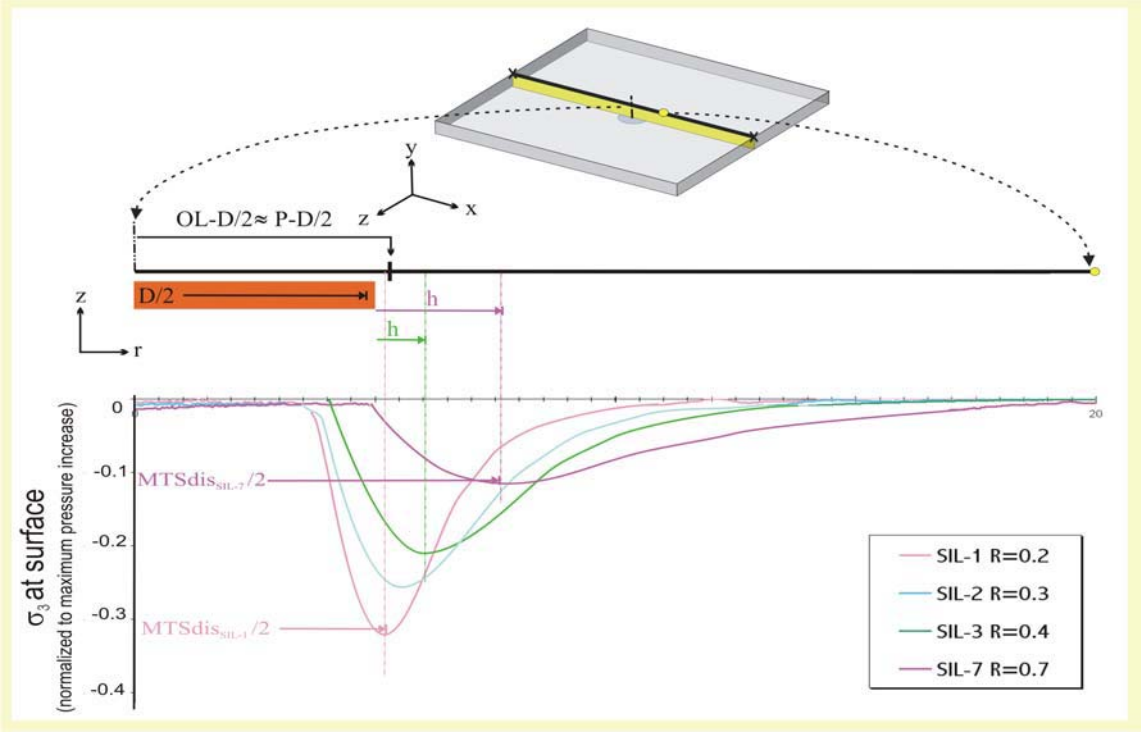

Fig. 4.22: Results obtained when reproducing numerically the analogue experiments SIL-1, SIL-2, SIL-3 and SIL-7 in a 3-D geometrical setting. On the top of the Figure a sketch illustrates the geometrical setting of the reproduced models. Small black crosses at the laterals indicate the limit of the computational domain, i.e. the walls of the experimental tank. These limits have assigned zero displacement in any spatial directions ($u_x = u_y = u_z = 0$). Moreover, the horizontal the coloured rectangle indicates the magma chamber analogue horizontal extension for all reproduced experiments. The Figure includes also the distribution of σ_3 at surface versus distance (in cm) along the tank. Values of σ_3 are normalized to the maximum pressure increase due to the sand-pack weight. **D** Magma chamber diameter; **h** Distance from the vertical projection of the chamber to the peak of σ_3 at surface; **MTSdis** Distance between both symmetrical peaks of σ_3 at surface; **OL-D** Diameter of the outer limit of the collapse; **P-D** Piston diameter at surface

Comparison of the results for the experiments SIL-1, SIL-2, SIL-3 and SIL-7 in an AS and a 3-D geometrical setting :

- For any roof aspect ratio **R** the location of the peaks of σ_3 at surface is independent of the geometrical setting we consider, AS or 3-D (Fig. 4.23 indication I).

- For low roof aspect ratios the peaks of σ_3 at surface are more tensile (i.e. σ_3 decreases) if we obtain the results with the axial symmetric geometrical setting (Fig. 4.23 indication I). Furthermore, the difference between the σ_3 value obtained with the axial symmetric and that obtained with the 3-D models decrease when **R** increases (Fig. 4.23 compare indication I and II). At higher **R** values both curves are practically the same (Fig. 4.23 indication III).

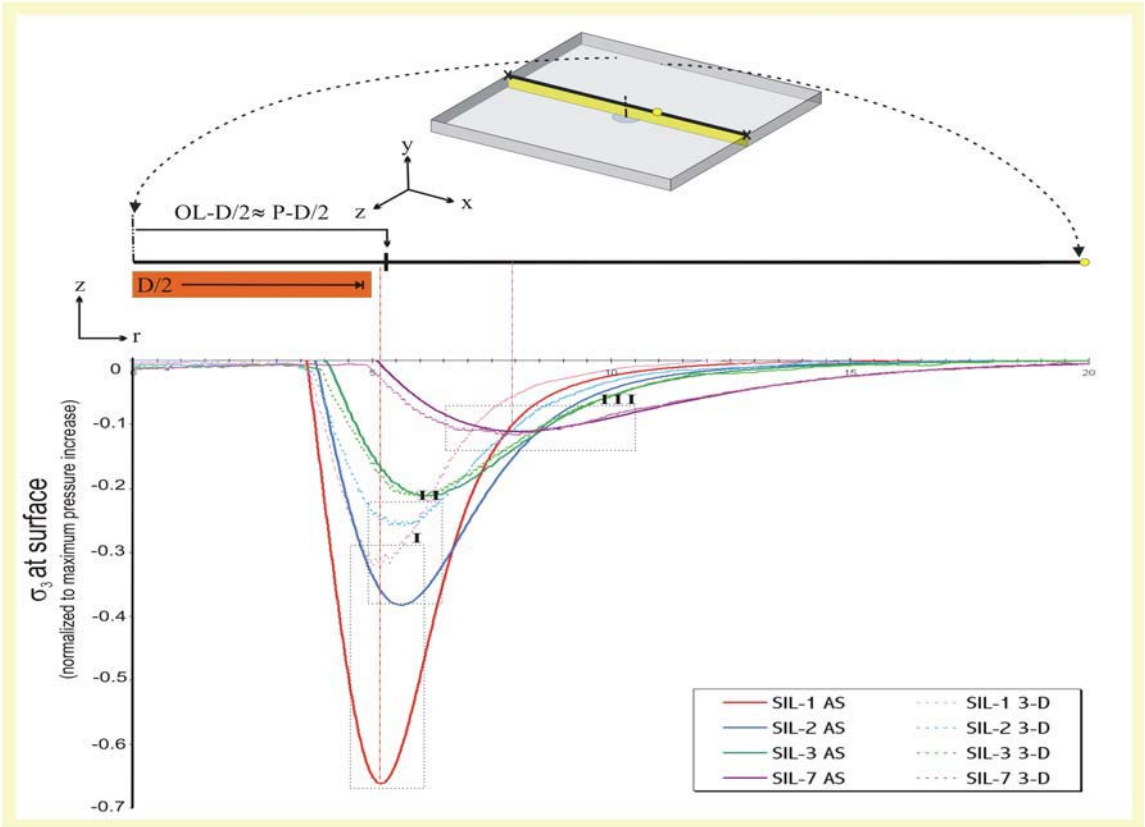

Fig. 4.23: Comparison of the results obtained when reproducing numerically the analogue experiments SIL-1, SIL-2, SIL-3 and SIL-7 using an axial symmetric (AS) and a 3-D geometrical setting. On the top of the Figure a sketch illustrates the geometrical setting of the reproduced models. Small black crosses at the laterals indicate the limit of the computational domain, i.e. the walls of the experimental tank. These limits have assigned zero displacement in any spatial directions ($\boldsymbol{u_x} = \boldsymbol{u_y} = \boldsymbol{u_z} = 0$). Moreover, the horizontal the coloured rectangle indicates the magma chamber analogue horizontal extension for all reproduced experiments. The Figure includes also the distribution of σ_3 at surface versus distance (in cm) along the tank. Values of σ_3 are normalized to the maximum pressure increase due to the sand-pack weight. **D** Magma chamber diameter; **h** Distance from the vertical projection of the chamber to the peak of σ_3 at surface; **MTSdis** Distance between both symmetrical peaks of σ_3 at surface; **OL-D** Diameter of the outer limit of the collapse; **P-D** Piston diameter at surface.

Results for the experiments SIL-9, SIL-10, SIL-11 and SIL-12 in an AS geometrical setting:

- Independent on the silicone reservoir eccentricity e, reproduced experiments have two local minimums of σ_3 at surface (Fig. 4.24). Apparently, the location of these peaks of σ_3 depends on e the roof aspect ratio, i.e. **MTSdis** increases with e.

- With increasing e of the silicone reservoir (i.e. the reservoir becomes flatter), the peaks of σ_3 at surface become more tensile (i.e. σ_3 increases) (Fig. 4.24 indication I).

➢ **Varying *e* two experiments with different roof aspect ratio R may have similar values for the σ_3 peak at surface (Fig. 4.24 indication II).**

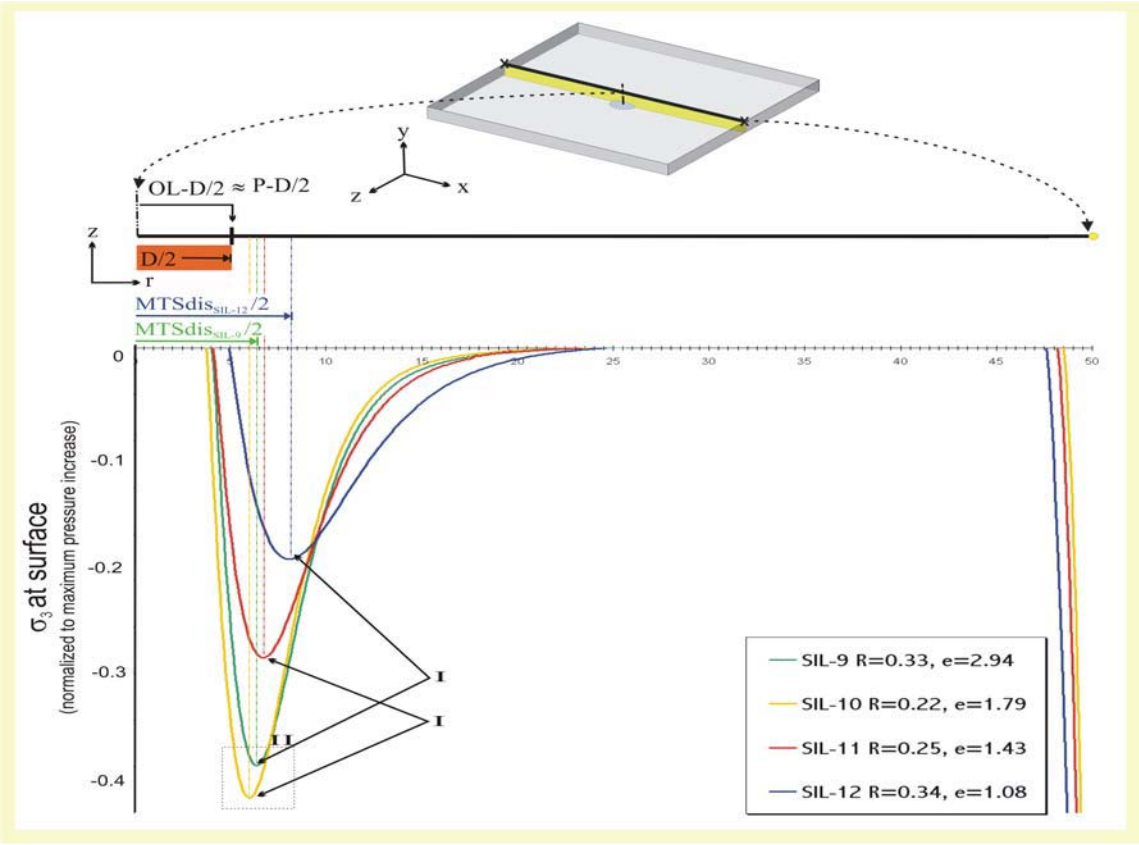

Fig. 4.24: Results obtained when reproducing numerically the analogue experiments SIL-9, SIL-10, SIL-11 and SIL-12 with an axial symmetrical geometrical setting. On the top of the Figure a sketch illustrates the geometrical setting of the reproduced models. Small black crosses at the laterals indicate the limit of the computational domain, i.e. the walls of the experimental tank. These limits have assigned zero displacement in any spatial directions (u_x = u_y = u_z = 0). Moreover, the horizontal the coloured rectangle indicates the magma chamber analogue horizontal extension for all reproduced experiments. The Figure includes also the distribution of σ_3 at surface versus distance (in cm) along the tank. Values of σ_3 are normalized to the maximum pressure increase due to the sand-pack weight. **D** Magma chamber diameter; **h** Distance from the vertical projection of the chamber to the peak of σ_3 at surface; **MTSdis** Distance between both symmetrical peaks of σ_3 at surface; **OL-D** Diameter of the outer limit of the collapse; **P-D** Piston diameter at surface.

Comparison of the results for the experiments SIL-9 and SIL-11 in an AS and a 3-D geometrical setting:

➢ **Independent of the model and, the distribution of σ_3 at surface has two local minimums (Fig. 4.25). However, the location of these peaks of σ_3 is dependent on the geometrical**

setting. The distance between them **MTSdis** is smaller in the 3-D models than in the axial symmetric models.

- In the case of model SIL-9 (**R**=0.33, e = 2.49) the value of the σ_3 peak is independent of the type of geometrical setting (Fig. 4.25 indication I). By contrast, results obtained for model SIL-11, which has a similar **R** (**R**=0.34) but a lower (e = 1.49) indicate that there exist some differences between the values of the σ_3 peak. The peak of σ_3 at surface calculated with the 3-D geometry is more tensile (i.e. σ_3 smaller) than that obtained with the AS model (Fig. 4.25 indication II).

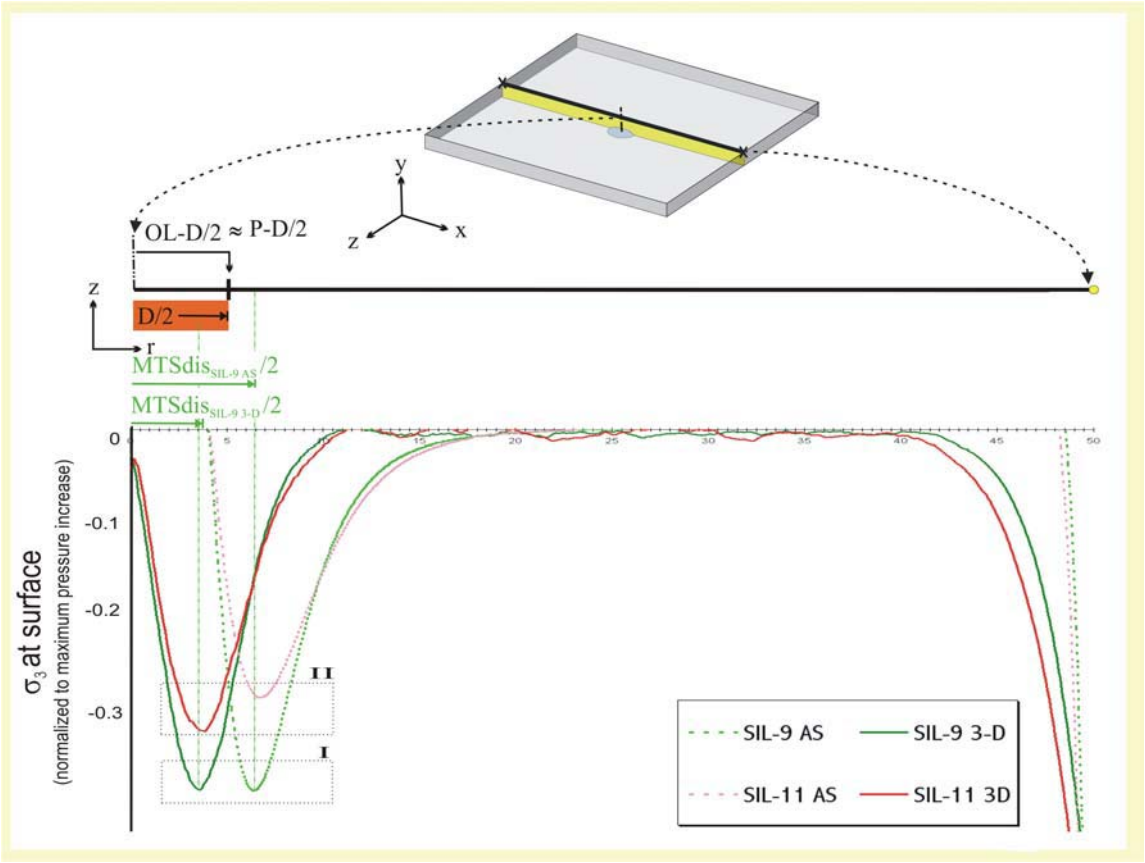

Fig. 4.25: Comparison of the results obtained when reproducing numerically the analogue experiments SIL-1, SIL-2, SIL-3 and SIL-7 using an axial symmetric (AS) and a 3-D geometrical setting. On the top of the Figure a sketch illustrates the geometrical setting of the reproduced models. Small black crosses at the laterals indicate the limit of the computational domain, i.e. the walls of the experimental tank. These limits have assigned zero displacement in any spatial directions (u_x = u_y = u_z = 0). Moreover, the horizontal the coloured rectangle indicates the magma chamber analogue horizontal extension for all reproduced experiments. The Figure includes also the distribution of σ_3 at surface versus distance (in cm) along the tank. **D** Magma chamber diameter; **h** Distance from the vertical projection of the chamber to the peak of σ_3 at surface; **MTSdis** Distance between both symmetrical peaks of σ_3 at surface; **OL-D** Diameter of the outer limit of the collapse**; P-D** Piston diameter at surface.

IV.5.3.6 Discussion

IV.5.3.6.1 Analogue models vs. mathematical models: Similarities and discrepancies

The mathematical reproduction of analogue models allows us to infer the restrictions of both types of modelling. Whereas analogue modelling let us to visualize the process itself, mathematical models are able to quantify it. However, are the results obtained with both types of models comparable? We have seen in section III.2.3 that analogue experiments are constrained by a long series of restrictions directly associated with the applied analogue materials and the design of the experimental device. Moreover, mathematical models have also several restrictions (see section IV.4.3). These come especially from the considered host rock rheology and fault simulation, and the actual impossibility of performing mathematical models coupling fluid dynamics and rock mechanics.

Reproducing numerically some of the balloon and silicone experiments we want to infer how the abovementioned restrictions affect and influence the results obtained with both analogue and mathematical modelling. We begin with the comparison with the results obtained for the analogue and mathematical models D-1, D-4 and D-5. Since we assume that 3-D mathematical models reproducing balloon experiments are more accurate than 2-D ones, we take into account only the results of the three-dimensional calculations. We observe in Figure 4.19 that the peak of σ_3 coincides with the limit of the non-deformed area. Now, we have to interpret the meaning of this coincidence. On the one hand, the peak of maximum tensile stress at surface determines the location of the collapse controlling ring faults (see section IV.3). Also, the limit of non-deformed area in analogue balloon experiments is defined by the arrival of the "bell-shaped faults" at surface (see Fig. 3.17) and not by the vertical subsidence-controlling ring faults. Consequently, the numerical and experimental results obtained are conceptually different. Theoretically, assuming that the peak of σ_3 at surface corresponds to the location of the ring faults, **MTSdis** would approximately correspond to the diameter of the subsiding piston at surface **P-D$_s$**, but this is not the case in the analogue models.

Let us study now the results obtained with the mathematical models simulating the silicone reservoir experiments. In this case the σ_3 peaks do not coincide with any of the structural features of this kind of models. Only the mathematical simulation

reproducing the silicone experiment with the lowest roof aspect ratio (R=0.3) is consistent with real observation, i.e. the σ_3 peak at surface corresponds to the position of the piston limits at surface and at the same time to the limit of the silicone reservoir. Apparently, when reproducing the silicone models of low R, mathematical models provide results more similar to experimental ones.

We have to keep in mind that balloon and silicone analogue models provide slightly different results, specially concerning the width of the extensional area surrounding the collapse area (see section III.3.6.1). For balloon models this area is considerably wider and for silicone experiments almost inexistent (compare Figs. 3.14 and 3.30). Discrepancies between balloon and silicone models appear here again when comparing the numerical results. No apparent concordance exists between the experimental and mathematical approach of balloon models, but there exist some for low R silicone experiments. Why? Which are the factors controlling these discrepancies in the results obtained? After long considerations, we assume that one important factor is to consider elasticity in the numerical approaches. In fact, as we can see in Figure 3.18, the collapse beginning is characterized by a nearly elastic deformation. However, at a certain moment the sand (host rock analogue) faults and fractures propagate down- and upwards. Evidently, mathematical models assuming elasticity can only reproduce the first deformation stage. Once the fist fault has appeared, the assumption of elasticity becomes non-sense and probably also the numerical results. Some authors (e.g. Folch and Martí, 2004) affirm that elastic behaviours to predict brittle rock strain lacks robustness, but it can be useful for general approximations. Nevertheless, they admit possible problems when studying any particular system in detail, which is our case. Although, in some cases, elasticity is enough to estimate the possible location of future fractures, we do not see this correlation when reproducing the balloon experiments. The first fractures that appear in the analogue models are those delimiting the extensional area (see Fig. 3.17). However, according to the peak of σ_3 at surface, we would expect to find the first fractures in a location equivalent to the limit of the non-deformed area. Besides, when reproducing low R silicone experiments the σ_3 peak coincides with the location of the first fractures that appear in the collapse process. Is this a pure coincident result or are some other reasons that may explain this observation? A more accurate and exhaustive analysis is out of the scope of this work, but it can be a possible subject for future works. However, we can sense that possible reasons for a possible reason for this

phenomenon may be implicit in the type of the analogue magma chamber (balloon or silicone reservoir) and possible edge effects induced by the tank size and consequently, introduced in the mathematical model via the small dimensions of the computational domain. Additionally, boundary conditions on the numerical models may be not accurate enough. For example, the assigned underpressure does not satisfactorily represent the natural contraction of the latex balloon due to the withdrawal of water, contrarily to the deformation of the silicone, which seems to be more accurately reproduced. These ideas may be the basis for further studies focused in this topic.

IV.5.3.6.2 Restrictions and implications of the selected geometrical setting

Traditionally, authors tend to use 2-D or axial symmetry to avoid time-consuming calculations. However, we have seen that there exist some differences in the results obtained depending on the selected geometrical setting. Compare for example the results exposed in Figure 4.20. The 2-D approximation does not indicate any σ_3 peak for high roof aspect ratio experiments. Additionally, the σ_3 profile of experiment D-1 shows two σ_3 peaks that have a completely different correspondence with analogue results. Evidently, a bi-dimensional approximation is too simplistic when considering magma chambers with geometries inadaptable to infinite long or wide bodies (Fig. 4.11), which are reproducible assuming a "plane strain" or a "plane stress" 2-D approach, respectively. Consequently, if possible, it is preferable to use a 3-D geometry rather than over-simplify 2-D models, which may lead to misinterpretations of the results.

Something different happens when comparing 3-D and AS results. Remember that 3-D and AS results for simulations considering a flat silicone reservoir are quite similar, whereas for curved silicone reservoir, differences are more evident. Regarding the distribution of σ_3 at surface, results obtained for the flat silicone reservoir experiments using a 3-D or and AS geometry are practically similar. In both sets of results (3-D and AS results) the distribution at surface of σ_3 is characterised by a flat area close to the symmetry axis and a local minimum (σ_3 peak) at a certain radial distance. For the highest roof aspect ratio simulations the values of the σ_3 peak are similar in both results sets. For lower R values, the 3-D simulation provides a less tensile σ_3 peak than the axial symmetric calculation.

art from the distribution of σ_3 at surface we want to compare the total displacement at surface (Fig. 4.24). We can clearly observe that there exist some differences between the 3-D and the AS results, especially close to the symmetry axis. The difference in the value of the maximum displacement is more evident in the model with lower R (SIL-2, R = 0.3). In short, the election of the geometrical setting is not trivial for the results obtained and consequently, for the drawn conclusion and interpretations. We continue this discussion and the implications in the next section.

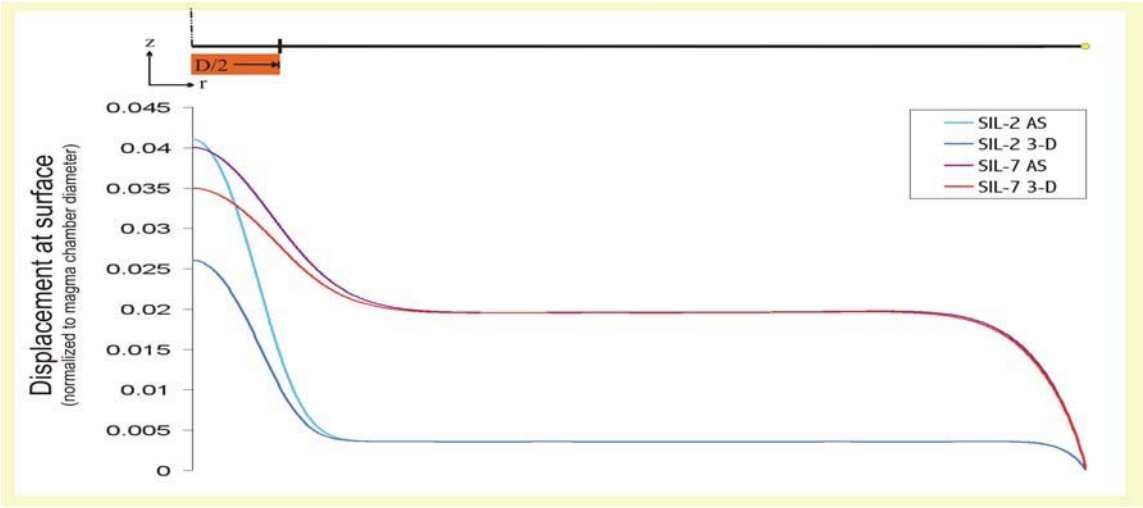

Fig. 4.26: Comparison of the results obtained when reproducing numerically the analogue experiments SIL-2 and SIL-7 using an axial symmetric (AS) and a 3-D geometrical setting. On the top of the Figure a sketch illustrates the geometrical setting of the reproduced models. The horizontal coloured rectangle indicates the magma chamber analogue diameter. The Figure includes also the displacement at surface versus distance along the tank. Values of displacement are normalized to the magma chamber diameter. **D** Magma chamber diameter.

IV.5.4 Geometrical constrains on the formation of ring fault calderas

IV.5.4.1 General aspects and objectives

Some authors (e.g. Gudmundsson, 1998; Folch and Martí, 2004) have investigated which combinations of chamber shape and depth are compatible with the creation of subvertical normal ring-faults that may lead to the formation of plate-subsidence calderas without the existence of previous fracturing or regional tectonic stresses. Although the results obtained were interesting and relevant for the understanding of caldera-forming processes, all these mathematical models were performed in 2-D or considering axial symmetry (Table 4.1). Consequently, some doubts have arisen regarding the reliability and accuracy of these studies. Therefore, the

principal aim of this section is to reproduce in 3-D some of the calculations performed by Folch and Martí (2004) those who considered axial symmetry. We can compare the results obtained in order to study the influence of the selected geometrical setting and to investigate the possible consequences in the interpretation.

IV.5.4.2 Geometrical setting

In Figure 4.27 we show the considered geometrical settings: the AS and the 3-D. As in prior models, we assume that the magma chamber is elliptical in cross section and is characterized by two axis **D** (magma chamber diameter) and **H** (magma chamber height). The magma chamber is located at a depth **P** below the Earth's surface.

In the case of axial symmetry, the computational domain is a rectangle which margins are placed at vertical and radial distances approximately ten times greater than the dimensions of the chamber. One of the margins acts as the symmetry axis. Results obtained with the AS models can be compared with those presented by Folch and Martí (2004).

In the 3-D geometrical setting, the elliptical magma chamber is converted to a lenticular magma chamber, i.e. the orthogonal projection of the chamber at surface is a circle of radius **D**. It is also characterized by the axis **D** and **H**. The computational domain corresponds to a cylinder with diameter and height ten times larger than the dimensions of the chamber. The magma chamber is located in the centre of the cylinder at a depth **P** below the cylinder's top, i.e. Earth's surface.

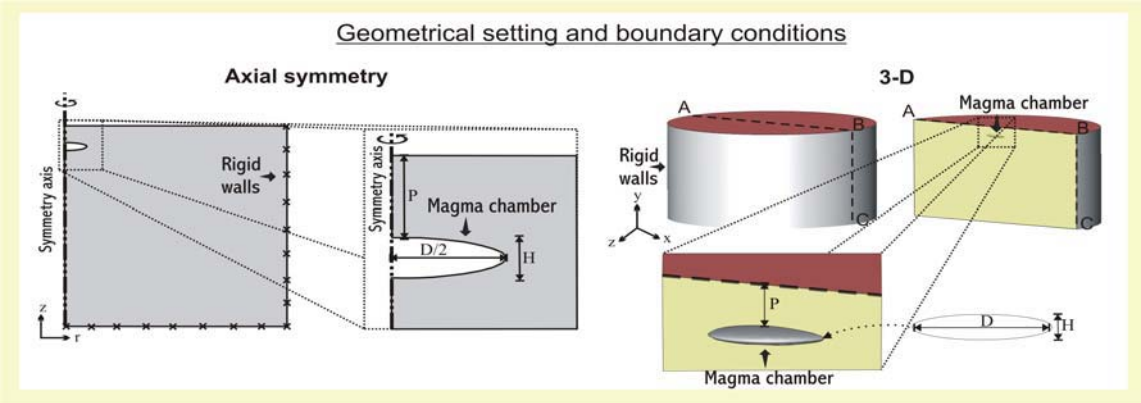

Fig. 4.27: Sketch of the corresponding geometrical setting and boundary conditions of the performed mathematical models. The axial symmetric geometrical setting corresponds to a rectangle with fixed laterals and base (u_x = u_y = 0). The magma camber is reproduced by an elliptical hole (white) in the rectangle. The top of the rectangle is traction free and. The 3-D geometrical setting consists of a cylinder with fixed laterals and base (grey). The magma chamber corresponds to a ellipsoidal lenticular hole. The upper surface of the cylinder corresponds to the Earth's surface and is traction free (red). **D** Magma chamber diameter; **H** Magma chamber height; **P** Balloon depth.

IV.5.4.3 Boundary conditions and numerical method

Similar to the other models, solutions are obtained using FEMFES. For the host rock properties we use standard values of Young's modulus $\boldsymbol{E}$ = 45 GPa and Poisson's coefficient ν= 0.25. Additionally, we assume that the host rock tensile strength $\mathbf{T_0}$ is 15 MPa and the shear strength $\mathbf{S_0}$ is 50 MPa. Nevertheless, possible variations of these values (always within bounds typically found in nature) do not alter the conclusions of this study.

Since we consider linear elasticity to solve the models, we can apply the superposition principle. Consequently, the solution of the problem gives the variations of the stress field (due to chamber decompression) with respect to an initial state of stress. The total stress field will be the pre-eruptive reference stress field plus the computed syn-eruptive stress variations. In our models we assume that the initial stress field is purely lithostatic given by Equation 4.16. Under these hypotheses, the stress field around a magma chamber is computed by solving the AS or the 3-D equations for each specific configuration and set of boundary conditions.

As boundary conditions we impose an underpressure $\mathbf{-\Delta P}$ at the chamber walls in order to simulate magma chamber decompression and we consider the surface of the Earth as free surface (i.e. traction free). Furthermore displacements are prescribed to zero ($\boldsymbol{u_x} = \boldsymbol{u_y} = \boldsymbol{u_z} = 0$) at the computational margins where the variations of the stress field due toe the magma chamber decompression can be neglected.

IV.5.4.4 Performed models

We have performed six different models (Table 4.4): 3 with axial symmetry and 3 in 3-D.

Models	INPUT PARAMETERS					
	P (km)	R	H (km)	D (km)	*e*	-ΔP (MPa)
NR-0.2 AS	2	0.2	2	10	5	15
NR-0.4 AS	4	0.4	2	10	5	15
NR-0.6 AS	6	0.6	2	10	5	15
NR-0.2 3-D	2	0.2	2	10	5	15
NR-0.4 3-D	4	0.4	2	10	5	15
NR-0.6 3-D	6	0.6	2	10	5	15

Table 4.4: List of the performed mathematical models and the corresponding input parameters. All parameters remain constants except of the roof aspect ratio **R**. Axial symmetric models are indicated with the abbreviation "AS". **-ΔP** Magma chamber underpressure; **D** Magma chamber diameter; **H** Magma chamber height; **P** Magma chamber depth; **R** Roof aspect ratio.

IV.5.4.5 Results

Since we want to compare our results with those exposed by Folch and Martí (2004), we are going to illustrate the contour fills of σ_1-σ_3 and σ_3 and the distribution of σ_3 at surface, in order to find the position of the peak of maximum tension. We assume that caldera collapse will take place if all the conditions for ring fault formation mentioned in section IV.3 are accomplished.

In Figure 4.28 we show the contour fills of σ_1-σ_3 and σ_3. Regardless the roof aspect ratio of the mathematical model the maximum value of σ_1-σ_3 occurs at the outer margins of the magma chamber (Fig. 4.28 indication I). Observe that for both samples (NR-0.2 3-D and NR-0.6 3-D) the highest value of σ_1-σ_3 goes beyond 50 MPa, the considered shear strength of the rock S_0. Consequently, if σ_1-σ_3 >S_0 shear fractures can be produced according to condition (2) for ring fault formation. If we compare the results obtained with the two different geometrical settings (axial symmetry or 3-D), notice that around the magma chamber the distribution of the values of σ_1-σ_3 is similar. By contrast, approaching to the surface, discrepancies between the results increase (Fig. 4.28 indication II). Regarding the contour fills of σ_3. For low roof aspect ratio, σ_3 values at surface become more tensile. In fact, only for the sample NR-0.2 3-D (**R**=0.2, 3-D) with the lowest **R** value, the minimum value of σ_3 is lower or close to 15 MPa, the considered tensile strength of the rock T_0. Consequently, only in this case $\sigma_3 < T_0$, i.e. tensile fractures can be produced according to condition (1) for ring fault formation. If we compare the results obtained with the two different geometrical settings (axial symmetry or 3-D), notice that there exist some discrepancies between the results (Fig. 4.28 indication III).

In Figure 4.29 we have represented the distribution of total displacement and of σ_3 at surface. In the case of the displacement distribution at surface, we observe that the maximum is centred in the magma chamber axis. Notice that for the same model in 3-D or with the AS geometry whereas the profile of the curve is geometrically similar the value of maximum displacement $\boldsymbol{u_{max}}$ varies. In all three cases, the AS models provide a much higher value of $\boldsymbol{u_{max}}$ than the 3-D ones. Additionally, we can observe that the difference between the values of $\boldsymbol{u_{max}}$ provide by the AS and the 3-D decrease when increasing R. Regarding the distribution of σ_3 at surface. Again, similar to the mathematical models reproducing curved silicone reservoir experiments, differences

between AS and 3-D are quite notorious. First, the main differences reside in the position of the σ_3 peaks. Results obtained with the 3-D models localize the minimum value of σ_3 at a distance shorter than **D**/2 and this position is independent on the roof aspect ratio value. By contrast, AS models indicate that the peak of σ_3 is situated beyond the limits of the magma chamber and the distance increases when increasing **R**. Additionally, if we compare the values of σ_3 we observe that similar to the displacements, difference increase when decreasing **R**.

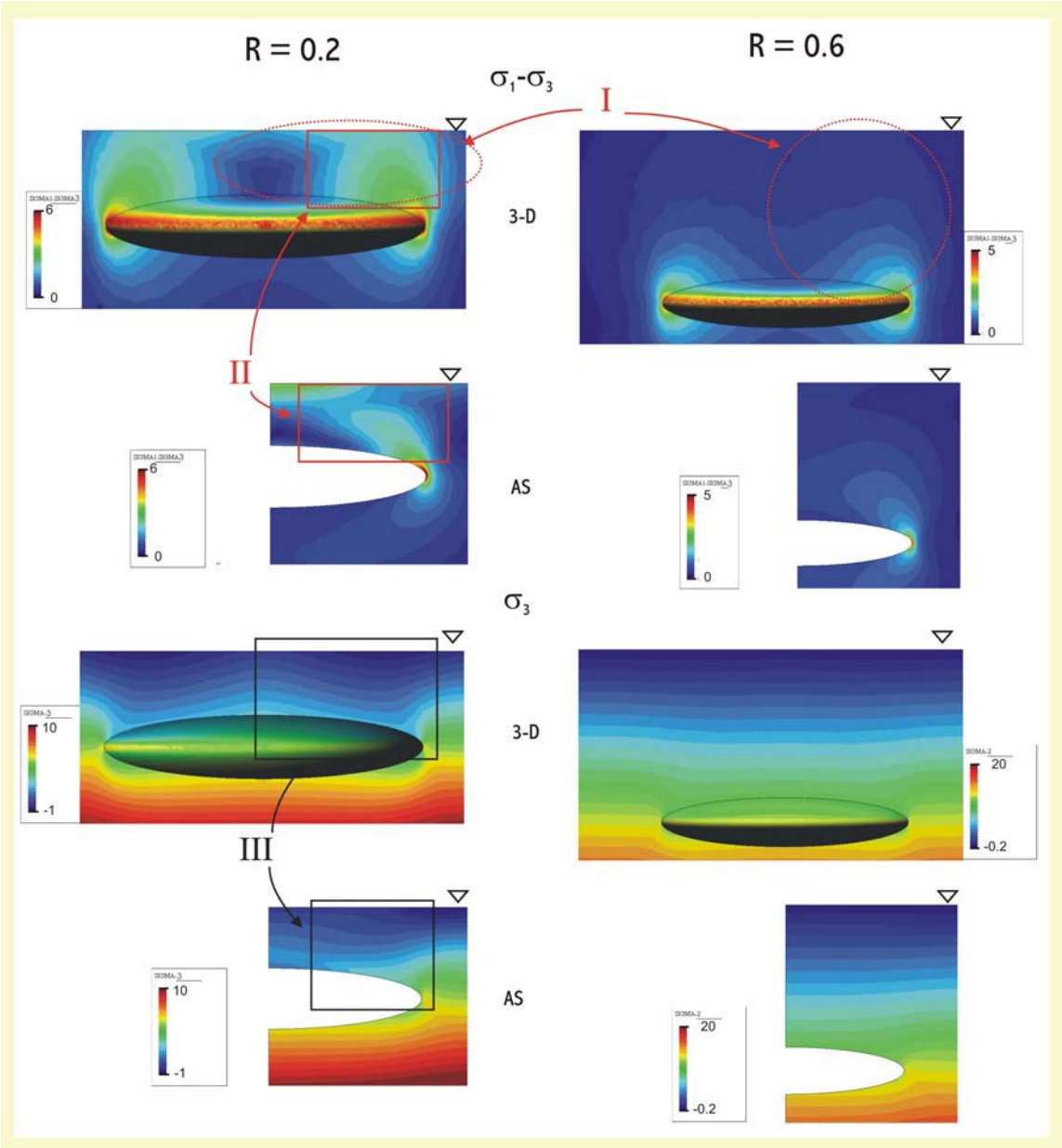

Fig. 4.28: Results obtained for the mathematical models NR-0.2 3-D, NR-0.2 AS, NR-0.6 3-D and NR-0.6 AS. Contour fills of σ_1 -σ_3 and σ_3. Stress values are normalized to magma chamber underpressure. Negative values for σ_3 imply extension.

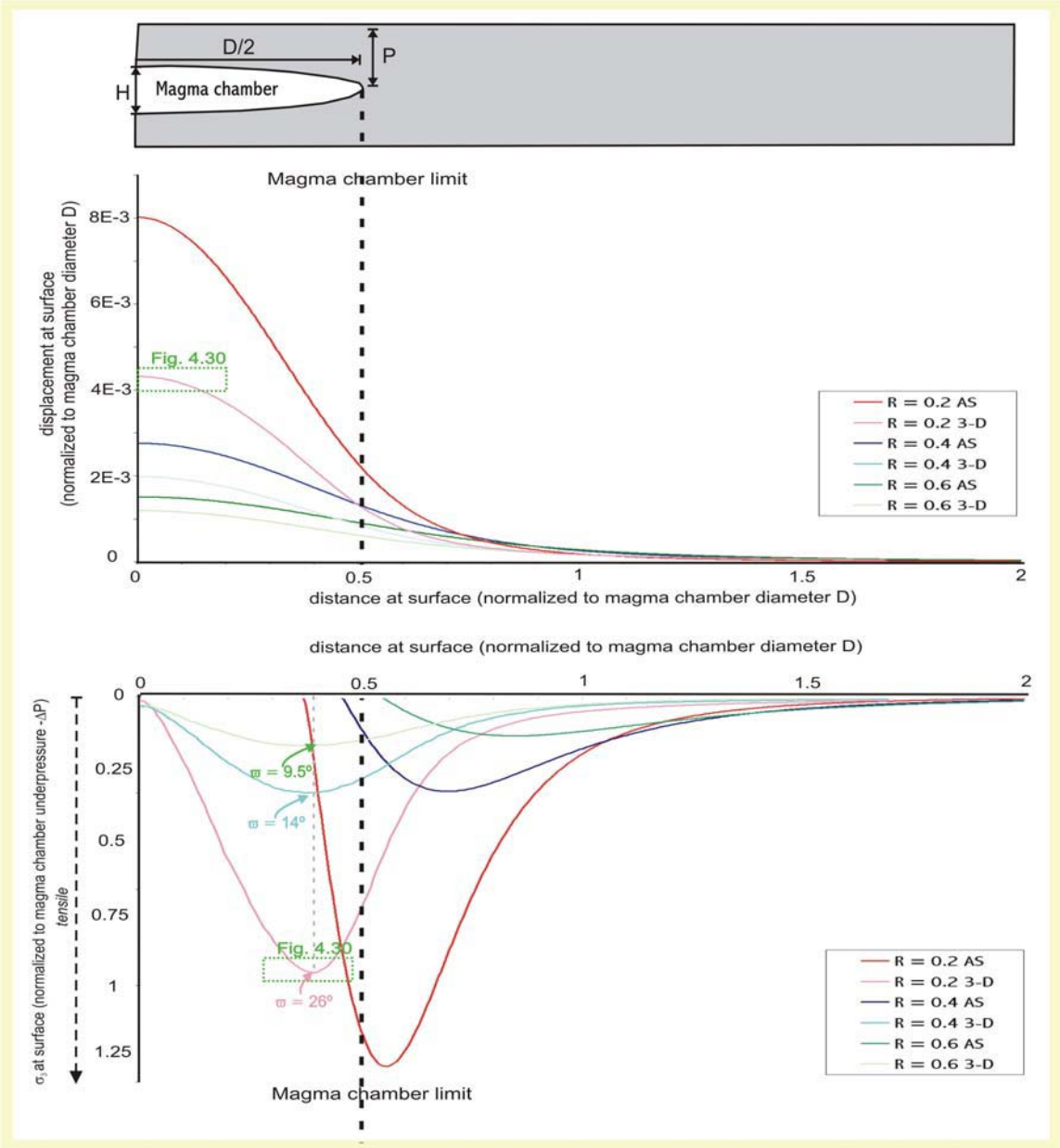

Fig. 4.29: Comparison of the results obtained when using an axial symmetric (AS) or a 3-D geometrical setting. On the top of the Figure a sketch illustrates the location of the magma chamber to facilitate the comprehension of the plots. The Figure includes the distribution of the displacements and of σ_3 at surface versus distance respect the magma chamber axis. Values of displacements and distances are normalized to the magma chamber diameter and those of σ_3 to the magma chamber underpressure **-ΔP.** The angle **ϖ** (Fig. 4.2), localized between the vertical and the line that draw from the edges of the cavity marks the peak of σ_3 at surface and has been calculated according to Equation 4.1. **D** Magma chamber diameter; **H** Magma chamber height; **P** Magma chamber depth; **R** Roof aspect ratio.

IV.5.4.6 Discussion

IV.5.4.6.1 Numerical implications of the selected geometrical setting

Theoretically, at least regarding the displacement and σ_3 values, results obtained should be independent on the selected geometrical setting. Due to the selected 3-D geometry (remember that for the 3-D models we use revolution geometries of the AS models) both AS and 3-D models are numerically equivalent. However, our results indicate the opposite. After long consideration we assume that the mesh of the 3-D models could play an important role.

Figure 4.30 shows the mesh of model NR-0.2 AS (R=0.2 and AS). We can observe that whereas the element size at the computational margins is quite large, around the magma chamber it is relatively uniform and refined. The total number of elements is 12,354, which are associated with 6,526 nodes and the accuracy of the results obtained is satisfactory for our study. In fact, a more refined mesh improves the results in the displacements only in the second decimal position. A finite element mesh of these characteristics (12,354 elements and 6,526 nodes) does not offer any computational problems and the calculation time is fast (< 1 min).

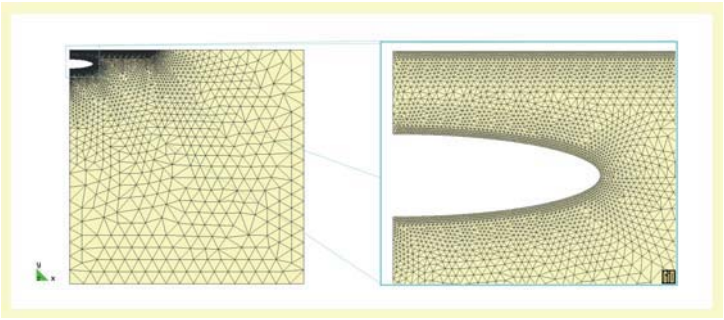

Fig. 4.30: Mesh of model NR-0.2 AS (R=0.2 and axial symmetric).

However, important problems appear when trying to mesh 3-D models. Figure 4.31 illustrates three different meshes for model NR-0.2 3-D (**R**=0.2, 3-D). Mesh A has a very small element size at surface, the magma chamber walls and the magma chamber axis (Fig. 4.31 indication I). However, elements surrounding the magma chamber are quite large (Fig. 4.31 indication II). In the case of mesh B, the elements at surface, the

magma chamber walls and the magma chamber axis have been refined (Fig. 4.31 indication III) and as a consequence of the mesh generator, the elements surrounding the magma chamber have been refined, too (Fig. 4.31 indication IV). In comparison to meshes A and B, mesh C is less refined at surface, the magma chamber walls and the magma chamber axis (Fig. 4.31 indication V). By contrast, elements surrounding the magma chamber are smaller and more abundant (Fig. 4.31 indication VI). If we compare, this three meshes with that of model NR-0.2 AS the most similar one is mesh C. Whereas the meshes of the axial symmetric models have less than 50,000 triangular elements, the 3-D meshes used in this work have between 800,000 and 1,000,000 tetrahedral elements. Using a standard personal computer Intel Pentium® 4 CPU 2.66 GHz and 1GB RAM, the generation of such a 3-D mesh and the corresponding calculus may last between 15 and 30 min each. Additionally, up to now the limit of elements calculable with the abovementioned computer due to the RAM memory is around 10^6 elements. Consequently, when calculating the 3-D models with a mesh similar to that of the axial symmetric models we are close to the computational limits of our computer. However, from the results illustrated in Figure 4.30 it is evident that 3-D models are more sensible to mesh changes than the AS ones. Moreover, notice that decreasing the size of the elements is not necessarily the best way to improve the results of our mesh (compare mesh A and C). The number of elements is approximately the same, but mesh A is more heterogeneous than mesh C and the number of elements between the magma chamber and the surface is greater in the latter. Displacement values obtained with mesh C are slightly closer to those of the AS model. Observe, that simply to give the mesh a more uniform element size covering better the zone between the magma chamber and the surface, improves the results in 0.15. We imagine that, similar to the model of the cube exposed in section, results in the displacement distribution obtained with an accurate 3-D mesh would we almost equal to that obtained with the AS models. Nevertheless, the performance of such refined meshes are out of our computational possibilities.

Additionally, Figure 4.31 illustrates that refining the mesh do not introduce changes in the position of the σ_3 peak. Therefore, interpretations of the results concerning this aspect are independent on the applied 3-D mesh.

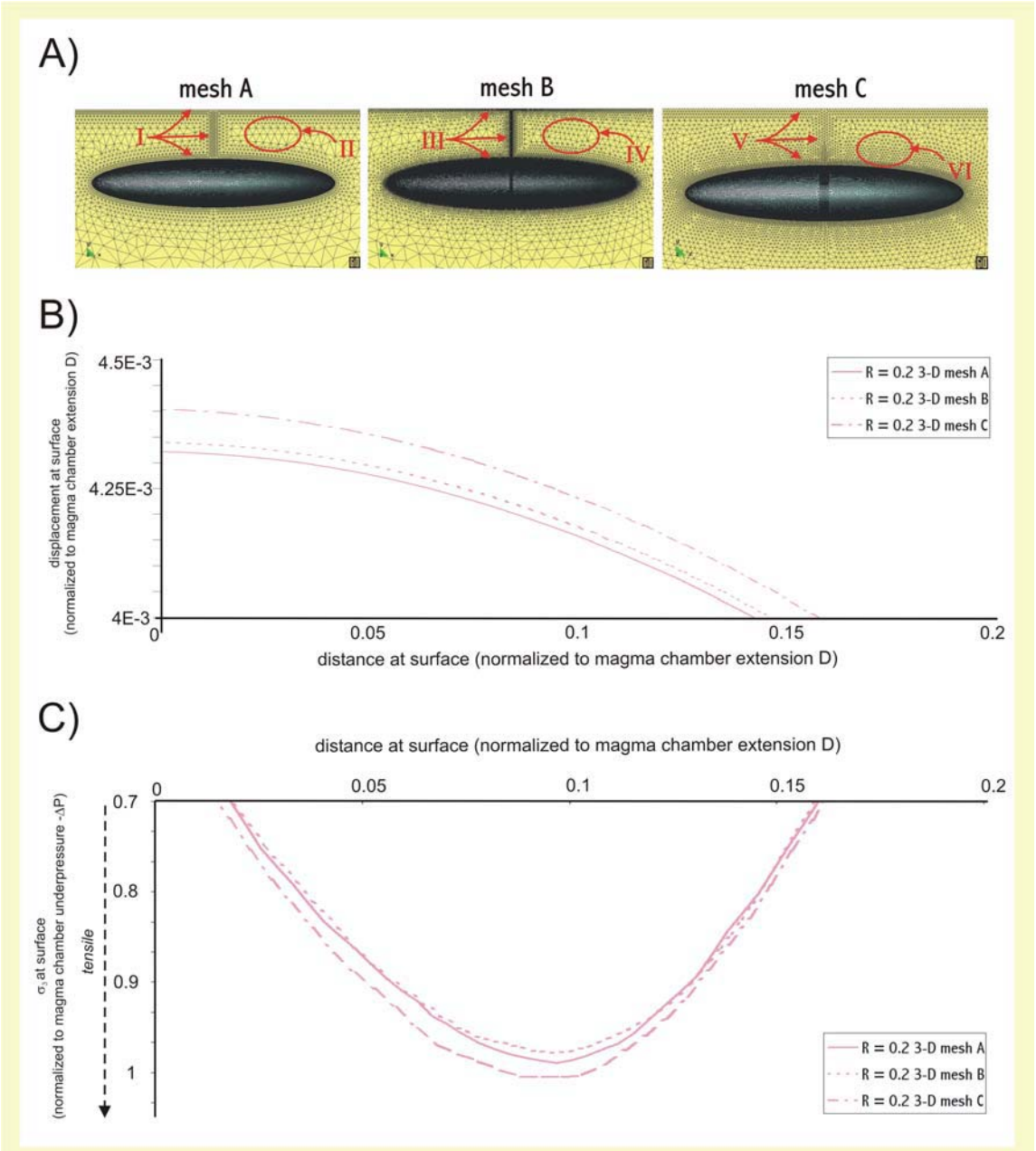

Fig. 4.31: Detailed comparison of the results obtained when using an axial symmetric (AS) or a 3-D geometrical setting. On the top of the Figure different mesh of model NR-0.2 3-D (**R**=0.2, 3-D). The Figure includes the distribution of the displacements and of σ_3 at surface versus distance respect the magma chamber axis. Values of displacements and distances are normalized to the magma chamber diameter and those of σ_3 to the magma chamber underpressure **-ΔP**. **D** Magma chamber diameter; **R** Roof aspect ratio.

IV.5.4.6.2 Volcanological implications of the selected geometrical setting

Now, we want to compare our results with those exposed by Folch and Martí (2004) (Fig. 4.32). Additionally, we want to analyse the volcanological implications of the selected geometrical setting. Remember that these authors use an AS approach for their calculations. Consequently, our results obtained considering AS should by identical to those exposed by Folch and Martí (2004).

We have seen in our results that regarding the contour fills of σ_1-σ_3 and σ_3, there are any significant differences when using a 3-D or a AS geometrical setting. Consequently, our results and those exposed by Folch and Martí (2004) should be approximately equivalent. Effectively, similar to our models, regardless the roof aspect ratio of the mathematical model the maximum value of σ_1-σ_3 occurs at the outer margins of the magma chamber and this is enough high, so that shear fractures can be produced according to condition (2) for ring fault formation. Our results regarding the contour fills of σ_3 values are also similar to those of Folch and Martí (2004). For low roof aspect ratio, σ_3 values at surface become more tensile. Only for low **R** values, σ_3 is enough low so that tensile fractures can be produced according to condition (1) for ring fault formation.

According to our results, the most important differences should appear when comparing the distribution of σ_3 at surface. Remember that our results vary noticeably when considering 3-D or AS geometry. In Figure 4.32 B we can see some of the results exposed by Folch and Martí (2004). Notice that according to them, the condition of ring fault formation concerning the location of the peak of maximum tension (minimum σ_3) at a radial distance approximately equal to the projection at surface of the magma chamber extension is never attained for certain magma chamber configurations (a given **R** and ***e*** pair). In such cases, the location of these fractures at too large radial distances impedes the formation of ring faults because this violates condition (3). Comparing our results with those exposed by Folch and Martí (2004) we can affirm that the main differences reside in the position of the σ_3 peaks. Our results obtained with the 3-D models localize the minimum value of σ_3 at a distance shorter than **D**/2, i.e. a radial distance shorter to the projection at surface of the magma chamber extension. Additionally, contrarily to Folch and Martí (2004) results, this position is independent on the roof aspect ratio value. Consequently, if we calculate the value of the angle $\boldsymbol{\omega}$ (Fig.

4.2) for the models NR-0.2 3-D, NR-0.4 3-D and NR-0.6 3-D (Fig. 4.29), we can observe that it decreases with the roof aspect ratio of the models. Contrarily to Folch and Martí (2004) results, for higher **R** values faults may be closer to the vertical.

According to their results (Fig. 4.32), the authors stated that in all their numerical runs they observed that those chambers that verify conditions (1) and (3) at surface verify also condition (2) at the chamber walls. With Figure 4.32 B the try to illustrated how, for sill-like chamber geometries, there exists a critical value for R (a critical chamber depth) above which both shear and tensional fractures are produced in a way that encourage the formation of subvertical ring-faults. Tensional fractures open at surface along the vertical direction, whereas a conjugate pair of shear fractures appears at a point above the chamber margins and forming angles of ± 45º with the normal to the walls. Despite their model is unable to predict subsequent fracture propagation, the orientation of principal stresses at this point suggests a rather vertical orientation for shear fractures. Finally, the authors perform the classification of the two collapse caldera end-members in terms of the dimensionless parameters **R** and ***e*** (Fig. 4.6). Evidently, with the new 3-D results this classification may be rethought.

After comparing our results with those presented by Folch and Martí (2004) we can appreciate how influential are in mathematical models the selected geometrical settings. In short, it is necessary to ensure when performing mathematical models that the selected boundary conditions, material properties and other pure numerical factors like mesh size or the numerical approach may influence the numerical results. It can happen, as we have seen in this chapter, that results may vary considerably depending on the selected characteristics. We cannot forget that the comparison of numerical results with a direct and clear field observation is a difficult and risky task, since we are not able to collate the obtained information.

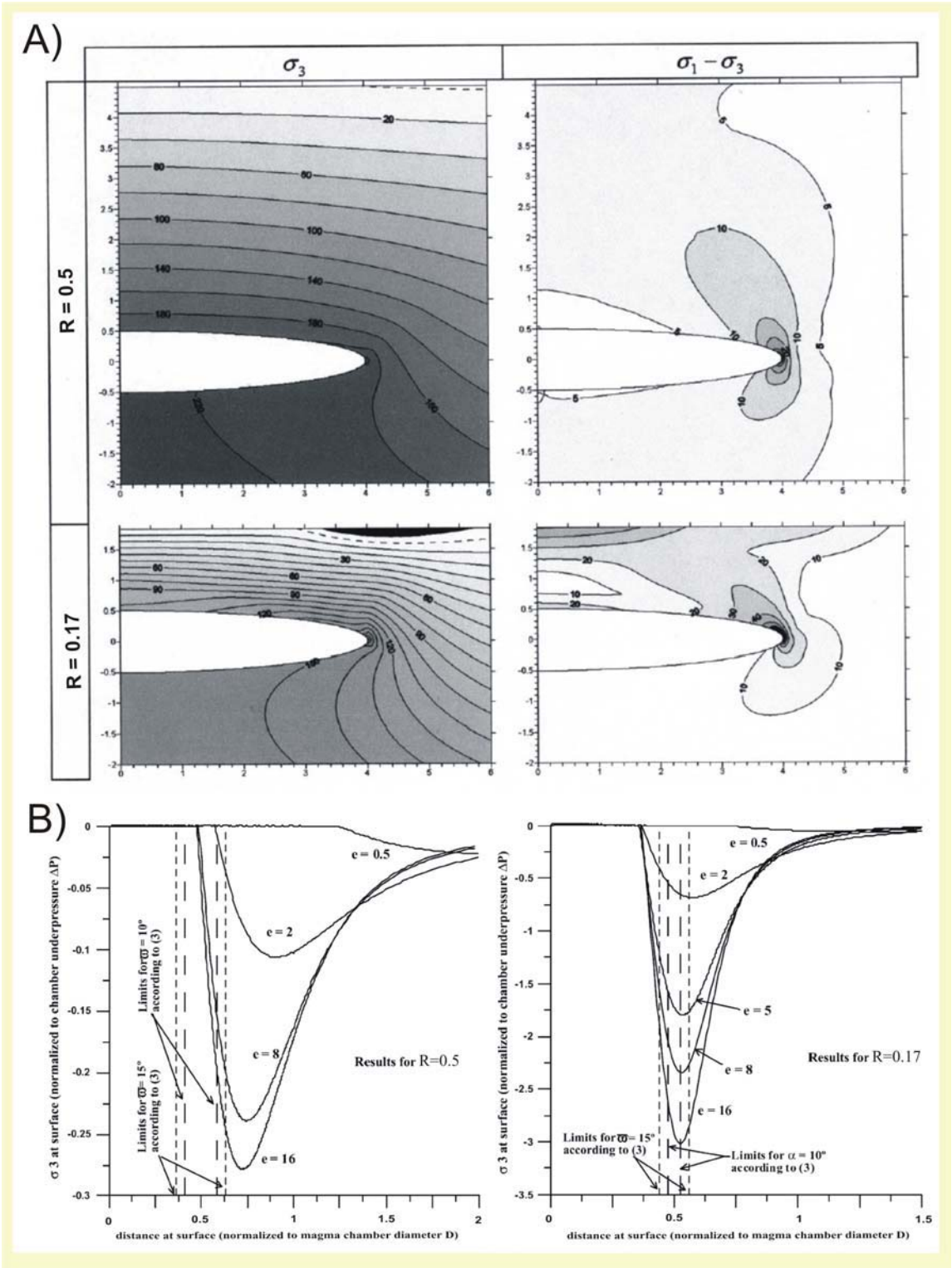

Fig 4.32: (A) Contour fills of σ_1-σ_3 and σ_3 for two magma chambers with ***e***=8 and R=0.5 and 0.17 after a decompression of 10 MPa. In both cases, only the region of the computational domain around the chamber is shown. The regions where σ_3<-T_0 for T_0 =10 MPa, i.e. where tensile fractures can be produced according to condition (1), are indicated in black. Regarding the contour fills of σ_1-σ_3 , the regions where σ_1-σ_3 >S_0 for S_0 =50 MPa, i.e. where shear fractures can be produced according to (2), are indicated in black. In any case, distances are given in km and stresses in MPa. For R=0.17, both shear and tensional fractures are produced in a way that encourage the formation of subvertical normal ring-faults. (B) Values of σ_3 at surface plotted versus radial distance for values of R=0.5 and 0.17. Stress values are normalised to chamber underpressure whereas radial distance is normalised to chamber extension, i.e. the surface projection of the chamber walls peaks at dimensionless distance 1. The origin of coordinates is at the symmetry axis.

IV.5.5 Influence of damage-zone growth on fault displacement

IV.5.5.1 Introduction and objectives

This section has two basic aims. One is to summarize recent field studies on the typical infrastructures of fault zones. The focus is on the fault core and fault damage zones, and how they grow and change with the development of the fault zone itself. In fact, these mechanical properties determine the fault slips and may control also fault reactivation. A second aim is to present new mathematical models on the effects of a growing damage zone on fault slip.

As mentioned above the aim of this section is to explore the effects of increasing damage-zone thickness on fault slip. Therefore, we have performed many mathematical models trying to simulate various fault zones. The results obtain are applicable to any type of faults, here idealized as sinistral strike-slip faults or vertical dip-slip faults such as those acting on caldera collapses.

Often caldera collapse processes take place incrementally during a short period of time during the same eruptive cycle (e.g. Bolsena – *Italy*, Nappi et al., 1991). In some cases, a subsequent collapse caldera close to a previous one, making good use of the existing ring fractures. Furthermore, as mentioned before (see sections I.1.2, II.5.7.5 and III.2.2), there exists relevant regional tectonic structures that may control the subsidence process or may be reactivated during the caldera collapse. Therefore, we consider very interesting to study the influence of the damage-zone growth on fault displacement related to caldera collapse.

IV.5.5.2 Infrastructure of a fault zone

Regarding the infrastructure of a fault zone, field studies worldwide indicate that fault zones consist of two main hydromechanical units: a fault core and a fault damage zone (Fig. 4.32). On the one hand, the core is primarily composed of fault rocks, such us breccia or gouge. On the other, the damage zone contains some lenses of breccia but is characterized by fractures of various types (Berg, 2000; Braathen and Gabrielsen, 1998;

Bruhn et al., 1994; Caine et al., 1995; Simmenes, 2002). During fault activity the core is normally soft (with a low stiffness), however, if the fault is inactive for a long time, it heals and seals becoming stiffer.

Furthermore, fields studies show that fracture frequency in a damage zone is often quite variable, but normally decreases with distance from the core-damage zone boundary (Berg, 2000; Braathen and Gabrielsen, 1998; Bruhn et al., 1994; Caine et al., 1995; Li et al., 1994; Simmenes, 2002). Similar results are obtained for microfaults in laboratory experiments (Shimada, 2000). Generally, an increase in the frequency corresponds to a decrease of the effective stiffness ***E*** (Young's Modulus) in a direction perpendicular to the main fracture direction. Consequently, the stiffness of a damage zone normally decreases on approaching the fault core (Fig. 4.32). On the basis of fracture frequency, a fault damage zone can commonly be divided into several subzones or units, each with a different stiffness (Gudmundsson and Brenner, 2003).

During fault activity the core accommodates most of displacement. Faults and fractures located in the core tend to be smaller than those in the damage zone and its characteristic features are cataclastic rocks such as gouge and breccia (Fig. 4.33). In an active fault, the crushed and altered cataclastic rocks of the core remain soft, with a granular-media structure at the millimeter or centimeter scale. In moderately to highly active fault zones the core material behaves as ductile except during fault slip.

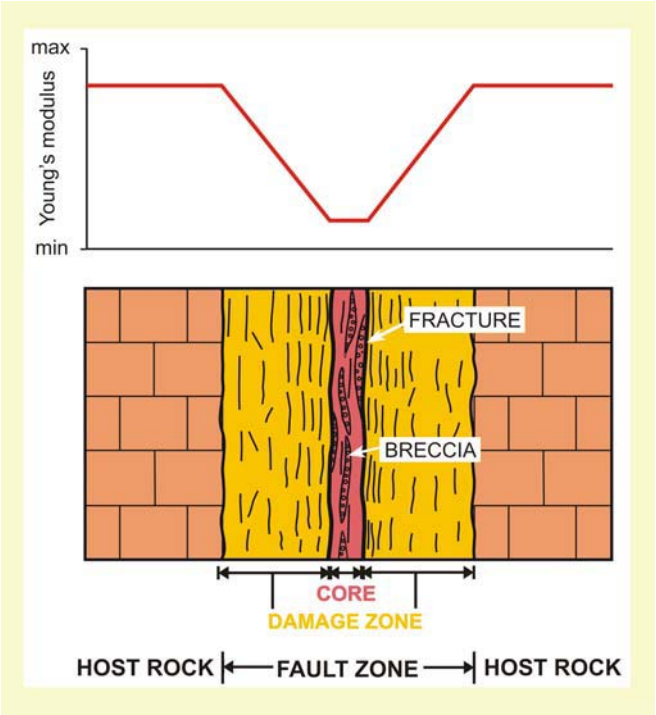

Fig. 4.33: Schematic illustration of a typical fault zone consisting of two main mechanical units: a comparatively thin core and a much thicker damage zone. The effective Young's modulus (stiffness) decreases from the host rock to the boundary between the core and the damage zone.

It is important to remark that the thickness of the core and damage zone increase with fault displacement (Berg, 2000; Braathen and Gabrielsen, 1998; Bruhn et al., 1994; Caine et al., 1995; Simmenes, 2002). For example, fault zones with displacements of tens of kilometres have damage zones that reach a thickness of several kilometres and cores (sometimes more than one) that reach ten meters.

So long as slip on a fault continues, the core and the damage zone maintain lower stiffnesses than the surrounding host rock (Fig. 4.33). As the damage zone increases its thickness, its stiffness may be expected to have gradually stronger effects on fault slips.

IV.5.5.3 Numerical fault models

IV.5.5.3.1 Procedure and geometrical settings

For the models we choose a 2-D plain strain geometrical setting. The computational domain is a rectangle of 2600 × 2400 length units LU. In the interior we simulate an existing fault by introducing a thin and elongate hole (Fig. 4.34 A). The fault-plane is 400 LUs long (strike dimension) and its opening (thickness of the fault core) is of 0.2 LUs. In order to analyse the effects of the damage zone growth we define 10 mechanical units around the opening. In each of the 10 total model runs, a new mechanical unit (of 10 length units) is added on either side of the fault, in order to simulate an increase in the damage-zone thickness (Fig. 4.34 B).

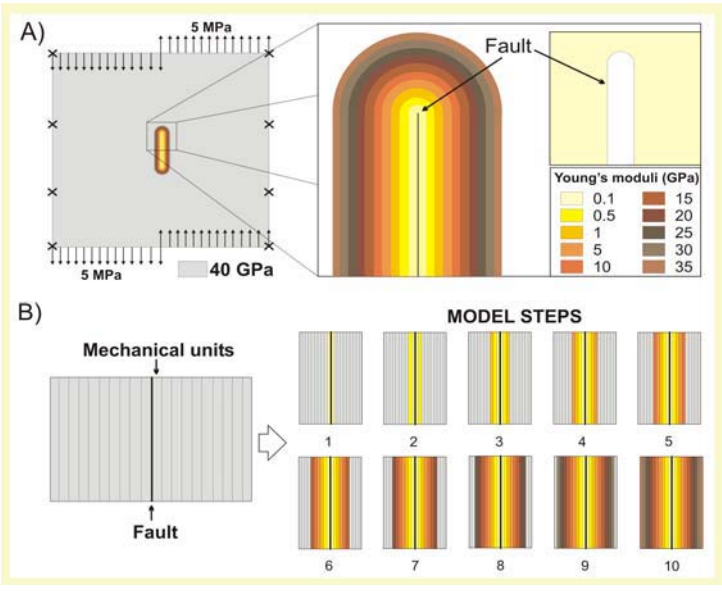

Fig. 4.34: Boundary-element model of fault displacement. **(A)** The boundary conditions and the variation in Young's modulus (stiffness) in the core and damage zone. **(B)** The damage-zone thickness is gradually increased in 10 steps. Step 10 corresponds to the mechanical units and stiffnesses shown in (A).

IV.5.5.3.2 Boundary conditions and numerical method

Results are obtained using the commercial boundary-element program BEASY® (Beasy, 1991; Brebbia and Dominquez, 1992; http://www.beasy. com).

Boundary conditions for the models are illustrated in Figure 4.33. The model boundaries running parallel with the fault, supposed to be far away from the fault, are fastened (fixed) using the conditions of fixed zero displacement (Fig. 4.34 A). Furthermore, a typical stress drop of 5 MPa (Scholz, 1990) is used as driving stress. Since the fault dimensions and the loading are constant, the only parameter that changes between the different models is the thickness of the fault-damage zone. In the present models we use data on typical laboratory values of stiffnesses for igneous rocks such as basalts but scale the laboratory values (Carmichael, 1989; Bell, 2000) down to lower values so as to take the effects of fractures in the damage zones into account. In the final geometry (step 10, Fig. 4.34 A) the stiffnesses of the mechanical units gradually decreases from 35 GPa at the contact with the host rock to 0.5 GPa next to the core. The host-rock stiffness is 40 GPa. The core stiffness is 0.1 GPa, a value based on typical static stiffnesses of unconsolidated rocks as well as in situ measurements from various fault cores worldwide (Hoek, 2000; Schön, 2004).

IV.5.5.4 Numerical results

For the given boundary conditions, the fault has its maximum displacement at the centre and the minimums at the borders (Fig. 4.35 A). The two peaks of tensile stress concentrations occur at the opposite locations of those of high compressional stresses (Fig. 4.35 B). One principal result is that the maximum displacement on the fault also increases (Fig. 4.36). It follows that fault slip generated during a particular event, may gradually increase with increasing damage-zone thickness. Thus, for a fault of constant rupture (trace) length, the ratio of the maximum displacement to the rupture length should decrease with time. Additionally, when the damage-zone thickness gradually increases, the maximum displacement increases although the fault-displacement curves remain geometrically similar (Fig. 4.37). Thus, irrespective of the displacement size, the displacement profile remains similar as regards shape; namely, a smooth curve with a

maximum displacement at the centre and minimum displacements at the lateral tips of the fault.

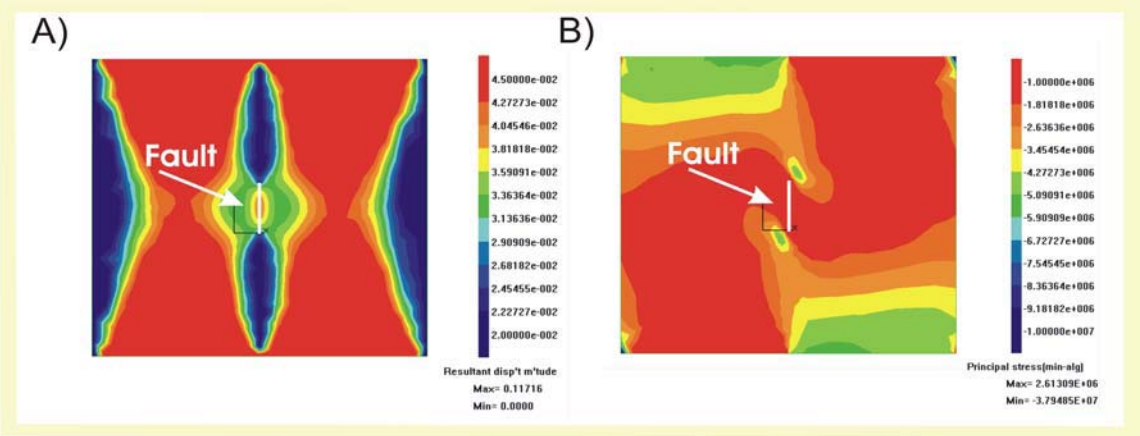

Fig. 4.35: Results obtained for step 10. Contour fills correspond to **(A)** Displacements. **(B)** Values of σ_3 (the maximum principal tensile stress).

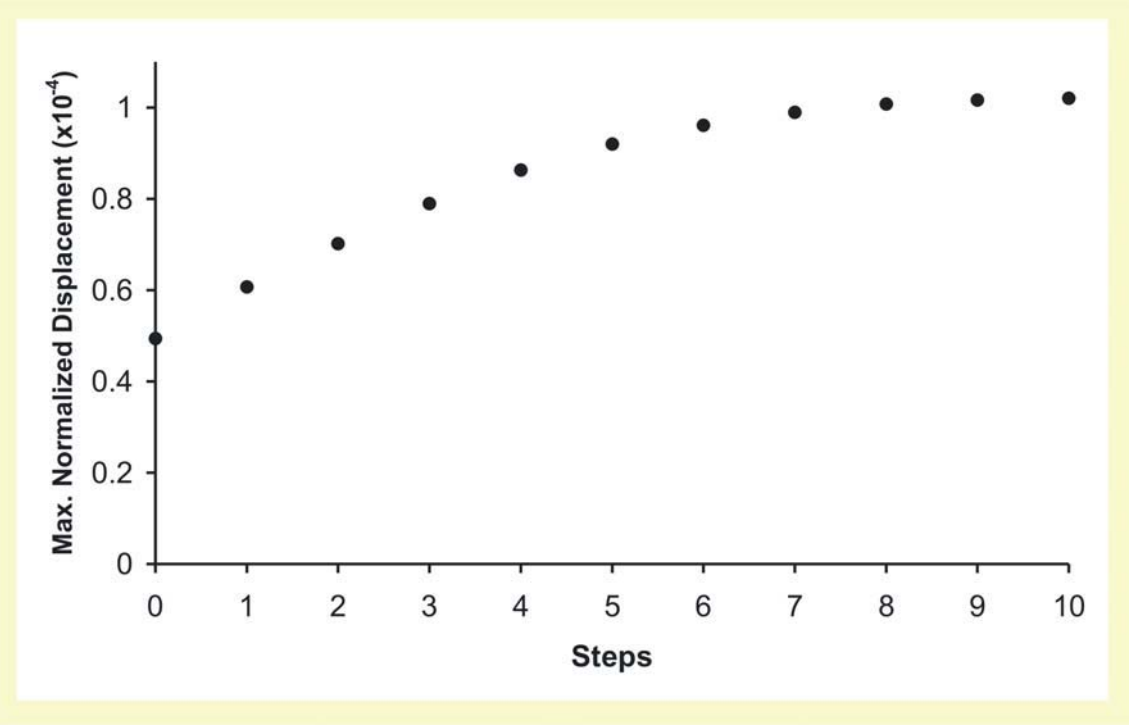

Fig. 4.36: Maximum normalized displacement (MND) in the fault center in each of the 10 steps (Fig. 3). Here MND = $10^4 \times$ *MD/FL*, where *MD* is the maximum displacement and *FL* the fault length, both expressed in model length units.

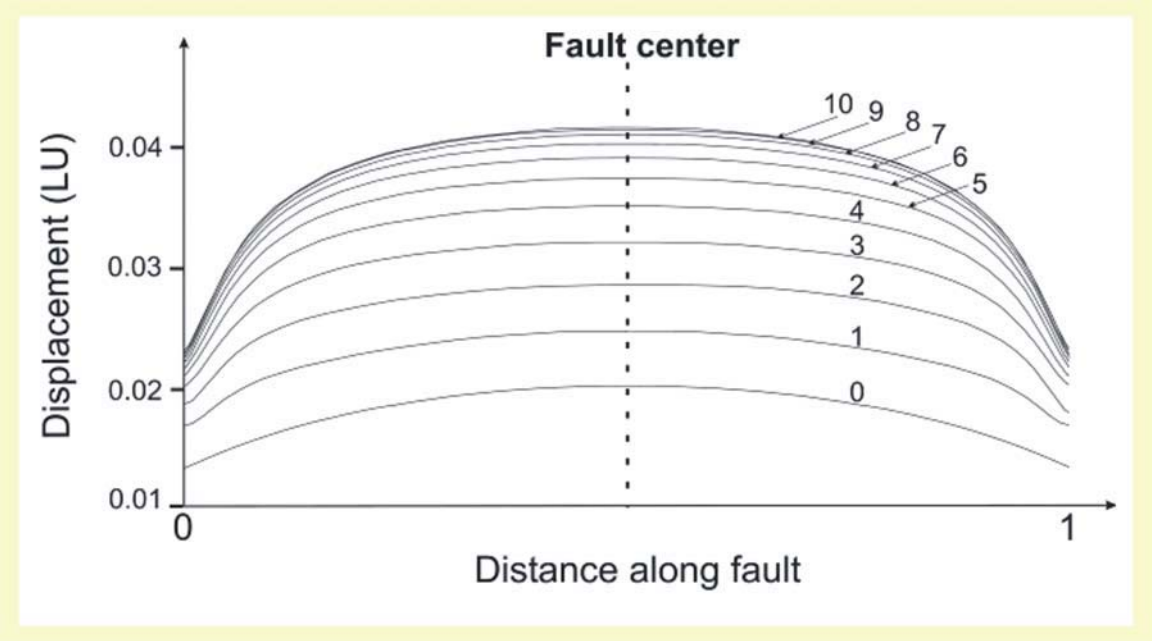

Fig. 4.37: Displacement curves along the length of the fault in each of the 10 steps (Fig. 4.34).

IV.5.5.5 Discussion

Fault displacement is directly proportional to the rock Poisson's ratio ν and the shear stress $\Delta\tau$ driving the displacement (Gudmundsson, 2000). Altough the Poisson's ratio depends on the rock type under consideration, its range is generally small compared with that of Young's modulus; for most crustal rocks Poisson's ratio is between 0.2 and 0.3 (Carmichael, 1989; Bell, 2000). Furthermore, stress drop, or driving stress, which lead to faulting has also a remarkably narrow range. In fact, most stress drops are between 1 and 10 MPa, and commonly 3-6 MPa (Scholz, 1990).

Furthermore, previous studies (Gudmundsson, 2000) indicate that for a given controlling dimension and driving stress the displacement increases, as E gets lower, which is in perfect agreement with the numerical results (Fig. 4.33). These theoretical results are also by supported by direct observations. Various field studies indicate that as a fault evolves, not only does its damage zone and core become thicker (Bruhn et al,. 1994; Berg, 2000; Simmenes, 2002), but its displacement u becomes larger in proportion to its trace length L so that the L/u ratio becomes smaller.

IV.5.5.6 Implications for caldera collapses

It is typical in some caldera systems that collapses episodes may occur repeatedly. Evidently, if we apply the results obtained in this section we can assume that due to the fractures that took place during the first collapse process it is possible that reactivation of pre-existing faults or the collapse onset is easier during the subsequent caldera-forming eruptions. If we extrapolate the observed results to natural caldera collapses, for the same stress field we would expect to find in reactivated faults higher displacements in the subsequent collapse process. We assume that caldera subsidence is controlled by the collapse mechanism but it is also limited by the high of the magmatic reservoir. However, attending to these observations it is plausible to assume that displacements along pre-existing ring faults during a second caldera collapse would be greater than the first one only due to the fact that the damage-zone surrounding the fractures has increased. Additionally, since post-collapse alteration processes may also alter and modify the stiffness of the host rock surrounding the ring faults there is the possibility that these processes may also influence in the displacement and fracture reactivation in posterior caldera collapses. It is clear that the mechanical conditions for subsequent caldera-forming events may vary during each cycle.

IV.5.6 Restrictions of the performed mathematical models

The principal aim of this section is to sum up the main restrictions of the mathematical models presented in this chapter. Some of them were already mentioned in section IV.2.3 and others appear after analysing results obtained in this work.

IV.5.6.1 The use of elastic models

A first group of numerical limitations are related to the use of elasticity as the selected host rock rheological behaviour. We have seen when trying to reproduce numerically the analogue models of chapter 3 that using this rheology is not possible to reproduce fault or brittle failure structures in detail. In fact, it is quite difficult to

correlate the numerical results with the experimental observations. We admit that the use of linear rheologies permits to work with the superposition principle of stress fields and facilitates the required calculation but the list of implicit restrictions is quite long. We suppose that the same mathematical models performed with different rheologies would offer completely opposite results, at least in such detailed study. Consequently, although linear elasticity may be suitable for a first numerical approximation is it recommendable the use of more complicated, i.e. realistic approaches. In fact, to consider linear elasticity when reproducing analogue experiments may be only reliable for simulating the first stages of the collapse process, i.e. the down flexure phase, prior to the appearance of any brittle structure. Once the first fracture has appeared, elasticity is far away from reproducing with accuracy the deformation that takes place during the collapse. These observations concerning the reproduction of analogue models may be extrapolated to those mathematical models trying to simulate "natural" conditions. If we base our interpretations only on numerical examples performed with elastic assumption they cannot be satisfactory enough and lead to misinterpretations of natural systems. Additionally, since we use linear elasticity, we are not able to consider the presence of regional faults or previous formed structures.

IV.5.6.2 Defining the geometrical setting

Some restrictions come directly from the considered geometrical setting. As we have seen, it is necessary to take into account possible variations in the results due to the selected geometrical setting. Several authors (e.g. Gudmundsson, 1998; Gray and Monaghan, 2004) (see Table 4.1) use 2-D geometries considering that the obtained results are an enough accurate solution. However, we have seen in sections IV.5.3.6.2 and 5.4.6.1 that this is not necessarily the case. Depending on the selected geometrical approach results obtained can be conceptually very different. Again, this is a crucial aspect when extrapolating the results obtained to natural systems. Since we try to understand complicated natural systems it is obvious that a too simplistic model may induce us to important conceptual errors and interpretation of our observations. We should try to improve mathematical models using if possible the most accurate geometries and trying to avoid too simple geometrical approaches like 2-D models. We

have seen that results of even axial symmetric and 3-D models may have important differences, although theoretically, results obtained should be equivalent.

IV.5.6.3 Influence of the mesh and computational limitations

An important source of errors in mathematical modelling is the mesh quality, which is strongly dependent on the own computational limitations. It is important to consider that although 3-D modelling is the best numerical approach, the accuracy and reliability of the obtained results is controlled by the quality of the used mesh. In our models we try to use the most refined finite element we are able to calculate using our standard personal computers (PC). Of course, more powerful machines or supercomputers would allow us to perform very fine meshes and consequently, much better calculations. As we assume that not all research groups are able to calculate with the helps of such potent computers we have preferred to infer the error provided by the calculus capacity of normal PCs.

IV.3.6.4 Additional limitations

Logically, our mathematical models are also affected by the restrictions commented in section IV.4.3. In our models reproducing natural systems (see section IV.5.4) we consider a homogeneous host rock, which is of course a simplification. Additionally, our models do not allow the possibility of dike injection and of course, fluid dynamics and rock mechanics are uncoupled. Moreover, models of section IV.5.4 are carried out without the presence of a volcanic edifice that may alter the stress around the chamber and slightly vary the observed results.

IV.6 SUMMARY AND CONCLUSIONS

This chapter has been addressed to summarize the most important aspects concerning theoretical/mathematical models of collapse calderas, which are important to quantify variables, to predict semi-quantitative general conditions for fracture or fault

formation and to provide a link with magma properties. Mathematical models allow to determine when caldera collapse process will occur, but they cannot tell us how such a complex process will develop. Mathematical models on collapse calderas performed during the last years can be classified depending on the topic they are focused on. There exit principally three groups: Models focused on the pressure evolution inside the magma chamber, models that determine stress conditions for normal-fault caldera initiation and models for predicting fault location using non-elastic rheology.

In this chapter, we have also introduced the important aspects regarding pressure evolution inside the chamber during volcanic cycles (specially caldera-forming eruptions). From this theoretical analysis, we have defined two collapse caldera end-members: under- and overpressure calderas. Additionally, we have sum up the conditions for ring fault initiation, i.e. the mechanical conditions to the caldera collapse onset: (1) The minimum value of σ_3, the tensile stress, (maximum tension) must be at surface, (2) the maximum value of σ_1-σ_3, the shear stress, must occur at the outer margins of the magma chamber and (3) the maximum tension at surface must peak at a radial distance approximately equal to the projection at surface of the magma chamber extension.

Furthermore, in this section we have described the different restrictions and limitations found in the mathematical models applied to the study of collapse calderas. These vary from model to model, and are principally dependent on the design of the physical model and the considered rheological behaviour for the host rock.

The new mathematical models exposed in this work want to reproduce some of the analogue experiments presented here offering us the possibility of comparing the results obtained using mathematical or analogue models to detect additional restrictions of both methodologies. We have also reproduced some of the existing mathematical models to study the influence of the selected geometrical setting (e.g. axial symmetric or three-dimensional) in the obtained results and the subsequent interpretation of the required stress field likely to initiate normal ring faults without the influence of any pre-collapse fracturing or differential tectonic stress. Moreover, we have presented another type of mathematical models, not strictly related to collapse caldera processes but from which the results obtained are applicable to the study of collapse mechanisms and controlling factors.

The main restrictions of our mathematical models are related to the use of elasticity as the selected host rock rheological behaviour, to the considered system

geometril and to the quality of the used mesh. Additionally, we have seen that the restrictions of the mathematical models may lead to misinterpretations of the results obtained.